1982

A [mu]+SRstudy of uniaxial stress induced symmetry breaking in an Fe single crystal

Min. Namkung
College of William & Mary - Arts & Sciences

Namkung, Min

A POSITIVE MUON SR STUDY OF UNIAXIAL STRESS INDUCED SYMMETRY BREAKING IN AN IRON SINGLE CRYSTAL

The College of William and Mary in Virginia PH.D. 1982

A μ^+SR STUDY OF UNIAXIAL STRESS INDUCED SYMMETRY BREAKING IN AN FE SINGLE CRYSTAL

A Dissertation

Presented to

The Faculty of the Department of Physics

The College of William and Mary in Virginia

In Partial Fulfillment

Of the Requirements for the Degree of

Doctor of Philosophy

---

by

Min Namkung

1982

APPROVAL SHEET

This dissertation is submitted in partial fulfillment of

the requirements for the degree of

Doctor of Philosophy

Min Namkung

Min Namkung

Approved, October 1982

William J. Kossler

Kenneth G. Petzinger

Harlan E. Schone

Mark S. Conradi

Gary C. DeFotis

Carey E. Stronach

Robert Grynszpan

TABLE OF CONTENTS

ACKNOWLEDGMENTS

Writing this dissertation, I am indebted to many people for their advice, help and support. My advisor William J. Kossler, who initiated this project, designed most of the equipment and managed the experimental schedule which involved an international collaboration. While allowing my fully independent role in the research, his continuous guidance and encouragement made this dissertation work possible.

I wish further to express my gratitude to the following persons:

C. E. Stronach and R. I. Grynszpan for their participation in the experiment, fruitful discussions and thorough reading of the dissertation;

K. G. Petzinger for his help with solid state theories, valuable discussions and derivation of the fitting equation used in this work;

W. D. Kündig, P. F. Meier and B. D. Patterson for their hospitality and collaboration during the experiment at SIN;

H. E. Schone, M. S. Conradi and G. C. DeFotis for their serving on the dissertation committee, careful reading of the dissertation and help in many other ways;

J. P. Bensel and his staff for their work on the pulling machine;

Sylvia Stout for typing this dissertation and editorial assistance;

My friends in the Physics Department, especially Vanamali Raghunathan and Wei Su Huai for their friendship and help.

Finally, I wish to thank my family for their understanding, encouragement and support during the whole period of time.

LIST OF TABLES

LIST OF FIGURES

ABSTRACT

For the first time, external uniaxial stress has been used in a μ^+SR experiment. The stress dependences of the following parameters were obtained for Fe crystals: the muon precessional frequency, ν_μ, the transverse (longitudinal) depolarization rates, $1/T_2$ ($1/T_1$), and F_T/F_L, the ratio of the probabilities for the muon to find domains with transverse/longitudinal fields. The shift in ν_μ was -0.34 ± 0.023 MHz per 100 micro-strain along the <100>-axis. Changes in other parameters depend on the sample history but they, in general, increase with stress.

External stress changes the muon occupational probability at each site which significantly affects the dipolar field averaged over interstitial sites of the same initial symmetry. This change in the averaged dipolar field is shown to be the main cause of the shift in ν_μ. To calculate the dipolar field at each site, the finite extension of the muon probability density and displacement of neighboring host atoms around the site are explicitly taken into account. From the experimental results and the dipolar field calculation, it is possible to estimate the anisotropy of the double-force tensor, (P_1-P_2), for the muon in Fe. This clearly shows that in Fe, for reasonable muon wave function shapes, the muon is more likely to occupy the 4T(0) site configuration.

For a random distribution of domains among the six easy axes of Fe, the dipolar field averaged over a region of the sample should be zero. However, the external stress breaks this randomness and with a certain magnitude of tensile stress in the z-axis, domains will align along the $\pm$ z-directions. A muon with its initial spin aligned perpendicular to the z-axis does not distinguish the stress induced domain alignment from the saturation along the + or - z direction. The experimental result shows the same stress dependence of ν_μ for both the stress induced and the externally saturated domain alignments. As expected the change in ν_μ with low stress is very small without the application of an external saturation field. Also, the change in F_T/F_L is consistent with that in ν_μ indicating that this parameter is a good measure of the domain alignment.

Similar results were obtained for polycrystalline samples. The interpretation made on the single crystal result is applicable to these results and it is possible to explain why local strains in Fe tend to reduce the magnitude of ν_μ.

A μ^+SR STUDY OF UNIAXIAL STRESS INDUCED SYMMETRY BREAKING IN AN FE SINGLE CRYSTAL

I. INTRODUCTION

Polarized muons implanted in a ferromagnetic specimen will precess with their Larmor frequencies in the local magnetic field. Through its parity-violating decay with a mean lifetime of 2.2 μsec, a muon emits two neutrinos and a positron. The direction of positron emission is preferentially the direction of the muon spin at the time of decay. Such an anisotropic emission of positrons and the precessional motion of muon spins give rise to an oscillatory component in the time dependence of the counting rate of positrons in a given direction.

The local field, B_μ , averaged over a certain region of the specimen, can be obtained from the oscillation frequency of the signal in the positron counting rate. One contribution to B_μ comes from the Fermi type contact field which is called the "muonic hyperfine field". The hyperfine field, B_{hf}, that a muon experiences in the interstitial sites of a ferromagnetic crystal is the consequence of the interaction between the muon and the surrounding local electronic environment.

If an ensemble of muons sees a range of averaged local fields, the signal will be damped in amplitude with a characteristic time T_2. In the presence of the longitudinal component of the local field the spins of the muons will be flipped to reach an equilibrium distribution between the two spin states. This relaxes the muon spin polarization towards equilibrium with a characteristic time T_1.

Once stopped in a crystalline solid, muons start diffusing through the interstitial sites. The role of diffusional motion has been shown to affect drastically the measured local fields. Especially in Fe the fast diffusional motion of the muon averages out the different dipolar fields at the interstitial sites which are crystallographically equivalent but may yet be magnetically inequivalent.

Preparation and purity of a sample influence both the local field and the diffusional motion. For example, in Fe, B_μ and T_2 are greater in well annealed samples of high purity.[1,2] It has been suggested[2] that the strains associated with dislocations and impurities might be responsible for the decrease in B_μ .

Dislocations and impurities produce rather complex strain distributions.[3] Thus to investigate the effect of strain on the internal field distributions the use of uniformly applied stress would be desirable.

Butz et al.[4] have measured B_μ in Fe and Ni under hydrostatic pressure. They found that B_μ decreased (increased) linearly up to the maximum applied pressure of 7k bar in Fe(Ni). For hydrostatic pressure, the crystal symmetry remains unchanged so that the interpretation of the results is relatively simple.

On the other hand, a uniaxial stress applied to a crystalline solid causes a lowering of the crystal symmetry while keeping the volume of the sample almost unchanged. In this work we applied external uniaxial stress to Fe specimens. This thesis is a report on the first results of a series of uniaxial stress μ^+SR experiments which was started for the following reasons:

1) The strain induced by lattice imperfections can be more closely simulated by the strain induced due to uniaxial stress. This is true, especially, when the type of imperfection is a dislocation.

2) In Fe the dipolar fields on the muon will not average out to zero because of the lowered symmetry. Since the dipolar fields are very different at the different interstitial sites in Fe, this may help us to determine the site that the muon occupies.

3) The change in B_μ can be measured by applying the external uniaxial stress along different directions. This will give us more information, compared to the hydrostatic pressure experiment, on the behavior of muons in solids.

4) Since uniaxial stress changes magnetic domains and dislocation structures, the study of the interaction between muons and lattice imperfections can be enhanced.

A detailed discussion on the current status and problems in μ^+SR research on ferromagnetic materials will be given in this chapter following a brief introduction to the μ^+SR method.

A. Decay of Muon and μ^+SR Method

Muons are decay products of pions, which, previously, are produced by the following reactions

$$p + p \longrightarrow \pi^+ + p + n$$

$$p + n \longrightarrow \pi^- + p + p$$

Typical nuclei used for pion production in accelerators are copper and beryllium, and the minimum kinetic energy required for pion production in such a nucleus is about 145 MeV, the threshold energy. Positive pions

decay with a mean lifetime of 26 nsec in the parity-violating process:

$$\pi^+ \longrightarrow \mu^+ + \nu_\mu$$

The decay of a positive muon can be written as

$$\mu^+ \longrightarrow e^+ + \nu_e + \bar{\nu}_\mu$$

with an average lifetime of:

$$\tau_\mu = 2.1994(6)\ \mu\text{sec}$$

The decay is governed by the weak interaction which leads to a violation of parity.

From the four fermion current-current interaction one can write the positron decay spectrum in the following way:[5,6]

$$\frac{dN(W,\theta)}{dW\,dt} = \frac{W^2}{2\pi}(3-2W)\left[1 - P\,\frac{1-2W}{3-2W}\cos\theta\right] \qquad (1.1)$$

where P is the degree of muon polarization, and θ is the angle between the positron momentum and the direction of muon spin at the time of decay. W is the positron energy in units of its maximum possible energy ($W = E/E_{max}$). The maximum kinetic energy is

$$E_{max} = \frac{m_\mu c^2}{2} - m_e c^2\left(1 - \frac{m_e}{m_\mu}\right) = 52.32\ \text{MeV}$$

Assuming that all positrons are detected with the same efficiency, one gets

$$\frac{dN(\theta)}{dt} = \frac{1}{4\pi}\left(1 + \frac{1}{3}P\cos\theta\right)$$

However, the efficiency of positron detection depends on the energy of the positron. Then, one can write

$$\frac{dN(\theta)}{d\Omega} = \frac{1}{4\pi}\tilde{\epsilon}\left(1 + \tilde{A}\cos\theta\right) \qquad (1.2)$$

where A is the average asymmetry. From the form of equation (1.1), one immediately sees that reducing the efficiency of detecting the low energy positrons makes A greater than 1/3. This means, by placing absorbers between the muon target and the positron detectors, the measured asymmetry will be increased but it will decrease the counting rate. The functional form of the term in the bracket of equation (1.2) is shown in Figure 1.

In a typical experiment the polarized positive muons are stopped in the material to be studied. Unless the local magnetic field is exactly parallel to the initial muon spin direction, the spin will precess with the Larmor frequency

$$\frac{\omega}{2\pi} = \frac{g_\mu B e}{4\pi m_\mu} = \frac{\gamma_\mu B}{2\pi} = 13.55\ (kHz/_G) \cdot B$$

From equation (1.2) the probability of emitting positrons along a fixed direction of detector is proportional to $(1 + \tilde{A} \cos\theta)$. Considering the precessional motion of the muon, the angle θ will be replaced by $\theta_0 + \omega_\mu t$, where θ_0 is the angle between the incoming beam and the detector (see Figure 2). Regarding these facts, one may write for the experimental time dependence of the counting rate:

$$N(\theta_0,t) = N_0 e^{-t/\tau_\mu}\left\{1 + A_{eff} \cdot P(t) \cos(\omega_\mu t + \theta_0 + \phi)\right\} + BKG \qquad (1.3)$$

where N_0 is the overall normalization constant, BKG is the accidental constant background, ϕ is the initial phase angle caused by very small rotation of the spin during the stopping process and the location and the finite size of the detector, and P(t) is the relaxation function of the muon spin polarization. A discussion of the physical nature of P(t) will

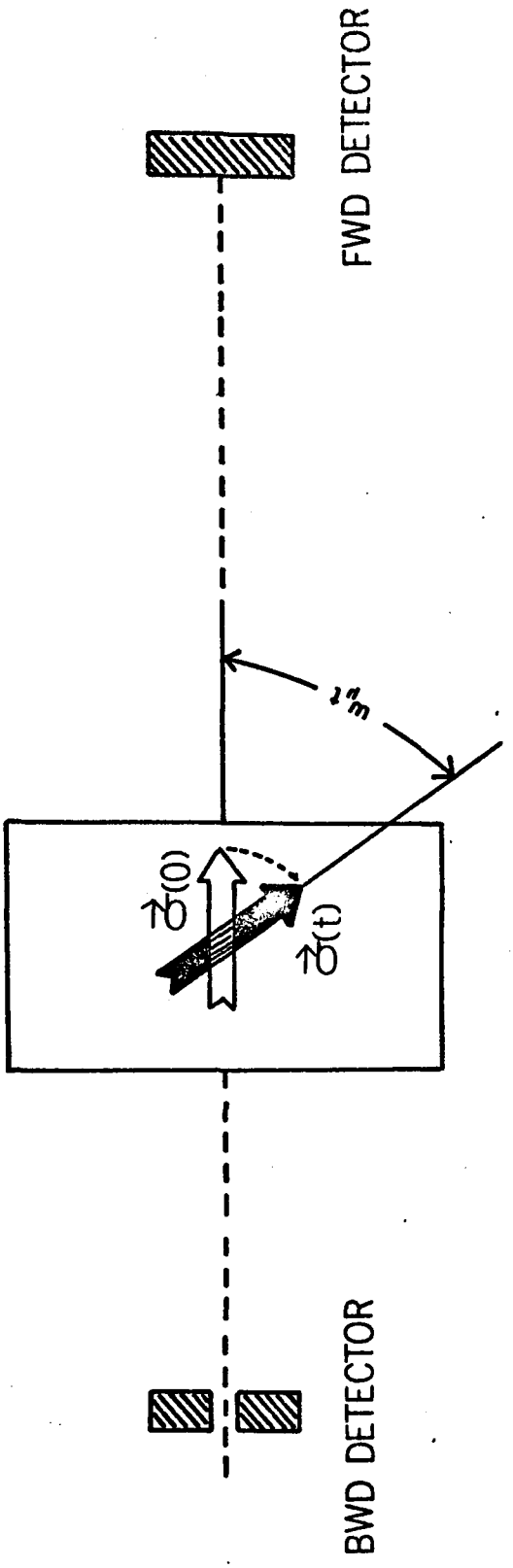

Fig. 1

Precessional motion of muon spin in a solid

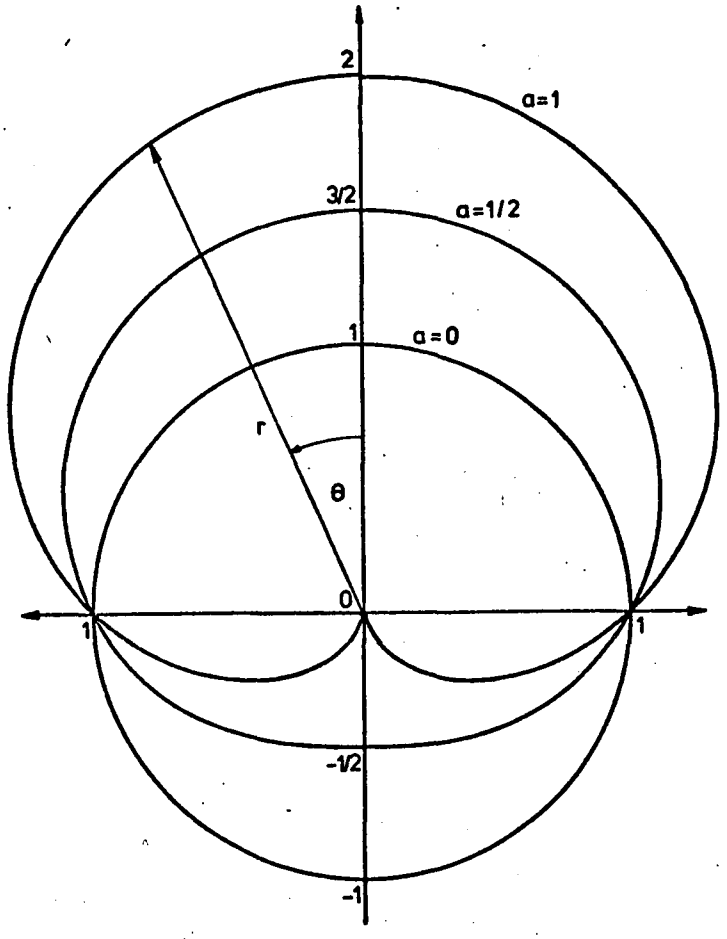

$$r = (1 + a \cos\theta)$$

Fig. 2

Plot of the (1+ a cosθ) distribution for various a values.

be given in A. The generalized form of equation (1.3), including the longitudinal relaxation process, is found in Appendix B.

In the experiments two positron detectors at $\theta_0 = 0$ and $\theta_0 = \pi$ give two histograms $N(0,t)$ and $N(\pi,t)$, respectively. These two histograms are shown in Figure 3.

B. The Muon as a Microscopic Probe of Magnetism

A muon entering a target with a kinetic energy of 50 MeV will lose its energy by scattering from electrons, until its velocity approaches that of the valence electrons of the atoms[7](corresponding to an energy $2 \sim 3$ keV). The total time it takes the positive muon to slow down to $2 \sim 3$ keV in condensed matter is estimated to be about $10^{-10} \sim 10^{-9}$ sec. Depolarization during this stage could only be due to the spin-dependent forces in the scattering process with electrons on nuclei. In both cases as Fond et al.[8] and Wenzel[9] have shown, such depolarization effects are extremely small and negligible.

After stopping in a solid the fate of the polarized muon depends critically on whether or not muonium, a hydrogen-like atom consisting of μ^+ and e^-, is formed. In the muonium the muon will precess in the hyperfine field produced by its single electron. The observed muon frequency directly measures the hyperfine field. In solids this gives information about the electronic environment. However, muonium formation seems to be restricted to a few insulators and semiconductors.

In metals muonium has not been found. This is attributed to the screening of the muon charge by the conduction electrons. The bare muon will probe the local magnetic field B_μ at interstitial sites. In a

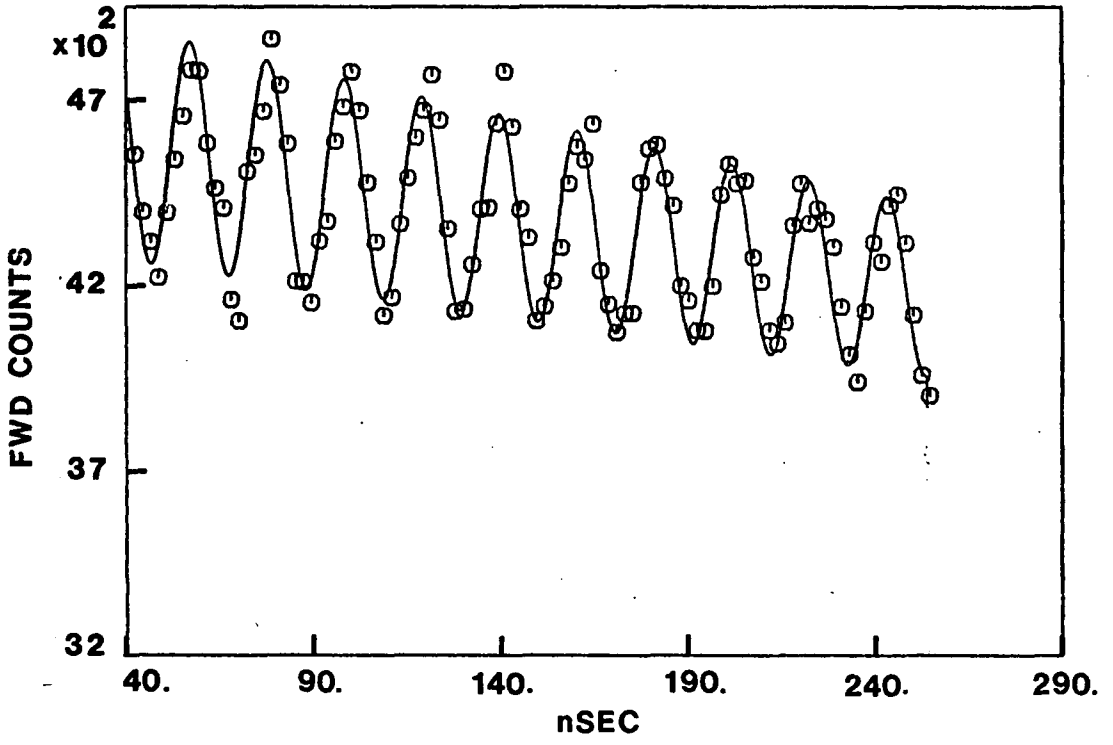

(a)

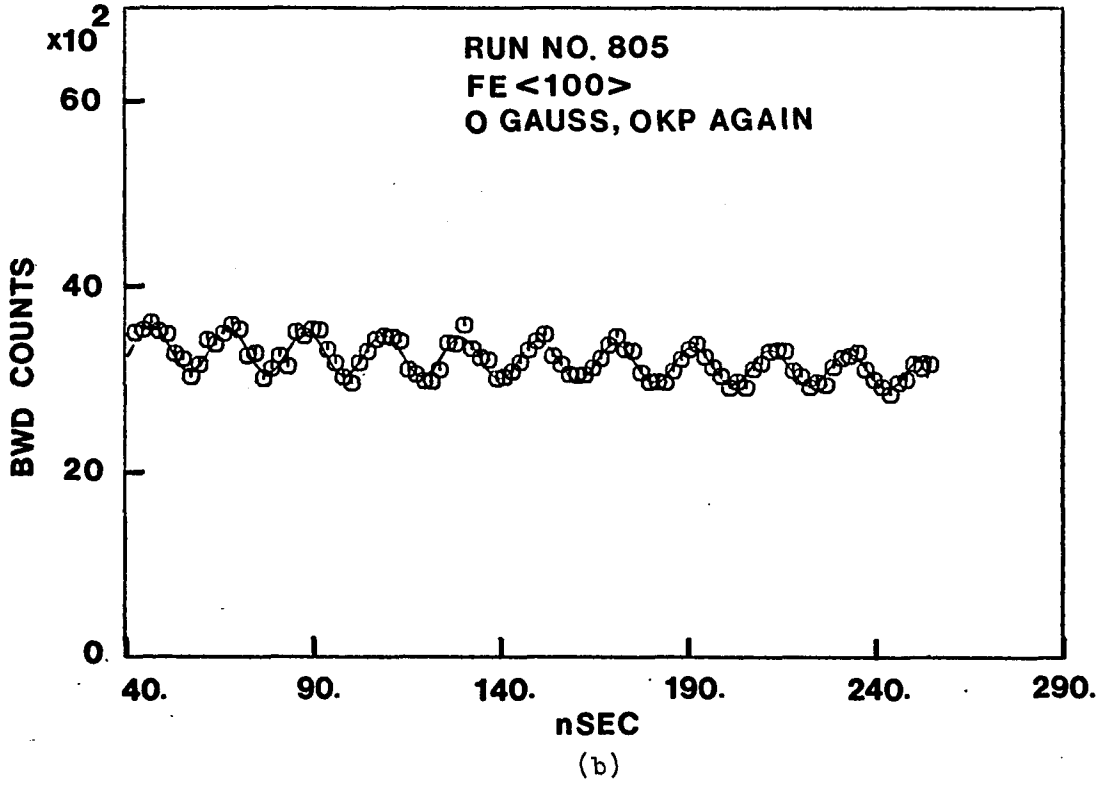

(b)

Fig. 3. Typical μ^+SR histograms
(a) forward histogram
(b) backward histogram

ferromagnetic material the local field B_μ is written as

$$\vec{B}_\mu = \vec{B}_{ext} + \vec{B}_L + \vec{B}_{dem} + \vec{B}_d + \vec{B}_{hf} \tag{1.4}$$

where $\vec{B}_{ext}$ is the externally applied magnetic field, $\vec{B}_L = \frac{4\pi}{3}\vec{M}_s$ is the Lorentz cavity field in a domain ($\vec{M}_s$ = saturation magnetization), $\vec{B}_{dem} = N\vec{M}_s$ is the shape dependent demagnetizing field, $\vec{B}_d$ is the dipolar field due to the magnetic moments of host atoms inside the Lorentz cavity, and $\vec{B}_{hf}$ is the hyperfine field. All terms, except $\vec{B}_{hf}$, in the right hand side of equation (1.4) can readily be calculated. Thus measuring $\vec{B}_\mu$ enables us to obtain $\vec{B}_{hf}$.

The hyperfine field, $\vec{B}_{hf}(\vec{R}_\mu)$, results from the interaction between the polarized conduction electron cloud around the muon and the muon itself. One writes

$$B_{hf,i}(\vec{R}_\mu) = \int d\vec{r}\; D_{ij}(\vec{r} - \vec{R}_\mu)\, M_j(\vec{r}) \tag{1.5}$$

Here, $\vec{M}(\vec{r})$ is the local conduction electron magnetization and

$$D_{ij}(\vec{r}) = (\nabla_i \nabla_j - \tfrac{1}{3}\delta_{ij}\nabla^2)\frac{1}{|\vec{r}|} - \frac{2}{3}\delta_{ij}\nabla^2\frac{1}{|\vec{r}|} \tag{1.6}$$

The first term in equation (1.6) transform as a spherical harmonic of order 2. Therefore, for a spherically symmetric screening cloud, only the second term contributes to the hyperfine field (see Appendix C). From equation (1.6) one obtains

$$\vec{B}_{hf}(\vec{R}_\mu) = \frac{8\pi}{3}\vec{M}(\vec{R}_\mu) \tag{1.7}$$

Therefore, the measured hyperfine field is of great interest in solid state physics because it provides information on the local electronic structure at the interstitial sites. The other parameters like T_1 and T_2 which are measured at the same time give information on muon diffusion and the defect structures in the crystal.

C. Hyperfine Fields in Pure Ferromagnetic Materials

The advantages of using the muon to probe the local microscopic fields are (i) it probes the interstitial sites, (ii) by having only one muon at a time, an infinite dilution of the impurity in the host is possible, and (iii) having no core structure of its own, it is the simplest system of a magnetic dilute alloy.

However, the positive charge of the muon perturbs the local electronic environment and the measured hyperfine fields are referred to this perturbed system. In this sense, equation (1.7) should be rewritten as

$$\vec{B}_{hf}(\vec{R}_\mu) = \frac{8\pi}{3} \rho(0) (n_{o+} - n_{o-}) \mu_B \tag{1.8}$$

where

$$\rho(0) = \frac{n_+(0) - n_-(0)}{n_{o+} - n_{o-}}$$

is the ratio between the local magnetizations after and before the perturbation due to the muon is introduced, and $\mu_B = 9.27 \times 10^{-24} \frac{J}{W/m^2}$, the Bohr magneton.

Table 1 shows the results of measurements of B_{hf} in several elemental ferromagnets. Also shown in the table are the types of interstitial sites for muon stops in these materials. The discussion on the

Table 1. Compilation of some properties of the ferromagnetic metals investigated and summary of the μ^+SR-results. All data are extrapolated to T = 0 K.

	Structure	Sat. magnet. M_s [kG]	Local field at muon B [kG]	Hyperfine field B_{hf} [kG]	Muon site
Fe	bcc	1.750	$-$ 3.67 $\pm$ 0.10	$-$ 11.1 $\pm$ 0.2	?
Co	hcp	1.415	$-$ 0.317 $\pm$ 0.010	$-$ 6.1 $\pm$ 0.2	octahedral
Ni	fcc	0.528	+ 1.48 $\pm$ 0.10	$-$ 0.71 $\pm$ 0.01	?
Gd	hcp	2.010	+ 1.10 $\pm$ 0.05	$-$ 6.98 $\pm$ 0.10	octahedral
Dy	hcp	2.995	$\pm$ 12.30 $\pm$ 0.20	$-$ 25.2 or $-$ 0.7 $\pm$ 1.0	?

site problem will be given in the next section and only the problems directly related to the hyperfine field will be considered in this section.

The value of B_{hf} in Ni at T = 0 K, extrapolated from low temperature measurements, is -0.71 kG. The minus sign of B_{hf} means that its direction is opposite to that of M_s. The unperturbed spin density at the octahedral site of Ni, as measured by Mook,[10] is

$$\mu_B (n_{o+} - n_{o-}) = -0.008S \pm 0.004 \quad \mu_B/A^{o3}$$

which corresponds to a field of -0.66 ± 0.32 kG. This means that the spin density enhancement factor $\rho(0)$ is close to unity.

Petzinger et al.,[11] who performed a spin density functional formalism calcuation on Ni, predicted $\rho(0)$ to be 12.5. To explain such a large discrepancy between the results of experiment and their calculation, they postulated a model in which the relatively unpolarized s band in Ni does the screening of the muon change and the localized 3d wave functions are essentially undisturbed by the screened potential of the muon.

Jena et al.[12] performed similar calculations on transition metals and Gd. They found $\rho(0)$ to be 12.4 in Ni and 9.74 in Fe. In the case of Fe, there is no unique value of the local magnetization measured by neutron scattering experiments (see Reference 13). If one takes the value of the magnetization[13] to be -0.014 ± 0.004 μ_2/A^{o3}, which is averaged over a 0.5 A^{o3} cube centered at the tetrahedral site of Fe, B_{hf} will be -11 kG. This value is very close to the experimental result. This indicates that the basic mechanisms related to B_{hf} in Fe and Ni may be quite different.

J. Kanamori et al.[14] have performed an ab initio calculation in Ni and obtained the values of B_{hf} -0.72 kG and -1.8 kG at octahedral sites and tetrahedral sites, respectively. These preliminary results in Fe were shown to be -13.0 kG for tetrahedral sites and -15.5 kG for octahedral sites. There have been other theoretical approaches to the hyperfine field in Ni. Keller and Patterson[15] obtained -0.59 kG from a cluster calculation. Using KKR methods, Katayama et al.[16] obtained -0.72 kG and with super cell band structure methods, Jepsen et al.[17] predicted -0.463 kG.

All these theoretical calculations assumed rigid positions of the host ions and the muon. However, muons are believed to undergo vibrational motions and also to create local distortion around them while residing in a crystal. Then one may wonder how the theoretical calculations give results close to the experimental result without counting these physical effects. Does this mean that these effects are negligible or do they somehow cancel each other?

P. F. Meier et al.[18,19] have pointed out that, due to computational complexity, the above methods are inconvenient to study the influence of these physical effects on the spin density. They have performed a series of theoretical calculations with a model based on a RKKY-type interaction between the localized moments of the ferromagnetic host and the conduction electrons. Their computational results were parameterized by a dimensionless quantity η defined by

$$\eta^2 = \frac{2}{3} \frac{\langle u_m^2 \rangle + \langle u_\mu^2 \rangle}{a^2}$$

where $\langle U_m^2 \rangle$ and $\langle U_\mu^2 \rangle$ are the mean square displacements from the

equilibrium position of the ion and muon, respectively. Their results show that the influence of the zero point motion on the spin density at the octahedral site of Ni is much smaller than for Gd, Dy or Fe. For this reason Ni seems to be a good candidate for rigid microscopic theories. This means that for other ferromagnetic specimens, especially in Fe which is the sample used in this work, the motion of the muon around an interstitial site and the lattice distortion due to the muon should be included in a full analysis of experimental results.

D. The Muon Sites in Ferromagnetic Materials

Since the hyperfine field must be different at different types of sites, it is important to know at which site the field is being measured. The importance of the site problem can be viewed in a different direction. The diffusion of hydrogen in α-Fe is of great interest because of its technical importance. In spite of this, there is a lack of reliable experimental information on the diffusion mechanism and location of solute hydrogen in α-Fe. Although the sites of muons and hydrogen may not be the same in a solid, knowing the site of the muon certainly helps to determine the site of hydrogen.

Both A. Seeger[20] and Nishida et al.[21] once pointed out that the muon stopping site in α-Fe should be the tetrahedral site. For this they gave the following reasons: The neutron data show that the magnetic moment density is negative at the tetrahedral site and is positive at the octahedral site, the muon hyperfine field in α-Fe is negative, and the tetrahedral site in a BCC crystal is more spacious than the octahedral site. However, Seeger and his collaborators[22] have more recently suggested that both tetrahedral and octahedral sites might be occupied above 40K.

In connection with the idea of Meier et al., mentioned in the previous section, one can expect that the muon may sample the fields over different types of sites due to its vibrational motion. This is to say that the wave function of a muon, centered at a particular site, can spread out to reach other neighboring sites. In addition to this, the lattice distortion around a muon may be severe enough to completely alter the local electronic structure. Therefore, the sign of the local magnetic moment density from the neutron scattering data will not determine the muon site in a ferromagnet. As stated earlier in this chapter one of the purposes of this uniaxial stress experiment is to study the muon site problem in Fe.

E. Organization of the Thesis

This thesis reports the first results of a uniaxial stress μ^+SR experiment. The experiment was performed at the Swiss Institute for Nuclear Research (SIN) at Villigen, Switzerland. Both single and polycrystal samples were used in this experiment.

Chapter II presents a brief introduction of SIN facilities, a description of the apparatus used for this work, the results of the neutron activation analysis of various impurity concentrations in the samples and the procedure of data analysis.

The theoretical background of this work is given in the next two chapters. Chapter III gives a review of some fundamental aspects in ferromagnetism. This leads to predictions of the domain wall movement in Fe in response to the externally applied stress. The occupational probability of a muon at an interstitial site of the crystal changes with the

application of uniaxial stress. Such a change will be discussed in Chapter IV in terms of the interaction between the elastic dipole of a muon and the external stress.

The experimental results are presented and explained in Chapter V. As will be seen in that chapter, the muon frequency decreases with the tensile stress applied along one of the crystal axes of Fe. Such a decrease in frequency again occurs in the polycrystal sample and it is explained in connection with the result obtained from the single crystal sample. From these results it is shown that the frequency in an Fe sample with a higher concentration of dislocations should be lower than that in a sample with a lower concentration.

II. EXPERIMENTAL DETAILS

The πE3 beam line at the Swiss Institute for Nuclear Research (SIN) was the source of the surface muons used for this work. The attractive features of this beam are the low energy and high intensity of the muons. Since the samples had small thickness, a low energy beam would have maximum stopping rate. The surface area of each sample was not large. A collimater (2mm x 5mm) was used to pass only the muons which would impinge upon the sample. This reduced the intensity of the beam significantly. If the original intensity of the muon beam had not been high the time required to stop a sufficient number of muons would have been too long.

As mentioned in the previous chapter the main feature of the present experiment is the application of external uniaxial stress to ferromagnetic specimens. Both single and polycrystal samples of Fe were used. Since the changes in physical parameters due to external uniaxial stress can be well defined in the single crystal, experiments were mainly concentrated upon the study of stress effects on the Fe single crystal.

In this chapter a brief description of the production and characteristics of the beam lines at SIN is given and this will be followed by detailed discussions on the samples, equipment and procedures.

A. The SIN Facility

The SIN User's Handbook (August 1981) is the best source for detailed information on the various beam lines at SIN; only a few

central parts related to the π E3 beam which we used are given in this section.

a. General Layout of the Accelerators and Beam Lines

The primary beam is produced by the accelerator system which consists of two separate machines, the 72 MeV injector cyclotron I and the 590 MeV ring accelerator, as shown in Figure 4. The proton beam is initially accelerated in the injector cyclotron which produces protons of 72 MeV with intensity up to 170 μA. These are injected into the ring accelerator producing a 590-MeV beam which is used for secondary beam production at two external targets. The pion beam for π E3 is produced at target station E using a 12 cm long beryllium rod.

b. π E3 Pion Beam and Surface Muons

The pion beam π E3 is a low energy beam produced at 90° from target station E (Figure 4). An additional installation was made in this beam line and is called the " π E3-appendix". The purpose this appendix is to provide an intense pion beam of extremely low momentum (40 $\sim$ 100 MeV/c) with little contamination and neutron background.

The pion beam line has been modified so that muons from the decay of pions stopped in the pion production target (so-called "surface muons") can be transported to the experimental area. The complete layout of the beam is shown in Figure 5(a) and its envelope in Figure 5(b). Figure 6 shows the measured intensities of muons as a function of the central momentum where the thickness of the degrader for electron separation is zero. The muon-positron separation for the 380 μm mylar foil is shown

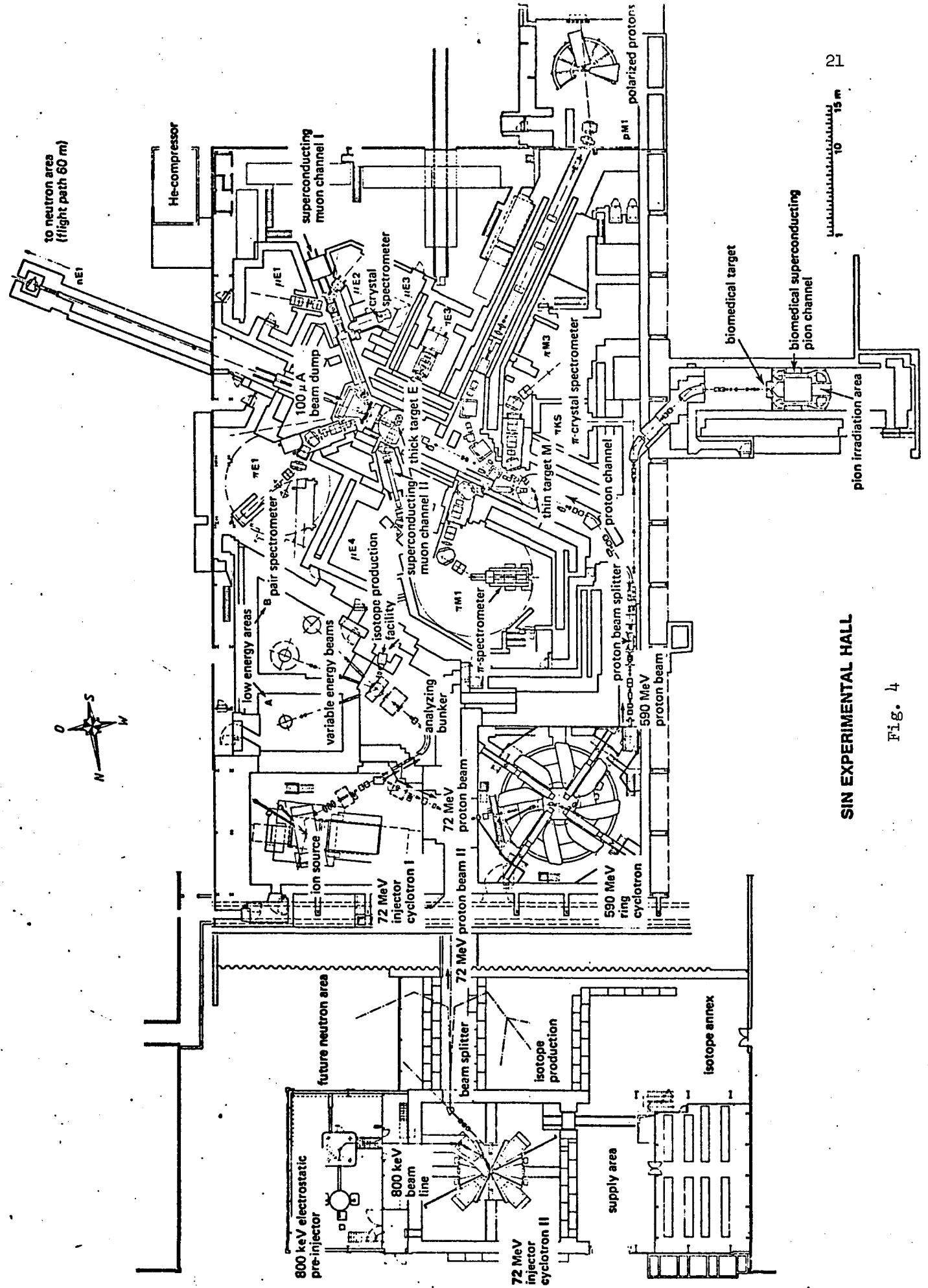
SIN EXPERIMENTAL HALL
to neutron area (flight path 60 m)
He-compressor
superconducting muon channel I
polarized protons
biomedical target
biomedical superconducting pion channel
pion irradiation area
crystal spectrometer
π-crystal spectrometer
100 μA beam dump
thick target E
thin target M
proton channel
pair spectrometer
superconducting muon channel II
isotope production facility
low energy areas
variable energy beams
analyzing bunker
π-spectrometer
proton beam splitter
590 MeV proton beam
72 MeV proton beam
72 MeV proton beam II
ion source
72 MeV injector cyclotron I
590 MeV ring cyclotron
future neutron area
beam splitter
isotope production
isotope annex
800 keV electrostatic pre-injector
800 keV beam line
supply area
72 MeV injector cyclotron II

Fig. 4

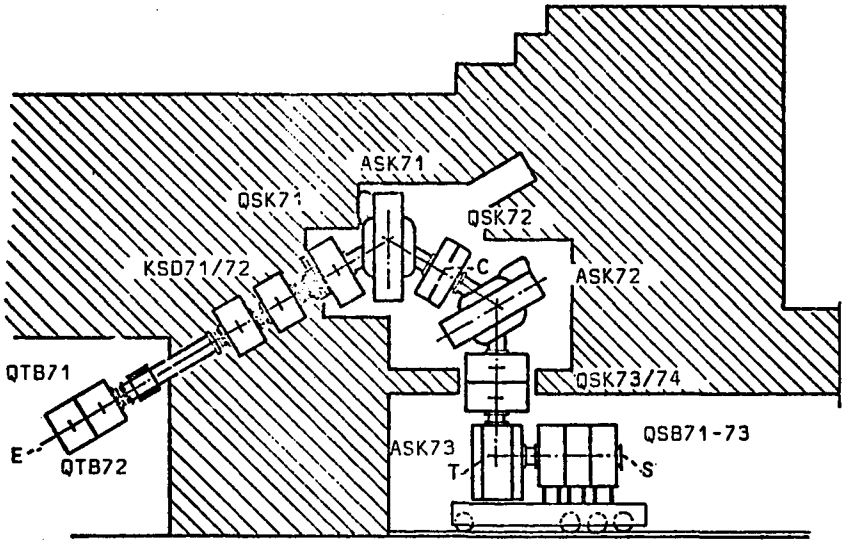

Fig. 5(a)

Lay out of the pion beam

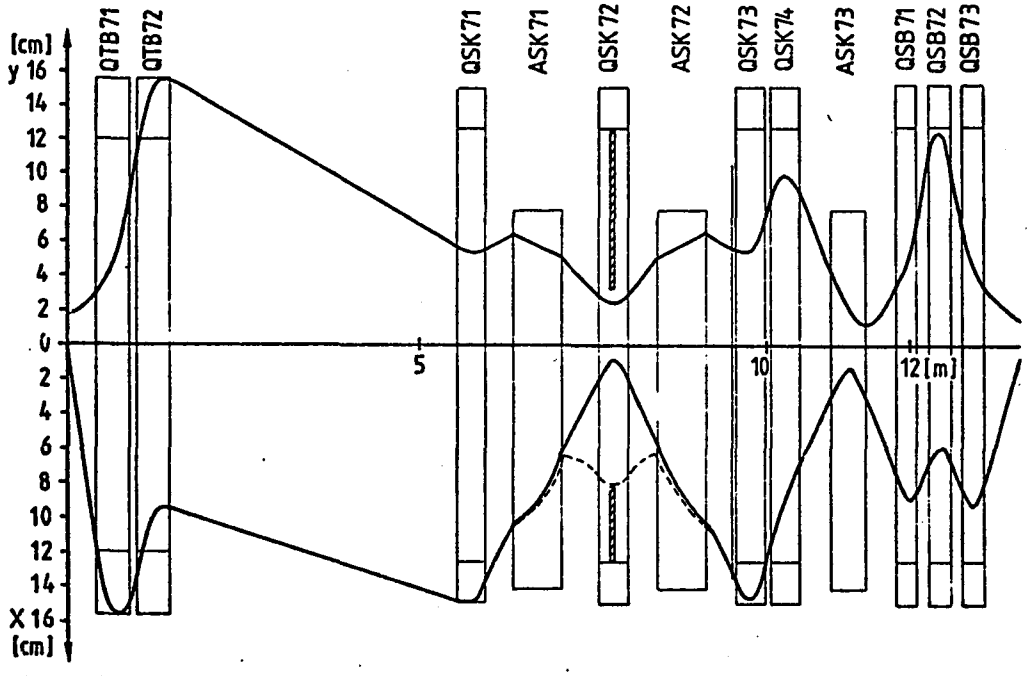

Fig. 5(b)

Envelopes of the πE3 beam with appendix

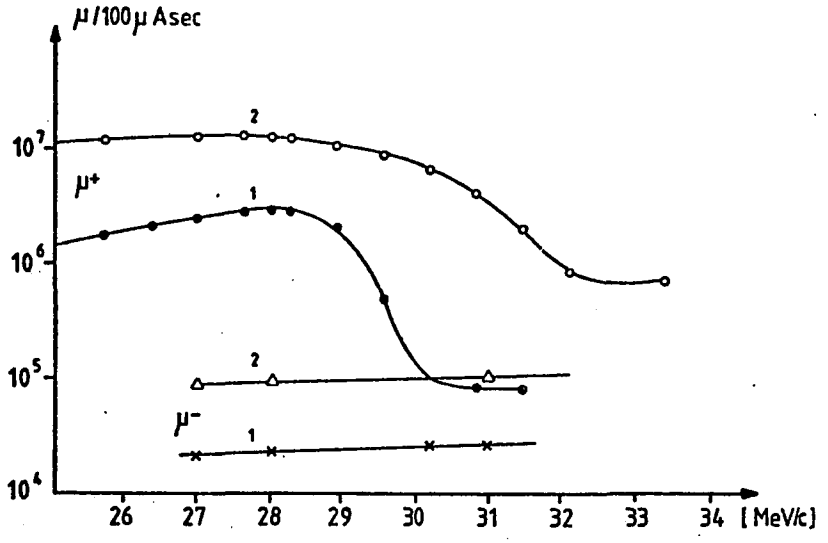

Fig. 6. Measured muon rates in the πE3 beam as a function of the central momentum in the first bending magnet. The degrader thickness for electron separation is zero. The production target is 22.2 g/cm^2 beryllium. However, the effective target length seen from the channel is only 3 cm. The accepted solid angle is 50 msr.
Curves 1:
The accepted momentum band is chosen to be $\Delta p/p$ = 4% FWHM in order to see a sharp drop in the muon rate near 29.5 MeV/c.
Curves 2:
Maximum intensities with full momentum band $\Delta p/p$ = 10% (FWHM).

in Fig. 7. Muon intensities and electron contamination for various degrader thicknesses and the magnet settings for the usual pion and muon modes are summarized in Table 2(a) and (b) respectively.

B. The Samples

The Fe single crystal sample was mainly studied in this experiment. Thus a detailed description of this particular sample will be given. This crystal was supplied by the Monocrystals Company, Cleveland, Ohio. According to the information provided by the manufacturer, the steps of growing and preparation can be summarized as follows:

1) A polycrystalline ingot was prepared by cold rolling the raw material after melting and cooling. As a result of this operation the ⟨100⟩ axis of each grain was preferentially oriented along the cylindrical axis.

2) Starting with a 3/8" diameter bar, the single crystal was grown from the center outwards and towards the surface by the anneal-strain-anneal method. The growth anneal was performed at 800°C for long periods.

3) After growth the crystal was etched in NITAL solution (5% HNO_3 acid in methanol) to expose the good material on the surface. Then, the x-ray Laue spot picture was taken to determine the orientation and angles for cutting out the desired specimen.

4) Thin wheel abrasive saws and a sharp (knife edge) single point milling tool were used to prepare the sample and sample surface.

5) The specimen was mechanically polished followed again by chemical etching to remove surface damage introduced in the shaping operation.

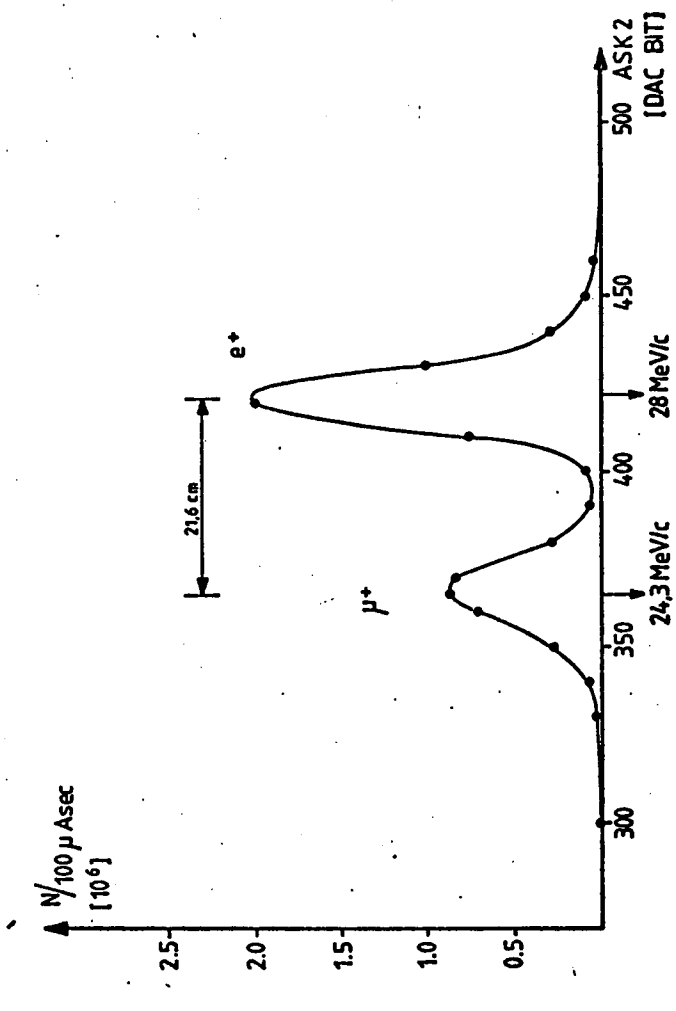

Fig. 7

Beam separation with 380 μm thick mylar degrader

Table 2(a). Muon intensities and electron contamination for various degrader thicknesses. The momentum in the first half of the beam line (before the degrader) is always 28 MeV/c.

Degrader	Momentum Band $\Delta p/p$ (FWHM)	Muons/100 μAsec		Beam Spot (cm^2) (FWHM)		Contamination e^+/μ^+ in 4 x 4 cm^2	Central Beam Momentum After Degrader
(μm Mylar)	(%)	11 m beam line	14 m beam line	11 m	14 m	Counter	(MeV/c)
0	4	$3.0 \cdot 10^6$	$2.7 \cdot 10^6$	2.4 x 3.2	2.4 x 5.2	2.0	28.0
	10	$1.4 \cdot 10^7$	$1.2 \cdot 10^7$	2.4 x 6.4	2.8 x 5.2		
190	4	$2.1 \cdot 10^6$	$1.7 \cdot 10^6$	2.4 x 5.6	2.4 x 6.4	0.1	26.3
	10	$9.8 \cdot 10^6$	$7.4 \cdot 10^6$	2.4 x 7.2	2.8 x 6.8		
380	4	$1.4 \cdot 10^6$	$1.3 \cdot 10^6$	2.4 x 10.4	4.4 x 7.2	0.04	24.3
	10	$6.1 \cdot 10^6$	$5.1 \cdot 10^6$	2.4 x 12.0	6.0 x 7.6		
570	4	$1.0 \cdot 10^6$	$1.0 \cdot 10^6$	2.8 x 15.0	4.8 x 8.0	0.1	21.8
	10	3.6×10^6	$2.8 \cdot 10^6$	1.8 x 15.0	6.0 x 8.0		

Table 2(b) Magnet settings for usual pion and muon modes

Magnet	Setting for 28 MeV/c μ^+				102 MeV/c
	no foil	190 μ	380 μ	570 μ	π^+
QTB 71	- 746	- 746	- 746	- 746	- 2734
QTB 72	+ 423	+ 423	+ 423	+ 423	+ 1540
ASK 71	+ 436	+ 436	+ 436	+ 436	+ 1588
ASK 72	+ 424	+ 395	+ 365	+ 327	+ 1575
QSK 71	- 170	- 170	- 170	- 170	- 660
QSK 72	- 165	- 165	- 165	- 165	- 1158
QSK 73	- 273	- 253	- 236	- 215	- 1045
QSK 74	+ 210	+ 210	_ 210	_ 208	+ 1200
QSB 71	- 730	- 650	-1040	-1370	-
QSB 72	+1035	+ 950	_1018	+1025	-
ASK 73	- 965	- 908	- 832	- 745	-
STA 71	+1000	+1000	+1000	+1000	+ 3300
STA 72	+ 50	+ 50	+ 50	+ 50	0
QSB 73	+ 470	+ 450	+ 450	+ 420	-

The sample thus prepared is a thin slab of dimension: 1 x 4.6 x 46.13 mm^3. The orientation of the sample is such that the ⟨100⟩ direction is along the long axis. The direction normal to the wide surface deviates from ⟨010⟩ by about 10°.

The polycrystalline Fe sample was prepared at Centre d'Etudes de Chemie Metallurgique (CECM), Vitry, France, from zone refined iron. It was annealed for 12 hours at 850°C under a purified hydrogen atmosphere. The average grain cross section was estimated to be about 2mm.

C. Neutron Activation Analysis

The purpose of this measurement was to measure the purity of the samples. It was performed by the staffs at CECM using the neutron beam of the Osiris reactor at Saclay, France. Impurities in the sample undergo a nuclear reaction with a neutron, for example,

$$^{55}Mn(n,\gamma) \rightarrow {}^{56}Mn$$

and the intensity of γ-rays subsequently emitted are compared to that for γ-rays emitted from samples with known concentration of each impurity. The general procedure is summarized as follows:

1) A small piece of material is cut from each sample and irradiated with thermal neutrons. After irradiation each piece is dissolved in acid (25% nitric acid and 75% hydrochloric).

2) The dissolved sample is put in a container and the γ-ray radiation is detected by a Ge(Li) detector connected to a multichannel analyzer. By dissolving the sample, the measurement is less dependent upon its position relative to the detector than for solid samples.

The concentrations of various impurities in the Fe ⟨100⟩ and Fe polycrystal samples are presented in Table 3 and Table 4. For better

Table 3. Impurity concentrations in units of wt PPM. Both samples were irradiated for 60 minutes with a neutron flux of 1.1×10^{14} neutrons/cm^2 sec.

Samples		
Elements	Fe <100>	Fe Polycrystal
Ce	≤ 0.8	≤ 0.5
Co	39(3)	0.21(1)
Cr	16.5 (10)	11.27 (10)
Cs	≤ 0.07	≤ 0.04
Hf	≤ 0.06	≤ 0.02
Ni	≤ 2.5	≤ 1.8
Rb	≤ 0.9	≤ 0.2
Sc	6×10^{-4}(2)	$\leq 6 \times 10^{-4}$
Ta	0.03	0.005
Zn	0.3	0.02
Zr	≤ 6	≤ 5

Table 4(a) Samples were exposed to 3×10^{12} neutrons/cm^2 sec for 1 minute

Elements	Samples: Fe <100>	Fe Polycrystal
As†	49(5)	0.31(2)
Au	$\leq$ 0.02	$\leq$ 0.02
Cu*	800(30)	1.30(4)
Cl	$\leq$ 7.9	$\leq$ 4.2
Ga	$\leq$ 3	$\leq$ 1
K	$\leq$ 1	$\leq$ 0.9
La	5(1)	$\leq$ 0.4
Mn**	500(15)	10.5(10)
Na	$\leq$ 0.14	$\leq$ 0.15
Sb	$\leq$ 0.3	$\leq$ 0.07
W	< 0.4	< 0.4

Table 4(b) Sample was exposed to 10^{14} neutrons/cm^2 sec for 1 minute

Elements	Samples: Fe <100>	Fe Polycrystal
Al	< 100***	2.0 $\pm$ 2

†Letting the radioactivity decrease for 48 hours still allowed one to see the As and Cu lines

*Checked not only on the 511 keV line but also on 1346 keV (^{64}Cu) line

**The analysis was based on the reaction $^{55}Mn(n,\gamma)\,^{56}Mn$ but the reaction $^{56}Fe\,(n,p)^{56}Mn$ interfered with the former reaction. Therefore, Mn concentration in the Fe-polycrystal sample is believed to be less than 1 PPM

***The Mn contained in the sample prevents one from obtaining an accurate measurement for the Fe <100> sample.

resolution three separate measurements were performed for each sample. It must be noted that there is an interfering effect on such impurities as Cr and Mn. Due to the following reactions

$$^{54}Fe\,(n,\alpha) \longrightarrow {}^{51}Cr$$

$$^{56}Fe\,(n,p) \longrightarrow {}^{56}Mn$$

samples appear as if they contain Cr and Mn impurities even though the samples may be free of these impurities. The concentrations of impurities so produced are believed to be about 10 PPM. Therefore, the concentration of Cr and Mn in Fe polycrystal sample is believed to be less than 1 PPM (see Tables 3 and 4).

D. The Pulling Device and Strain Gauge

Figure 8a shows the arrangement of the puller constructed at the Physics Machine Shop of the College of William and Mary. Each sample was glued to the sample holders in a specially designed jig to prevent misalignment between the stress axis and the long axis of the sample. A supporting piece made from aluminum was attached to the sample holders by two small screws while the sample was in the jig. The supporting piece was carefully released after the stress transmitting rods were engaged to the sample holders. The steps were reversed when the sample was taken out of the puller. With this process the external mechanical disturbance to the sample was minimized.

The sample holder assembly was insulated by a vacuum jacket. Ethand was circulated at a constant rate through the 1/8" copper tubing attached to the sample holder assembly. The temperature of ethand was regulated by heating and cooling. Hence the temperature in the sample was kept constant at 302°K during the entire run with a very slow variation

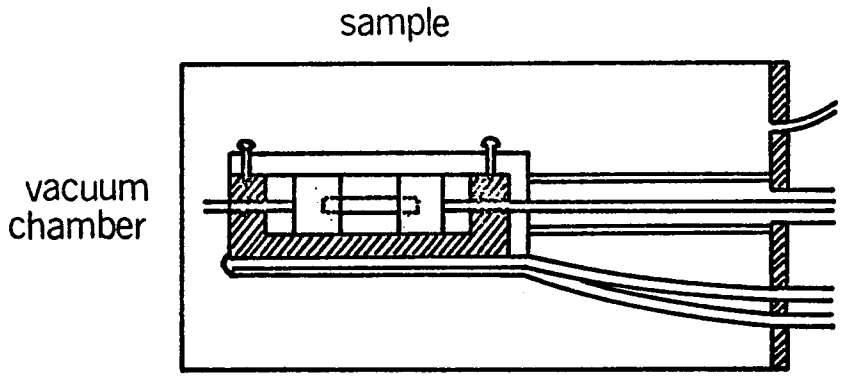

Fig. 8(a)

Sample holder assembly

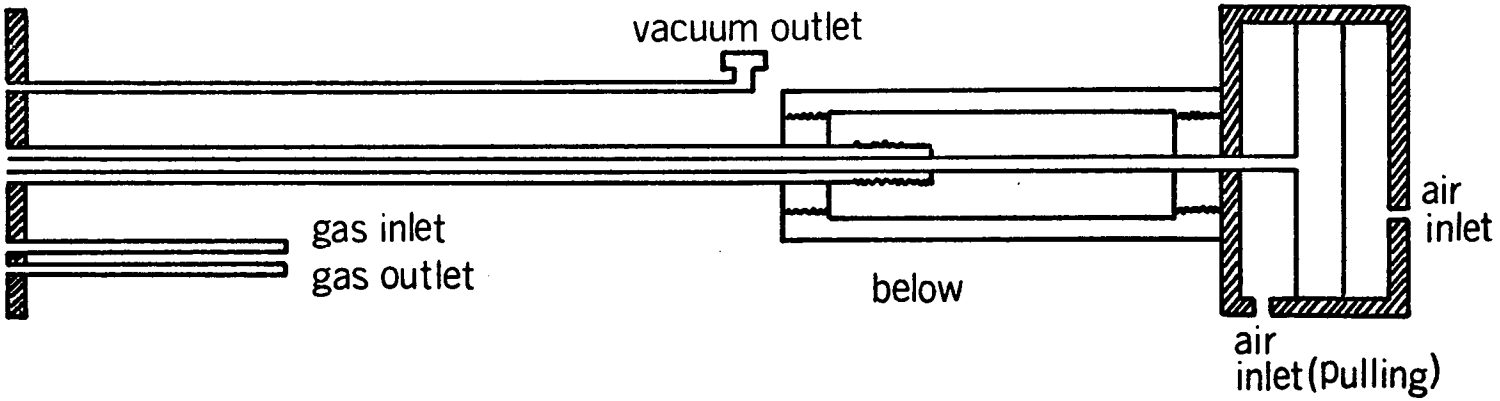

Fig. 8(b)

Piston assembly

within $\pm$ 1K. The vacuum chamber has 1" diameter windows on each side which are sealed by 3 mil thick mylar film. The mylar window on the upstream side passed muons to the sample without stopping. The other window allowed "see-through" adjustment of the sample position. The position of the sample was checked by a telescope aligned with the beam line.

The stress applied to the sample was produced by the multiplication of N_2 or air pressure by the area ratio between the sample cross-section and the piston. Figure 8b shows the piston arrangement. The tensile strain induced on the sample by the external stress was measured by a strain gauge. Strain gauges were purchased from Micro-Measurement Company, Romulus, Michigan. These wire type gauges had exactly 350Ω of resistance when unstrained and a gauge factor of 2.06 $\pm$ 0.5% which is very insensitive to a small change in temperature. The fractional changes in the resistance and the length of the gauge are related by the gauge factor as

$$\frac{\Delta \ell}{\ell_o} = \frac{1}{GF} \frac{\Delta R}{R_o}$$

The change in the resistance, ΔR, due to external stress was directly measured by the change in the voltage across the strain gauge using a nano-voltmeter. Figure 9 shows the circuit for this measurement.

E. Data Acquisition

There was no modification made for this experiment to the already existing data collection system built by the μ^+SR group at the University of Zürich. For this reason only a few general features of the system will be outlined.

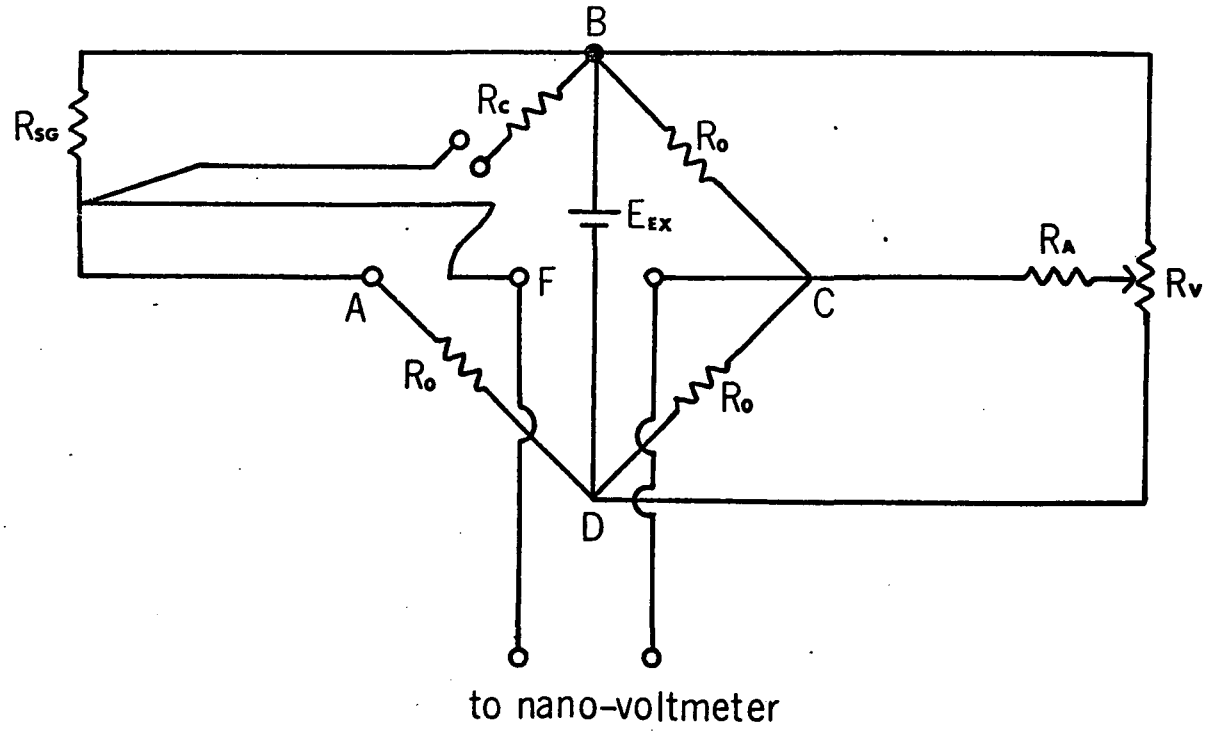

Fig. 9. Strain gauge circuit. When unstrained $R_{SG} = R_0 = 350\ \Omega$, $R_c = 3.67\ M\Omega$ is used to calibrate the change in R_{SG}. $R_A = 20$ K is for zero setting of the reading in the voltmeter when unstrained. The distance from points A and B to the strain gauge is about 12 meters. To compensate for any change in the resistance of the conducting wires, the three wires from A, B and F all have the same length.

Muons and positrons are detected by plastic scintillation detectors (NE 102) mounted via light pipes on photomultipliers (xp 2020). Figure 10 shows the arrangement of detectors and a block diagram of the μ^+SR electronics. The major functions of the electronics system which was interfaced to a PDP 11-40 are:

1) It detects a muon stopped in the sample and also the positron emitted from the decay of the corresponding muon, then, records one positron event according to the time interval between the above two detections. It distinguishes whether the positron is detected in either the forward or backward counter and records the event accordingly.

2) The system accepts only one muon event during a fixed period of time (4.5 μsec) to properly correlate the detected positron to the corresponding muon. Otherwise, the obtained histogram will be distorted.

3) To form a histogram each positron event must be recorded at the proper location in the memory space of the PDP computer. For this operation the time interval between the detection of the muon and positron is converted to a voltage signal by a TAC (Time to Amplitude Converter) and is subsequently digitized by an ADC (Analog to Digital Converter).

For these basic operations the following logic signals are used to identify the events:

$$\text{INC} : M \cdot \overline{F_1 + F_2 + F_t} = \text{incoming muon}$$

$$\text{IST} : \text{INC} \cdot \overline{(F_1 + F_2 + F_t)} = \text{incoming stopped muon}$$

$$\text{EF} : (F_1 + F_2) \cdot F_T \cdot \overline{(M + R + R_t)} = \text{forward positron}$$

$$\text{ER} : R \cdot R_T \cdot \overline{(F_1 + F_2 + F_t)} = \text{backward positron}$$

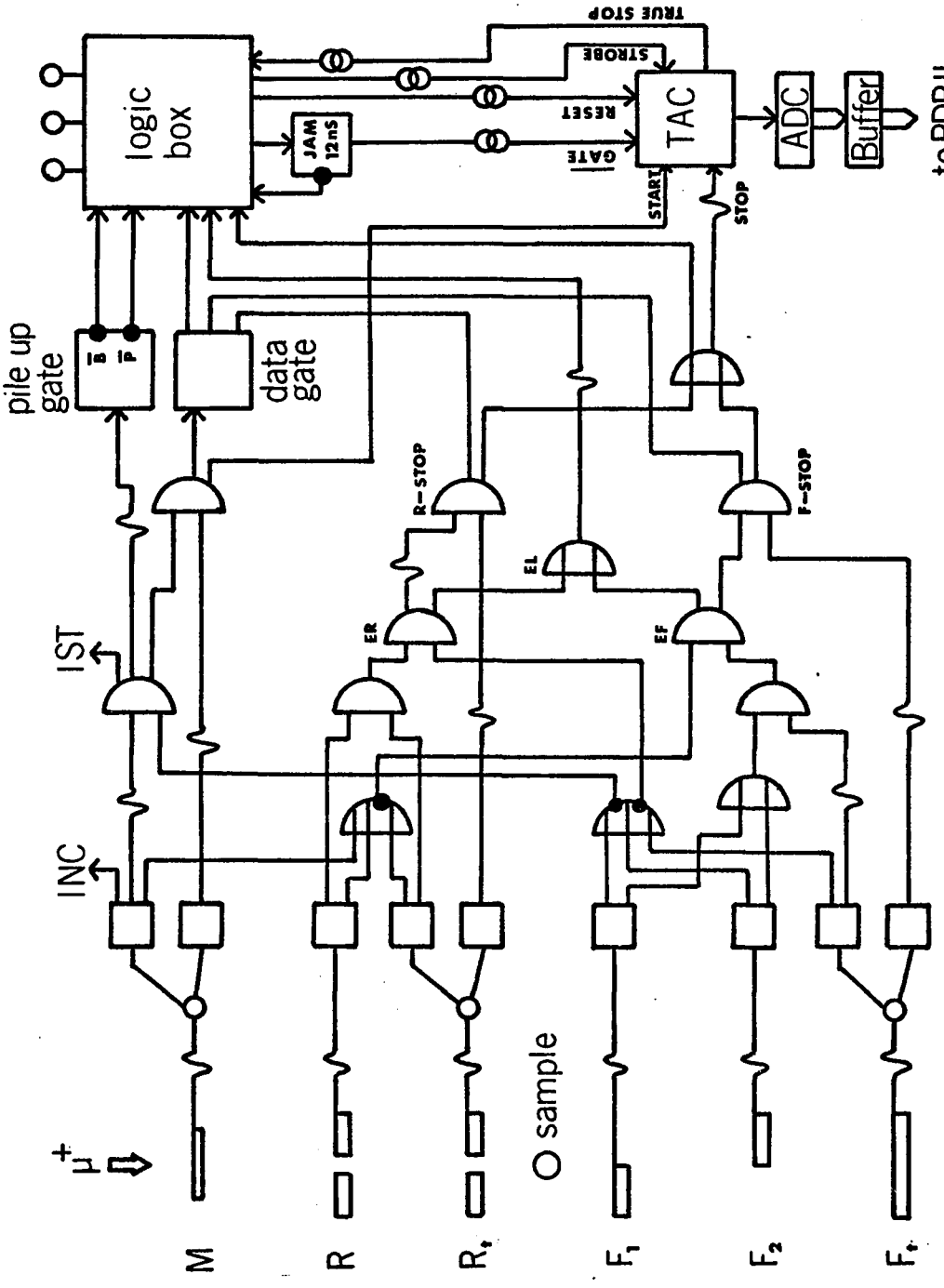

Fig. 10(a). μ^+SR electronics at πE3

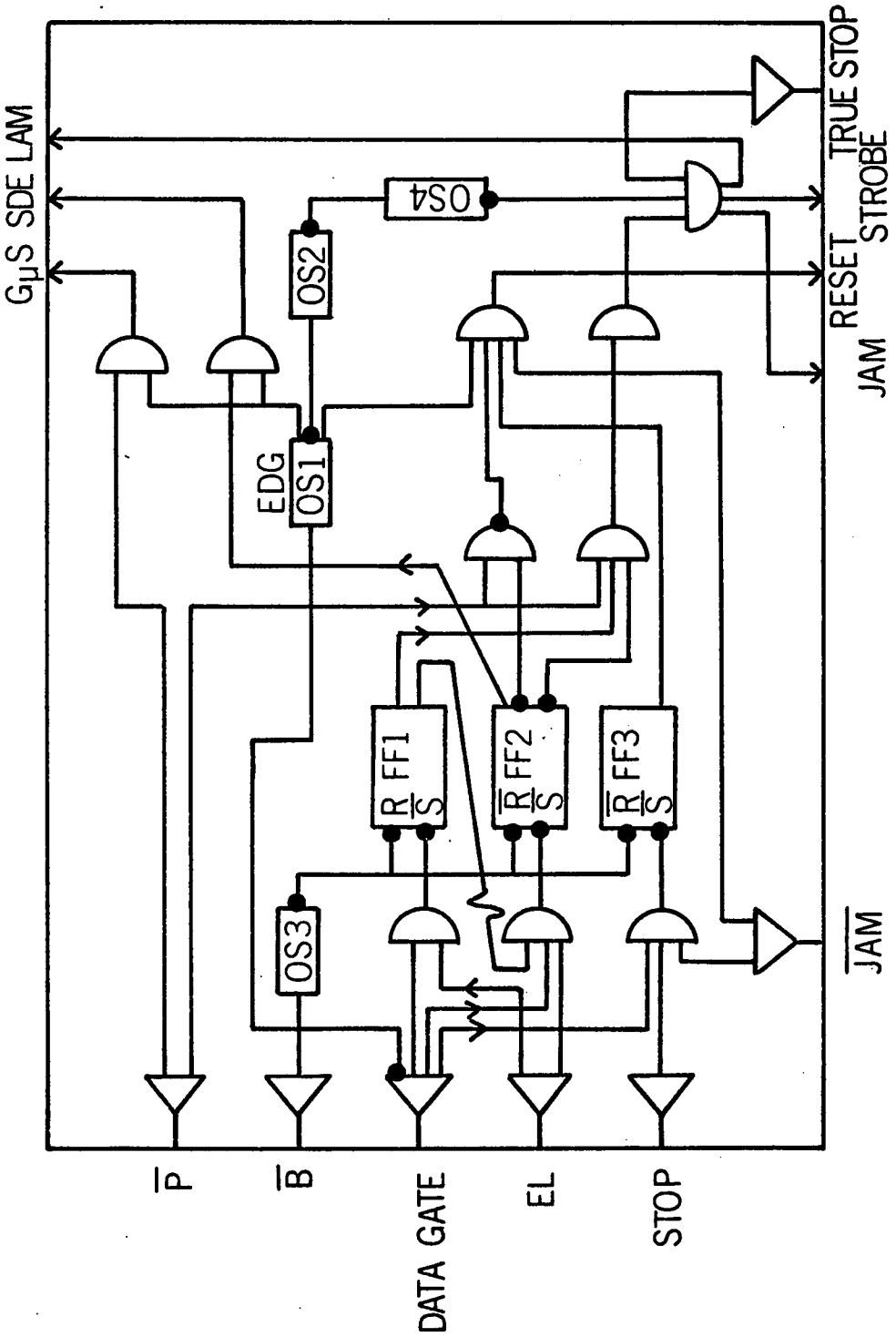

Fig. 10(b). Detailed diagram of the logic box (see Figure 10(a)).

During step (3) the system is essentially turned off for 12 μsec by a JAM signal (Fig. 10(a)) and no new muon event is accepted. The above three steps are repeated until a sufficient number of positron events (~ 3M million) is collected. When this is finished the information stored in the PDP is written onto a magnetic tape.

The data thus collected for each run consist of 8192 words on the magnetic tape followed by a block of 256 words for a run label. Each integer word in the histograms represents the total number of positrons detected between T_i and $T_i + \Delta t$. Here, Δt is the effective time per channel which was 2.14136 nano-sec for this experiment. Time zero channels were obtained by removing the anticoincidence requirements on E_F and E_R and observing muons passing through the muon and positron detectors. These were the 157th and 156th channel in the forward and backward histograms, respectively.

A detailed general description of the μ^+SR data acquisition system is found in Reference 23 and that specially for the SIN πE3 is given in Reference 24.

F. Data Analysis

The raw histograms of most of the runs were fitted to a model function obtained from equation (1.3) by including longitudinal depolarization (see Appendix B for derivation):

$$N_{F,B}(t) = N_{0_{F,B}} e^{-t/\tau_\mu} \{ 1 \pm P[F_L e^{-t/T_1} + F_T e^{-t/T_2} \cos(\omega_\mu t + \phi)] \} + BKG_{F,B} \quad (2.1)$$

where $P = A_{eff} \cdot P(t = 0)$. The parameters F_T and F_L are defined in Appendix B.

Time t is the only independent variable in the above equation. To determine the values of the unknown parameters the data were fitted to equation (2.1) using a non-linear least-square fitting routine. An improved grid-search method was employed to minimize the difference between unity and the normalized χ^2 defined below.

$$\chi^2(\vec{x}) = \sum_{i=1}^{N} \left[\frac{Y_i - F_i(\vec{x})}{\sigma_i} \right]^2 \Big/ \text{degrees of freedom} \qquad (2.2)$$

where $\vec{x} = (x_1, x_2, \ldots, x_n)$ are the variable parameters, N is the number of data points to be fitted, Y_i and σ_i^2 are the measured values and their variances and $F_i(\vec{x})$ are the values predicted by the fitting equation. Since the emitted positrons follow the Poisson distribution, the variance σ_i^2 can be replaced by F_i (see Reference 25). The number of degrees of freedom is the total number of data points minus the number of parameters.

In the actual fitting process F_L in equation (2.1) was factored out of the bracket to replace F_T by $\beta = F_T/F_L$ which approximately corresponds to the ratio between volumes of domains perpendicular and parallel to the initial muon spin orientation. The forward and backward histograms of each run were analyzed simultaneously using one value for each parameter which, in principle, should be the same in both histograms. For runs with long lasting signals the first 1000 data points from each histogram were fitted and varying the range up to 3000 points gave essentially the same results for the values of important parameters such as ω_μ, F_L/F_L, $1/T_1$ and $1/T_2$.

In other cases, for example, runs on the cold worked Fe ⟨100⟩, the oscillation amplitude damped out rapidly and replacing e^{-t/T_2} by $e^{-\sigma^2 t^2}$ gave better results. This judgment was made from the value of χ^2; with the exponential relaxation function of e^{-t/T_2}, χ^2-values obtained were not less than 1.5. Using the Gaussian function of $e^{-\ 2_t 2}$, χ^2's were close to unity. In these cases the first 350 data points were fitted. A discussion of the physical origin of the relaxation function parameter is given in Appendix A.

III. PHENOMENOLOGICAL ASPECTS IN FERROMAGNETISM*

In 1901 Piere Weiss put forward the "molecular" field hypothesis that each atom of a ferromagnetic material is a magnetic dipole and is acted upon by an intense magnetic field proportional to, and parallel to, the magnetization in the region surrounding it. This met with considerable success in accounting for spontaneous magnetization and its variation with temperature. Weiss realized that the molecular field had to be more intense than could be accounted for by ordinary magnetic forces, but he was unable to trace its origin.

It is now known that the molecular field is a representation of the net effects of exchange interactions. The elementary dipoles behave as if they were experiencing an intense magnetic field as a result of exchange interactions between them. The proportional dependence of the molecular field on the intensity of the magnetization existing in a domain reflects the fact that the net exchange couple tending to turn an ion into a particular direction will be proportional to the excess number of its neighbors already pointing in that direction. The intensity of magnetization is a measure of the number of such excess ions averaged over a volume containing a very large number of atoms.

Most known ferromagnetic substances are metallic. This fact immediately introduces a difficulty which is not really peculiar to

*Discussions on these subjects are found in references 26-31.

magnetism. The problem is the more general one of how to describe the state of motion of the electrons in a metal. When atoms combine to form a metal the most tightly bound electrons are hardly affected by the neighboring atoms and remain localized on separate nuclei. The outermost electrons, on the other hand, are as close to one nucleus as to the next and they tend to move extensively through the lattice of positive ions. The "magnetic" electrons in ferromagnetic rare earth metals are in 4f states and, being screened by the 5s and 5p electrons, probably remain tightly bound and localized on parent nuclei. In transition metals and their alloys, the electrons responsible for ferromagnetism are those which are derived from 3d states of free ions and unscreened from neighboring atoms in a solid sample. Therefore, they probably exist in states which are itinerant, or at least intermediate between being localized on parent nuclei and being freely itinerant.

The atomic ground states of 3d transition elements as determined by Hund's rule predict net magnetic moments from the unpaired electrons in 3d shells. The values of the magnetization at 0 K, extrapolated from low temperature measurements, show that each atom of Fe, Ni and Co carries 2.22 μ_B, 0.6 μ_B and 1.7 μ_B, respectively, where μ_B is the Bohr magneton. The Weiss model for localized electrons cannot explain these non-integral numbers of Bohr magnetons. On the other hand, the collective-electron model due mainly to Stoner deals with almost free itinerant electrons. This model provides a satisfactory general account of the main magnetic and thermal properties of transition metals and alloys. However, the collective electron model fails to explain some important facts in ferromagnetism such as the existence of spin

waves. Formulating a single simple theory which deals adequately with the localized and itinerant characters of electrons at the same time has not been successful.

Despite such difficulties in the theoretical description of ferromagnetism the role of ferromagnetic materials and their alloys is very important in technology. For this reason the magnetic and mechanical properties of ferromagnetic substances have been studied extensively for the last several decades. The theories developed during this period successfully describe the physical process of ferromagnetic states of a material in response to external influence. External stress, especially a uniaxial stress, applied to a ferromagnetic material alters its magnetic states through the change in mechanical structure of the material. Such effects by the external uniaxial stress on the ferromagnetic states of a material are seen from the magnetic domain reorientation, motion of Bloch walls, the change in the magnitude of the spontaneous magnetization and stress induced anisotropy. In this chapter the basic phenomenological aspects in ferromagnetism which are related to the uniaxial stress μ^+SR experiment will be discussed.

A. Exchange Theory of Ferromagnetism

The most general definition of the exchange energy for a two-electron system with a Hamiltonian not containing terms describing the magnetic interaction is connected to the possibility that two types of ground states may exist: a singlet with zero spin S = 0 and an energy $^1\epsilon$, and a triplet with S = 1 and an energy $^3\epsilon$. The exchange energy J is defined as half the difference between these two energies:

$$J = \frac{1}{2}\left({}^{1}\epsilon - {}^{3}\epsilon\right) \tag{3.1}$$

From this one sees that for $J > 0$ energy ${}^{3}\epsilon < {}^{1}\epsilon$, and in the ground triplet state the spins of two electrons are parallel (more precisely, the projections of the spins onto the quantization axis have the same sign in the case of ferromagnetism), while for $J < 0$ the spins would be antiparallel (case of antiferromagnetism).

The definition in equation (3.1) suggests a means of writing the exchange part of the electrostatic energy for a two-electron system as the scalar product of spin vectors. To do this, one writes the energy of the system as

$$\epsilon = \frac{1}{2}\left({}^{1}\epsilon + {}^{3}\epsilon\right) - \frac{1}{2}\kappa\left({}^{1}\epsilon - {}^{3}\epsilon\right) \quad (\kappa = \pm 1) \tag{3.2}$$

here, for $\kappa = 1$ $\epsilon = {}^{3}\epsilon$, and for $\kappa = -1$ $\epsilon = {}^{1}\epsilon$. The square of the total spin vector for the system $\vec{S} = \vec{S}_1 + \vec{S}_2$ in units of $\hbar$ is

$$S^2 = \frac{3}{2} + 2\,\vec{S}_1 \cdot \vec{S}_2 = S(S+1) \tag{3.3}$$

Therefore, one gets an operator

$$\left(\frac{1}{2} + 2\,\vec{S}_1 \cdot \vec{S}_2\right) \tag{3.4}$$

with an eigenvalue $[S(S + 1) - 1]$: for $S = 0$ the eigenvalue is -1, and for $S = 1$ it is $+1$. The eigenvalues coincide with the possible values of κ in equation (3.2).

By replacing κ in equation (3.2) with (3.4), one obtains the following energy operator for the system:

$$\mathcal{H} = \epsilon_0 - 2J\,\vec{S}_1 \cdot \vec{S}_2 \tag{3.5}$$

which has the required eigenfunctions relative to the spin and accurate eigenvalues of the energy. Here, $\epsilon_0 = ({}^1\epsilon + {}^3\epsilon)/4$ is the mean energy of all four spin states. Equation (3.5) does not depend on any of the assumptions made during the usual treatment of the problem.

Denoting $\phi_a(\vec{r}_1)$ and $\phi_b(\vec{r}_2)$ as the single electron wavefunctions for the electrons positioned at r_1 and r_2 with spin states a and b, respectively, the exchange energy J can be expressed as[29,31,32]

$$J = e^2 \iint \frac{\phi_a^*(\vec{r}_1)\,\phi_b^*(\vec{r}_2)\,\phi_a(\vec{r}_2)\,\phi_b(\vec{r}_1)}{|\vec{r}_1 - \vec{r}_2|}\, d\vec{r}_1\, d\vec{r}_2 \tag{3.6}$$

which is the exchange integral. Equation (3.6) was derived by neglecting the overlap integral

$$|S_{ab}|^2 = \int \phi_a^*(\vec{r}_1)\,\phi_b(\vec{r}_2)\,\phi_a(\vec{r}_2)\,\phi_b(\vec{r}_1)\, d\vec{r}_1\, d\vec{r}_2 \tag{3.7}$$

Suppose the two electrons belong to the same atom, but do not complete a closed shell. The form of the Coulomb interaction and of the atomic orbitals ϕ_a and ϕ_b is such that J is positive; the electron spins tend to line up to make the maximum total spin consistent with the numbers of independent states to be filled in the shell. This is Hund's rule, which explains why the electrons in an incomplete d-shell of an ion of a transition metal tend to combine to give a large permanent magnetic moment to the ion.

However, we are concerned here with the interaction between the spins of electrons on different ions. It turned out that J almost

always comes out negative, favoring antiparallel spins on neighboring sites. The simplest case of this is the Heitler-London model of the hydrogen molecule, where the bonding state has electrons paired. On this basis, therefore, it is difficult to explain the fact that many metals, usually "transition" elements, are ferromagnetic. The problem is further complicated by the fact that the d-electrons are not strictly localized on particular ions but lie in states that overlap from atom to atom to form a narrow band. This band, in turn, hybridizes with the ordinary s-band, where electrons conduct very freely. Despite these difficulties the Hamiltonian in equation (3.5) successfully explains many phenomenological aspects in ferromagnetism.

In problems concerning ferromagnetism usually only the spin dependent term of equation (3.5) is of interest. For two atoms, i and j, that have one electron each the exchange Hamiltonian is

$$\mathcal{H} = -2J_{ij}\,\vec{S}_i \cdot \vec{S}_j \tag{3.8}$$

where J_{ij} is the exchange integral for the two electrons. If each atom has more than one electron with an unapired spin, the exchange Hamiltonian is

$$\mathcal{H} = -2J_{ij}\,\vec{S}_i \cdot \vec{S}_j \tag{3.9}$$

where $S_i = \sum_i S_i$ and $S_j = \sum_j S_j$ are the total spins of atoms i and j, respectively. Here, it is assumed (a) that all the electrons have the same exchange integral J_{ij} and (b) that the exchange between electrons of the same atom is constant, and hence can be omitted. Further, the exchange integral is usually neglected except for nearest neighbors. The

Hamiltonian of an entire crystal is

$$\mathcal{H} = -2 \sum_{i>j} J_{ij} \vec{S}_i \cdot \vec{S}_j$$

where the summation on j is over the nearest neighbors of atom i. If the exchange integral J_{ij} is isotropic, equal to J_e, one gets

$$\mathcal{H} = -2 J_e \sum_{i,j} \vec{S}_i \cdot \vec{S}_j \tag{3.10}$$

In certain problems, particularly in domain theory, it is both appropriate and convenient to consider the spin matrix operator of equation (3.10). For a one-dimensional array of spins making small angles with neighboring ones, this equation can be rewritten as

$$\mathcal{H} = E = -2 J_e S^2 \sum_j \cos \phi_{ij} \tag{3.11}$$

where ϕ_{ij} is the angle between the directions of the classical spin angular momentum vectors. If the angles between neighboring spins are very small, $\cos \phi_{ij} \simeq 1 - \frac{1}{2} \phi_{ij}^2$. The variable part of the exchange energy is given by

$$E = J_e S^2 \sum \phi_{ij}^2 \tag{3.12}$$

Let $\hat{U}_i$ and $\hat{U}_j$ be vectors parallel to the spin vectors of adjacent atoms i and j, and let r_{ij} be the displacement vector between the atoms. Then

$$\cos \phi_{ij} = \hat{u}_i \cdot \hat{u}_j = \alpha_{1i} \alpha_{1j} + \alpha_{2i} \alpha_{2j} + \alpha_{3i} \alpha_{3j} \tag{3.13}$$

where α_1, α_2 and α_3 are the direction cosines of a unit vector. Since the angle between the unit vectors $\hat{U}_i$ and $\hat{U}_j$ is small, the direction

cosines of $\hat{U}_j$ may be expanded in a Taylor series in the direction cosines of $\hat{U}_j$. For example,

$$\alpha_{ii}\alpha_{ij} = \alpha_{ii}\left(\alpha_{ii} + \vec{r}_{ij}\cdot\nabla\alpha_{ii} + \frac{1}{2}(\vec{r}_{ij}\cdot\nabla)^2\alpha_{ii} + \cdots\right)$$

Substituting this expression into equation (3.13), one can calculate the sum in equation (3.12). In the case of a cubic crystal, it can be shown that

$$\sum_j \cos\phi_{ij} = z + \frac{1}{6}\sum_j r_{ij}^2\,\hat{u}\cdot\nabla^2\hat{u}\,, \tag{3.14}$$

where the subscript on $\hat{U}_i$ was omitted. By considering only the variable part of the energy, the exchange energy is therefore given by

$$\mathcal{H} = E = -\frac{J_e S^2}{3}\sum_j r_{ij}^2\,\hat{u}\cdot\nabla^2\hat{u}$$

Using a vector identity, the above equation can be written as

$$\mathcal{H} = E = \frac{J_e S^2}{3}\sum_i r_{ij}^2\left[(\nabla\alpha_1)^2 + (\nabla\alpha_2)^2 + (\nabla\alpha_3)^2\right]$$

For cubic structure, either simple, body-centered, or face-centered, the expression $\sum_j r_{ij}^2$ is equal to $6a^2$, where a is the lattice spacing. Hence one gets finally

$$\mathcal{H} = E = 2J_e S^2 a\left[(\nabla\alpha_1)^2 + (\nabla\alpha_2)^2 + (\nabla\alpha_3)^2\right] \tag{3.15}$$

as the exchange energy for one cube of edge a.

B. Crystalline Anisotropy

The exchange energy depends on the scalar product of $\vec{S}_i\cdot\vec{S}_j$ which is invariant with respect to the choice of the coordinate system.

Experimentally, however, it is found that the magnetization tends to lie along certain crystallographic axes. This indicates that the internal energy of a magnetic system depends on the direction of the magnetization. An energy of this kind is called a magnetic anisotropy. Generally the magnetic anisotropy energy possesses the crystal symmetry of the material, and we call this a crystalline anisotropy.

The existence of crystalline anisotropy may be demonstrated by the magnetization curves of single crystal specimens. Magnetization curves for single crystals of Fe, Ni, and Co for various orientations of the applied field with respect to the crystal axes for room temperature are shown in Figure 11. It is clear that much smaller fields are required to magnetize the crystals to saturation along certain directions than others. These directions are the easy magnetization directions of ferromagnetic substances.

For cubic crystals such as Fe and Ni the anisotropy energy can be expressed in terms of the direction cosines (α_1, α_2, α_3) of the magnetization with respect to the three edges of the cube. The anisotropy energy can be expressed in a polynomial series in α_1, α_2 and α_3. Those terms which include odd powers of the α_i, must vanish because a change in sign of any of the α_i should bring the magnetization vector to a direction which is equivalent to the original direction. The expression must be invariant to the interchange of any two α_i's, so that the terms of the form $\alpha_i^{\ell}\,\alpha_j^{m}\,\alpha_k^{n}$ must have, for any given combination of ℓ, m, n, the same coefficient for any interchange of i, j and k. The first term, therefore, should have the form $\alpha_1^2 + \alpha_2^2 + \alpha_3^2$, which is always 1.

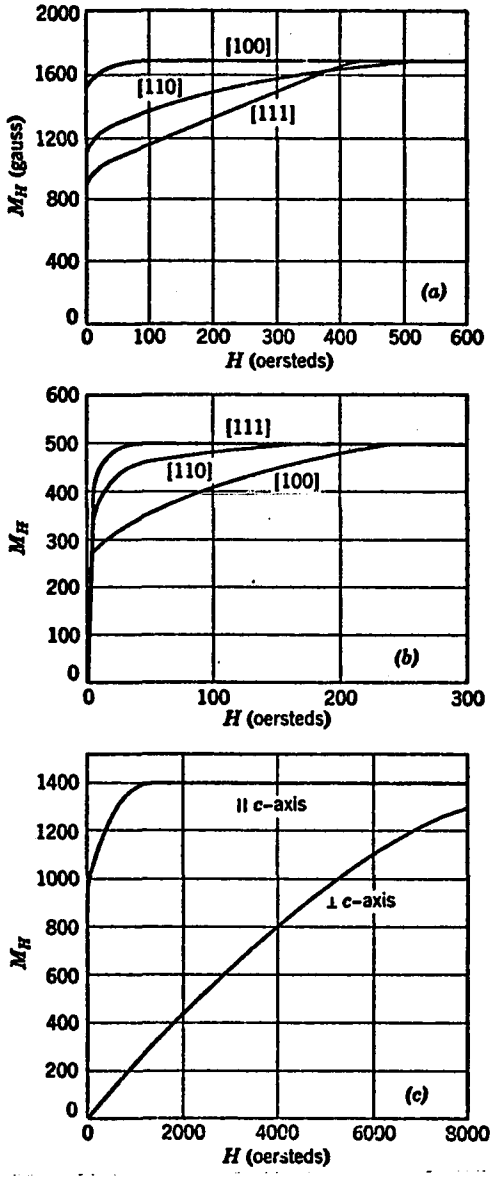

Fig. 11. Magnetization curves of single crystals of (a) iron, (b) nickel, and (c) cobalt. The direction of the applied field with respect to the crystallographic axis is indicated for each curve. (After Honda and Kaya.)

Next is the fourth order term which can be reduced to the form $\sum_{i>j} \alpha_i^2 \alpha_j^2$ by the relation

$$\alpha_1^4 + \alpha_2^4 + \alpha_3^4 = 1 - 2(\alpha_1^2\alpha_2^2 + \alpha_2^2\alpha_3^2 + \alpha_1^2\alpha_3^2)$$

Furthermore, by the relations

$$\alpha_1^6 + \alpha_2^6 + \alpha_3^6 = 1 - 3(\alpha_1^2\alpha_2^2 + \alpha_2^2\alpha_3^2 + \alpha_1^2\alpha_3^2) + 3\alpha_1^2\alpha_2^2\alpha_3^2$$

$$\alpha_1^4\alpha_2^2 + \alpha_2^4\alpha_3^2 + \alpha_3^4\alpha_1^2 + \alpha_2^4\alpha_1^2 + \alpha_3^4\alpha_2^2 + \alpha_1^4\alpha_3^2 = 3(\alpha_1^2\alpha_2^2 + \alpha_2^2\alpha_3^2 + \alpha_3^2\alpha_1^2) - 9\alpha_1^2\alpha_2^2\alpha_3^2$$

every sixth order term can be reduced to $\sum_{j>i} \alpha_i^2 \alpha_j^2$ and $\alpha_1^2\alpha_2^2\alpha_3^2$. Thus we have the expression

$$E_a = K_1(\alpha_1^2\alpha_2^2 + \alpha_2^2\alpha_3^2 + \alpha_1^2\alpha_3^2) + K_2\alpha_1^2\alpha_2^2\alpha_3^2 + \cdots \qquad (3.16)$$

where K_1 and K_2 are the anisotropy constants. For Fe at room temperature[33]

$$K_1 = 4.8 \times 10^5 \ erg/cm^3$$

$$K_2 = \pm 5 \times 10^4 \ erg/cm^3$$

and for Ni at room temperature,

$$K_1 = -4.5 \times 10^4 \ erg/cm^3$$

$$K_2 = 2.34 \times 10^4 \ erg/cm^3$$

When $K_1 > 0$ the first term takes on its minimum value at all directions of [[100]], whereas when $K_1 < 0$ it does so at all directions of [[111]]. These, then are the directions of easy magnetization.

The origin of the anisotropy energy is believed to be the result of the combined effects of the spin-orbit interaction and the partial quenching of the orbital angular momentum (by inhomogeneous crystalline electric fields and by orbital exchange interactions with neighboring atoms). In other words, the magnetization of the crystal "sees" the crystal lattice through the agency of the orbital motion of the electrons; the spin interacts with the orbital motion by means of the spin-orbit coupling and the orbital motion in turn interacts with the crystal structure by means of electrostatic fields and overlapping wave functions associated with the neighboring atoms in the lattice.

C. Magnetostriction and Magnetoelastic Energy

When a magnetic substance is exposed to a magnetic field, its dimensions change. This effect is called magnetostriction. It was discovered as long ago as 1842 by Joule, who showed that an iron rod increased its length when it was magnetized lengthwise by a weak field. The fractional change in length $\Delta l/l$ is simply a strain, and, to distinguish it from the strain ϵ caused by an applied stress, it is traditionally denoted by a symbol λ :

$$\lambda = \Delta l/l$$

The value of λ measured at magnetic saturation, or technical saturation, is called the saturation magnetostriction λ_s.

Magnetostriction occurs in all pure substances. However, even in strongly magnetic substances, the effect is small: λ_s is typically of the order of 10^{-5}. The smallness of this strain may be

better appreciated if it is translated into terms of stress. If Young's modulus is 30 x 10^6/PSI, a strain of 10^{-5} would be produced by an applied stress of only 300 PSI or 0.2 kg/mm^2. In weakly magnetic substances the effect is even smaller, by about two orders of magnitude, and can be observed only in very strong fields.

Although the direct magnetostrictive effect is small there exists an inverse effect which causes such properties as permeability and the size of the hysteresis loop to be highly dependent upon stress in many materials. Magnetostriction therefore has many practical consequences, and a great deal of research has accordingly been devoted to it.

The value of the saturation longitudinal magnetostriction λs can be positive, negative, or, in some alloys, zero. The value of λ depends on the extent of magnetization and hence on the applied field. Figure 12 shows a typical variation of λ with H for a substance with positive magnetostriction.

The magnetoelastic energy is that part of the energy of a crystal which arises from the interaction between the magnetization and the mechanical strain of the lattice. The magnetoelastic energy is defined to be zero for an unstrained lattice. It must be made clear that this strain interacting with the magnetization is a spontaneous deformation of the lattice.

The close physical relationship which exists between the anisotropy and magnetostriction is not revealed clearly in the standard discussions of the energy relationships in ferromagnetics. It is of

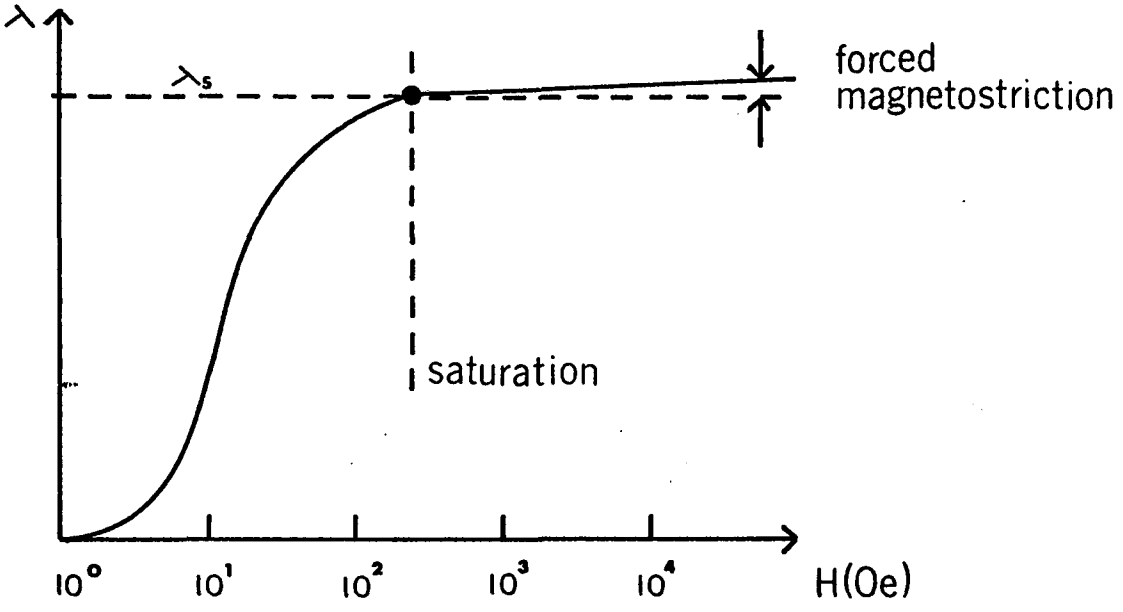

Fig. 12. Variation of magnetostriction with field H (schematic)

primary importance to recognize that there will be no linear magnetostriction if the anisotropy energy is independent of the state of strain of the crystal. Magnetostriction occurs because the anisotropy energy depends on the strain in such a way that the stable state of the crystal is deformed with respect to a cubic lattice. That is, a crystal will deform spontaneously if to do so will lower the energy.

The mathematical expression of magnetostriction has been derived by many authors. Since the magnetoelastic energy plays one of the most important roles in the uniaxial stress experiment, a detailed treatment will be given in this section. Outlined below is the derivation by Kittel[34] following the discussion of Becker and Akulov.

The elastic energy density in a cubic crystal is given by (Love, 1944, p. 160)[35]

$$f_{el} = \frac{1}{2} C_{11} (e_{xx}^2 + e_{yy}^2 + e_{zz}^2) + \frac{1}{2} C_{44} (e_{xy}^2 + e_{yz}^2 + e_{zx}^2) + C_{12} (e_{yy} e_{zz} + e_{xx} e_{zz} + e_{xx} e_{yy}) \tag{3.17}$$

where the C_{ij} are the elastic moduli and the e_{ij} are strains. The anisotropy energy density in an unstrained cubic crystal is of the form

$$f_K = K (\alpha_1^2 \alpha_2^2 + \alpha_2^2 \alpha_3^2 + \alpha_3^2 \alpha_1^2)$$

to the first order. To express the dependence of the anisotropic energy on the strain we expand the energy in a Taylor's series in the strain:

$$f_K = (f_K)_o + \sum_{i>j} (\partial f_K / \partial e_{ij})_o e_{ij} + \cdots\cdots \tag{3.18}$$

Considering the lowest order terms dependent on orientation, we may take

from symmetry considerations

$$\frac{\partial f_K}{\partial e_{ii}} = B_1 \alpha_i^2$$
$$\frac{\partial f_K}{\partial e_{ij}} = B_2 \alpha_i \alpha_j \tag{3.19}$$

where B_1 and B_2 are constants which may in principle be calculated knowing the details of the interactions in the solids. The B's are called magnetoelastic coupling constants. Substituting equation (3.19) into equation (3.18), we get

$$f_K = K_1 (\alpha_1^2\alpha_2^2 + \alpha_2^2\alpha_3^2 + \alpha_3^2\alpha_1^2) + B_1 \sum_i \alpha_i^2 e_{ii}^2 + B_2 \sum_{i<j} \alpha_i \alpha_j e_{ij} \tag{3.20}$$

The equilibrium configuration of the crystal, that is, the stable state of strain, when magnetized in the direction $\hat{\alpha}$ may be found by minimizing the total energy $f = f_{el} + f_k$ with respect to the e_{ij}. Since we have six independent components of e_{ij}'s, there will be six equations for $\partial f / \partial e_{ij} = 0$. Solving these simultaneous equations, the solutions are obtained:

$$e_{ii} = \frac{B_1 [C_{12} - \alpha_i^2 (C_{11} + 2C_{12})]}{(C_{11} - C_{12})(C_{11} + 2C_{12})}$$
$$e_{ij} = -B_2 \alpha_i \alpha_j / C_{44} \qquad (i \neq j) \tag{3.21}$$

The conventional first order magnetostriction equation which is frequently used in the analysis of experimental measurements on cubic crystals is

$$\frac{\delta l}{l} = \frac{3}{2}\lambda_{100} (\alpha_1^2\beta_1^2 + \alpha_2^2\beta_2^2 + \alpha_3^2\beta_3^2 - \tfrac{1}{3}) + 3\lambda_{111} (\alpha_1\alpha_2\beta_1\beta_2 + \alpha_1\alpha_3\beta_1\beta_3 + \alpha_2\alpha_3\beta_2\beta_3) \tag{3.22}$$

where $\hat{\alpha} = (\alpha_1, \alpha_2, \alpha_3)$ is the unit vector in the direction of the magnetization, $\hat{\beta} = (\beta_1, \beta_2, \beta_3)$ is a unit vector in the direction in which δl is measured: λ_{100} and λ_{111} are the saturation magnetostrictions in the directions $\langle 100 \rangle$ and $\langle 111 \rangle$, respectively. The next step is to relate the magnetostriction constants λ_{100} and λ_{111} to the magnetoelastic coupling constants, B_1 and B_2, which have more fundamental significance.

Suppose a position vector r between two points of an unstrained crystal becomes $\vec{r}'$ by the strain induced in the crystal. The components $\vec{r}'$ can be expressed in terms of the components of $\vec{r}$:

$$x_i' = (1 + e_{ii}) x_i + \sum_{i<j} \frac{1}{2} e_{ij} x_j$$

hence

$$\delta(l^2) = 2\delta l \cdot l = 2l^2 \sum_{i,j} e_{ij} \beta_i \beta_j$$

From this we have

$$\frac{\delta l}{l} = \sum_{i,j} e_{ij} \beta_i \beta_j \tag{3.23}$$

On substituting the values of the e_{ij} given by equation (3.20) we get

$$\begin{aligned} \frac{\delta l}{l} = &- \frac{B_1}{C_{11} - C_{12}} (\alpha_1^2 \beta_1^2 + \alpha_2^2 \beta_2^2 + \alpha_3^2 \beta_3^2) + \frac{3 C_{12} B_1}{(C_{11} + 2C_{12})(C_{11} - C_{12})} \\ &- \frac{B_2}{C_{44}} (\alpha_1 \alpha_2 \beta_1 \beta_2 + \alpha_1 \alpha_3 \beta_1 \beta_3 + \alpha_2 \alpha_3 \beta_2 \beta_3) \end{aligned} \tag{3.24}$$

which may be written in the form of equation (3.22) if we set

$$\lambda_{100} = -\frac{2}{3} \frac{B_1}{C_{11} - C_{12}} \tag{3.25}$$

$$\lambda_{111} = -\frac{1}{3} \frac{B_2}{C_{44}}$$

and drop a residual term which is constant with respect to $\hat{\alpha}$ and $\hat{\beta}$. The room temperature values of these parameters in Fe are:[26,33]

$$\lambda_{100} = 21 \times 10^{-6}$$
$$\lambda_{111} = -21.2 \times 10^{-6}$$
$$C_{11} = 2.41 \times 10^{12} \text{ dyne cm}^{-2}$$
$$C_{12} = 1.46 \times 10^{12} \text{ dyne cm}^{-2}$$
$$C_{44} = 1.21 \times 10^{12} \text{ dyne cm}^{-2}$$
$$B_1 = -2.9 \times 10^{6} \text{ erg/cm}^3$$
$$B_2 = 6.4 \times 10^{7} \text{ erg/cm}^3 \quad .$$

So far, only the spontaneous deformation of the crystal has been discussed. The next thing one needs to consider is the contribution of external stress to the magnetoelastic energy of the crystal. Suppose a uniform tensile stress of magnitude σ is applied to a crystal such that γ_1, γ_2, γ_3 are the direction cosines of σ with respect to the crystal axes. The stress components are $\sigma_{ij} = \sigma \gamma_i \gamma_j$. The resulting strains are:

$$\begin{aligned} e_{ii} &= -\sigma \left[(S_{11} - S_{12}) \gamma_i^2 + S_{12} \right] \\ \epsilon_{ij} &= -\tfrac{1}{2} \sigma S_{44} \gamma_i \gamma_j \end{aligned} \tag{3.26}$$

where s_{ij}'s are the elastic compliances. By substituting the above expressions into equation (3.20), we have

$$\begin{aligned} f_{me} = -B_1 \sigma \left[(S_{11} - S_{12}) (\alpha_1^2 \gamma_1^2 + \alpha_2^2 \gamma_2^2 + \alpha_3^2 \gamma_3^2) \right] \\ - B_2 \sigma S_{44} (\alpha_1 \alpha_2 \gamma_1 \gamma_2 + \alpha_2 \alpha_3 \gamma_2 \gamma_3 + \alpha_3 \alpha_1 \gamma_3 \gamma_1) \end{aligned} \tag{3.27}$$

Equation (3.27) can be rewritten using equation (3.25). The total energy

$f = f_k + f_{me}$ can be written as

$$f_{k,me} = K_1(\alpha_1^2\alpha_2^2 + \alpha_2^2\alpha_3^2 + \alpha_3^2\alpha_1^2) - \frac{3}{2}\lambda_{100}\sigma(\alpha_1^2\gamma_1^2 + \alpha_2^2\gamma_2^2 + \alpha_3^2\gamma_3^2)$$
$$-3\lambda_{111}\sigma(\alpha_1\alpha_2\gamma_1\gamma_2 + \alpha_2\alpha_3\gamma_2\gamma_3 + \alpha_3\alpha_1\gamma_3\gamma_1) \qquad (3.28)$$

Equation (3.28) represents the interaction between the domain magnetization and the external uniaxial stress. As a result of such an interaction, domains in a specimen rearrange in response to the applied stress.

D. Ferromagnetic Domains and Domain Walls

The concept of magnetic domains was hypothesized by Weiss along his molecular field theory. In the unmagnetized state a ferromagnetic specimen is broken up into a large number of domains and the directions of spontaneous magnetizations in domains are such that the magnetization averaged throughout the specimen is zero.

The origin of domains may be explained by considering the structures shown in Figure 13. In (a) the magnetic poles formed on the surface of the single domain crystal will create a magnetic energy $\frac{1}{8\pi}\int H^2 dr$. The magnetic energy for a square cross will be of order $M_s^2 \simeq 10^5$ ergs/cm^3. Here M_s denotes the saturation magnetization.

In (b) the magnetic energy has been reduced by a factor of roughly one-half as a result of dividing the crystal into two domains magnetized in opposite directions.[34] The subdivision process may be carried further as in (c): With N domains it turns out that the magnetic energy is reduced to approximately 1/N of the magnetic energy of the saturated configuration (a).

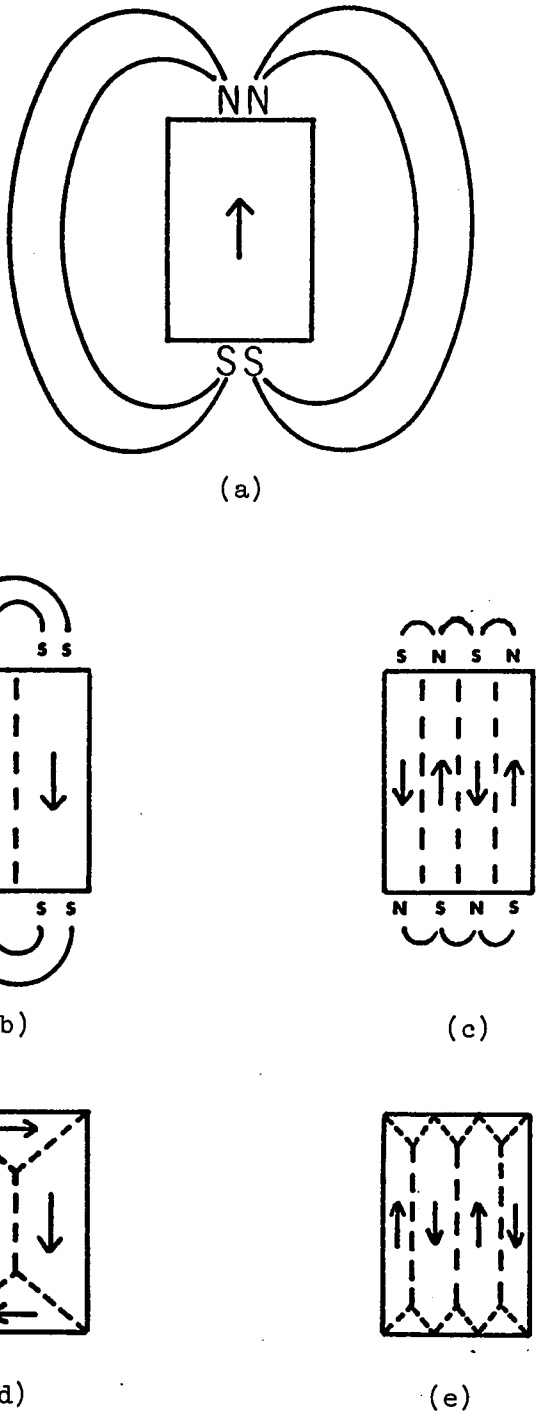

Fig. 13. The origin of domains

The subdivision process may be expected to continue until the energy required to establish an additional boundary layer or interface, separating two domains magnetized oppositely, is greater than the reduction in magnetic field energy consequent on the finer subdivision. It may be appreciated that a boundary layer does indeed have a certain amount of energy associated with it: on opposite sides of the boundary the magnetization is directed in anti-parallel directions; since the exchange forces favor parallel and oppose anti-parallel orientations of the magnetization, it will naturally require the expenditure of energy to establish a boundary layer.

It is possible to devise domain arrangements such as (d) for which the magnetic energy is zero. In (d) the boundaries of the triangular prism domains (termed "domains of closure") near the end faces of the crystal make equal angles (45°) with the magnetization in the rectangular domains and with the magnetization in the domains of closure. Therefore, the component of the magnetization normal to the boundary is continuous across the boundary, and no poles are formed anywhere in the crystal. As there are no poles there is no magnetic field associated with the magnetization. Therefore, as far as the magnetic energy is concerned, the closure domain of (d) is not different from that of (e). However, the experimentally observed patterns of domain structure of Fe single crystals show the patterns of (e). As was discussed in the previous section, the unit cells of Fe are longer along the magnetization direction. This means that the triangular prism domains in the configurations (d) and (e) are compressed to minimize lattice mismatch. Since the compressed volume is smaller in the configuration (e), the elastic energy is lower and this configuration is favored.

The domain structure in Fe is much simpler than that of Ni because the easy magnetization directions of Fe are the crystal axes. Even in the case of Fe, if the physical boundary of a specimen is not exactly perpendicular to one of the crystal axes the formation of closure domain is not possible at the surface. Figure 14 (a) shows the so-called "free patterns" on the surface of a Fe single crystal which is slightly tilted from the (100) plane. The domain structure inside a crystal is believed to be as simple as the configuration (e) in Figure 13 (3) and it is shown in Figure 14 (b).

As was mentioned before, there is an energy associated with the domain boundary wall which separates two oppositely oriented domains. This transition layer has a finite thickness and the motion of this layer in response to the external field is important in the magnetization process. The transition layer, called the Bloch wall, also moved by an external uniaxial stress and such a motion will be discussed in the following section.

Figure 15 shows the 180° Bloch wall which appears in the domain structure of Fe. The essential idea of the Bloch wall is that the entire change in spin direction between adjacent domains magnetized in opposite directions does not occur in one discontinuous jump across a single atomic plane. Rather, the change of direction will take place in a gradual way over many atomic planes. The reason for the gradual nature of the change is the fact that for a given total change of spin direction the exchange energy is lower when the change is distributed over many spins than when the change occurs abruptly.

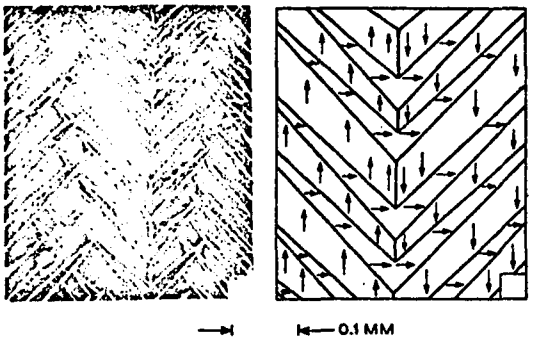

(a)

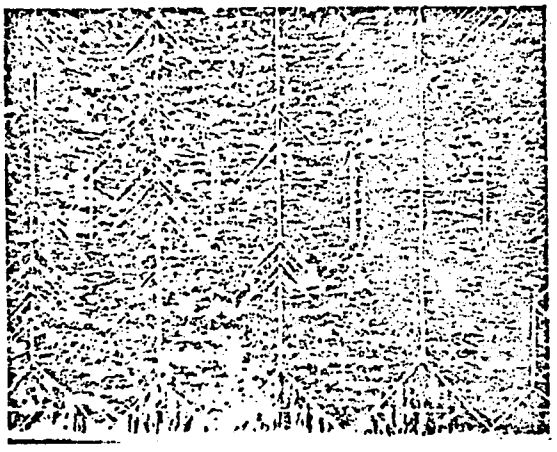

(b)

Fig. 14. Domain patterns of Fe-Si single crystal. (a) Typical tree patterns on the surface slightly tilted from the (100) plane (b) Closure pattern on the surface parallel to the (100) plane.

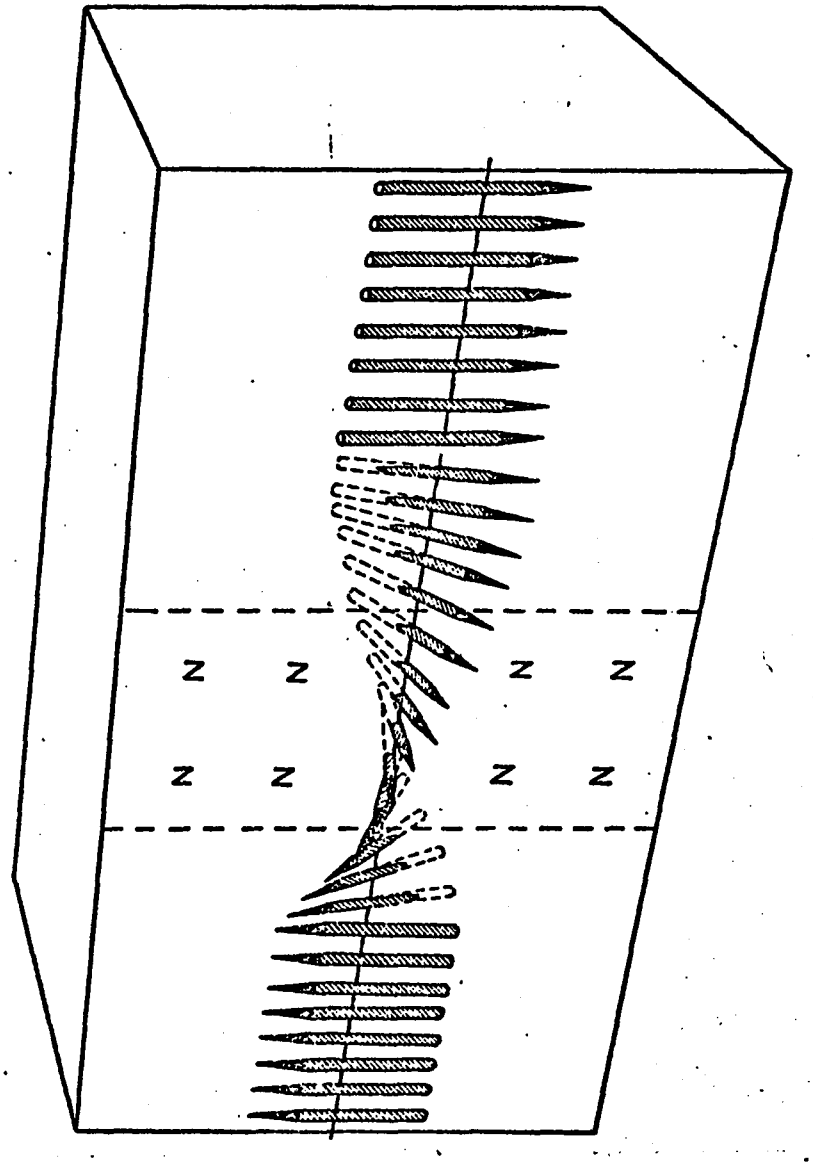

Fig. 15. 180° Bloch wall

From equation (3.12) the exchange energy between two spins making a small angle φ with each other can be written as

$$\omega_{ex} = J_e S^2 \varphi^2 \tag{3.29}$$

If the change occurs in N equal steps, then the angle change between neighboring spins in φ/N_p, and the exchange energy between each pair of neighboring atoms is

$$\omega'_{ex} = J_e S^2 (\varphi/N)^2$$

The total exchange energy of the line of N + 1 atoms is thus

$$W_{ex} = J_e S^2 \varphi^2 / N \tag{3.30}$$

The energy in equation (3.30) is certainly lower than that in equation (3.29). If $\varphi = \pi$, W_{ex} would be $2JeS^2$ from equation (3.10), while $W_{ex} = J_e S^2 \pi^2/N$ from equation (3.30).

Since the exchange energy of a domain wall is inversely proportional to the thickness, the wall might spread out until it filled a sizeable portion of the crystal, were it not for the restraining effect of the anisotropy energy, which acts to limit the width of the transition leyer. The spins contained within the wall are largely directed away from the axes of easy magnetization, so that there is a certain amount of anisotropy energy associated with the wall. The amount of anisotropy energy will be roughly proportional to the thickness of the wall, since the thickness is a measure of the total volume directed away from the axes of easy magnetization.

The actual thickness and the energy of the transition layer are the result of a balance between the competing claims of exchange energy and anisotropy energy, the former tending to increase the thickness and the latter tending to decrease the thickness.

The energy per unit surface area may be represented to a good approximation as the sum of contributions from exchange and anisotropy energies:

$$E_w = E_{ex} + E_{anis}$$

The exchange energy is given approximately by equation (3.30) for each line of atoms through the wall and normal to the plane of the wall. There are $1/a^2$ such lines per unit area, where a is the lattice constant. Hence

$$E_{ex} = \pi^2 J_e^2 S^2 / N a^2 \tag{3.31}$$

The anisotropy energy is of the order of the anisotropy constant times the volume, or

$$E_{anis} \simeq KNa \tag{3.32}$$

so that

$$E_w \simeq (\pi^2 J_e S^2 / N a^2) + KNa \tag{3.33}$$

which is minimum with respect to N when

$$\frac{\partial E_w}{\partial N} = 0 = -(\pi^2 J_e^2 S^2 / N^2 a^2) + Ka$$

or

$$N \simeq [\pi^2 J_e S^2 / K a^3]^{1/2} \tag{3.34}$$

The numerator in the bracket of equation (3.34) is the exchange energy between two neighboring but opposite spins. The magnitude of this exchange energy is the same as that between two parallel spins which is comparable to $k_B T_c$ where T_c is the Curie temperature. To an order of magnitude, in Fe,

$$N \simeq [k_B T_c / K a^3]^{1/2} \simeq [10^{-3}/10^5\, 10^{-23}]^{1/2}$$

$$\simeq 1000\, A^\circ$$

$$\simeq 300 \text{ lattice constants}$$

E. The Magnetization Process

A typical magnetization curve, showing the relation between B and H in a specimen initially unmagnetized, may be divided into three main parts. As is seen in Figure 16, the curve in the first region starts from the origin with a finite slope $dB/dH = \mu_0$. This portion of the curve is usually said to be reversible because the curve is retraced approximately (not exactly) when the external field if turned off.

The second part of the magnetization curve has the greatest slope and is irreversible. The path when H is decreased is quite different from the upward curve. In the third part the slope is very small and is reversible. When M_s is plotted against H, the slope will approach zero in this part (see Fig. 11).

In the unmagnetized state the directions in which the domains are saturated are either distributed at random or in some way such that the resultant magnetization as a whole is zero. Application of a magnetic field changes only the direction of magnetization in a given volume, not the magnitude.

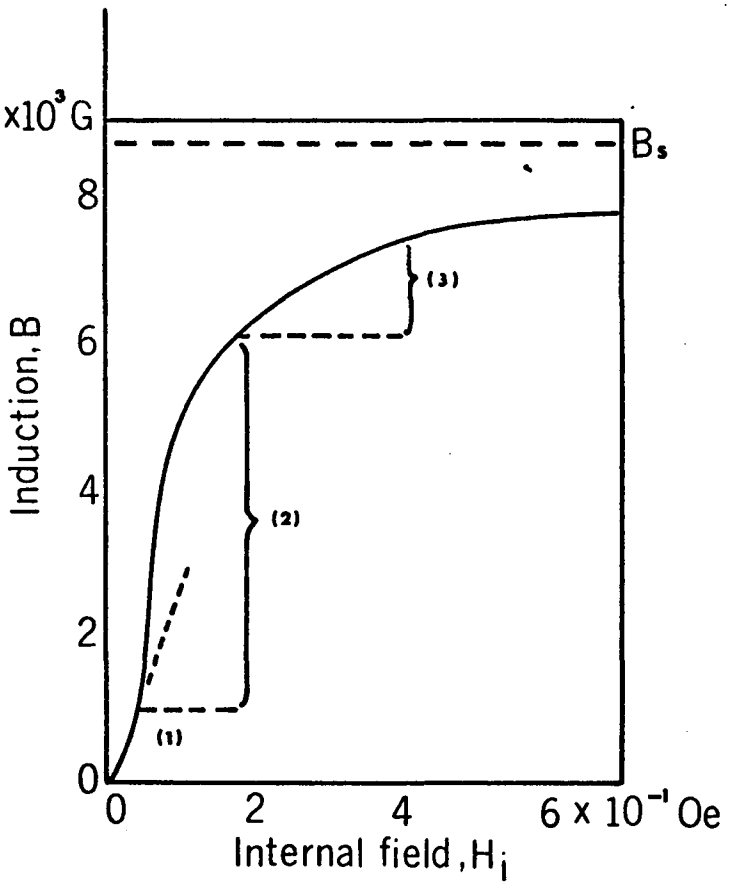

Fig. 16. Typical magnetization curve

The first part of the magnetization is known to be caused by the reversible domain boundary displacement. The gradual change in direction of spins in the Bloch wall (Fig. 15) makes the wall motion possible. Suppose that a field is applied along the upward spin direction. The spins oriented parallel to the field are in the lowest Zeeman energy state. In the Bloch wall the spin right next to the favored domain has a slightly higher Zeeman energy than the lowest state and tends to turn around along the field direction. This perturbs the balance between several different types of energy contributed to form the Bloch wall and the domain structure. Since the wall tends to keep the thickness constant, the small angle rotation of the first spin causes the same motion of the following spins. Therefore, the Bloch wall moves to expand the volume of the favored domain by turning the spin vectors one by one into the field direction like collapsing dominoes. If the field is not parallel to the favored domain direction, these spin vectors will turn around to point in the favored magnetization direction.

As domain boundary walls move to expand the volume of domains along a certain direction, the average magnetization is not zero any more. The non-zero value of the average magnetization creates a distribution of magnetic poles on the surface of the specimen such that the field due to these poles is opposite to the applied field. To keep the internal field constant the applied field must accordingly be increased.

However, a constant but very small internal field is not able to move the Bloch walls as far as they can go. The important restraining effects on Bloch wall propagation originated in lattice imperfections.

These include impurities and dislocations. In the case of Fe, a very pure sample usually contains various impurity concentrations less than $10 \sim 20$ PPM but the dislocation density might be about $10^6/cm^2$. Therefore, there will be at least 10,000 dislocation lines passing through a small domain of an unmagnetized specimen. As will be discussed later, Bloch walls interact with impurities and dislocations and such interactions cause effective potential barriers along the paths of the Bloch walls.

Figure 17(b) shows such an irregular shape potential hill that a Bloch wall encounters along its path.[30,34,36] If a 180° wall moves through a distance x, as shown in Figure 17 (a), then

$$E_H = 2HM_s x A$$

assuming that the total area of the wall is A. Thus, there is an effective pressure on the wall, given by

$$\frac{1}{A}\frac{\partial E_H}{\partial x} = 2HM_s \tag{3.35}$$

Figure 17 (c) shows the pressure on the Bloch wall from the potential hill that opposes the motion of the wall. Suppose that the magnitude of H is just enough to bring the wall to the point A. If the field is turned off at this point, the wall would return to its original position at 0. However, if the magnitude of H is slightly higher than that which is needed to bring the wall to A, the wall suddenly jumps from A to E. Turning off the magnetic field at this point causes the wall to move to point D. Since the potential is in its local minimum, the wall would stay there.

The first part of the magnetization curve represents the motion of Bloch walls between points 0 and A. Since each Bloch wall encounters

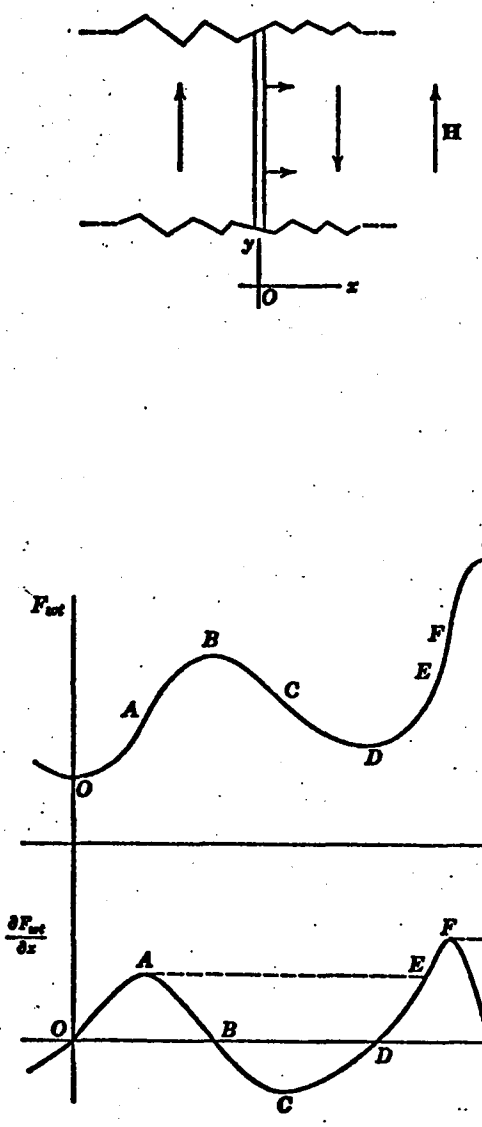

Fig. 17. Illustration of domain wall movement in soft materials possessing imperfections. (a) The direction of motion of a 180° wall under the action of a field H is indicated. (b) A possible form for the dependence of $F_{\omega t}$ on x. (c) The slope of $F_{\omega t}$ is plotted as a function of x.

a potential of different shape, the reversibility of wall motion throughout a whole specimen would not be exactly perfect. The irreversible domain wall motion in the second part of the magnetization curve has already been explained. The evidence of this wall jump is found in a detailed magnetization curve in the second part which shows small discontinuous steps. Such a jumping motion was first seen by Bahkhausen and the effect was named after him.

When the applied field is removed after saturation is reached, Bloch walls move back along the paths to restore the original unmagnetized state. This returning motion of each Bloch wall ends at the position corresponding to the point D in its path. As a result, the unmagnetized state is not obtained and the specimen is partially magnetized. Such a partial magnetization is called the remanence, as seen in Figure 18. To recover the unmagnetized state, it is necessary to apply a field which is in the direction opposite to that of the previously applied field. This field enables the Bloch wall to move back from D to the original point O. The magnitude of this inverse field needed to restore the unmagnetized state of a specimen is called the coercive force.

From the discussion given above, it is clear why the first part of the magnetization curve is reversible while it is irreversible in the second part. The magnetization at the beginning of the first part can be related to the applied field by a constant which is called the initial permeability. The initial permeability is a measure of the intrinsic restoring force on the wall for a small displacement, while the coercive force is a measure of the maximum restoring force on the wall. The

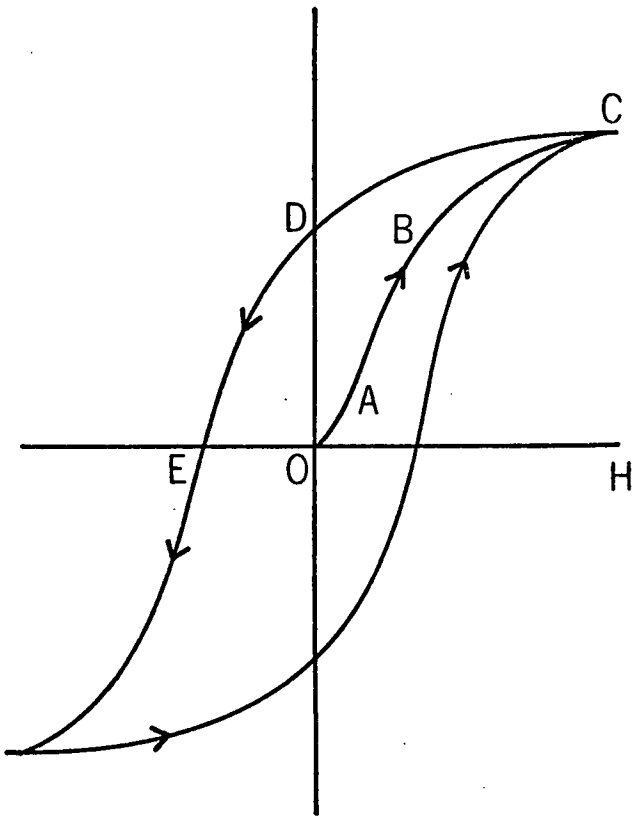

Fig. 18. Typical hysteresis loop of ferromagnetic substances showing remanence at D and coercive force Hc at E.

coercive force tells us the field strength needed to carry a wall from one potential energy valley to another, past the highest intervening energy hump.

Since the irregularly shaped potential that each wall encounters is produced by lattice imperfections, the initial permeability and coercive force are sensitive to the mechanical structure of a specimen. Thus it has been experimentally observed that metallurgical treatment and change of chemical composition significantly affect the values of these quantities.[37]

F. Motion of Bloch Walls by External Stress

Any arbitrary external stress can change the domain structure of a specimen provided the external stress is not hydrostatic. The effect on the domain by a complex stress can always be explained on the basis of the effect by a uniaxial stress. It is seen in equation (3.28) that an external stress explicitly contributes to the energy of a crystal and the contribution is dependent on the signs of K, λ_{100}, λ_{111} and σ. Since the interaction between the magnetization and the stress depends on the angle between them, domain rearrangement always proceeds to reach the proper energy state of the crystal. The fundamental difference in the wall movement by the magnetic field and the uniaxial stress must be: the external field takes only one direction of magnetization, while due to its bilateral nature the uniaxial stress equally favors both directions of magnetization, which are opposite to each other along certain axes in the crystal. The movements of domain walls by an external magnetic field and uniaxial stress are shown in Figure 19.

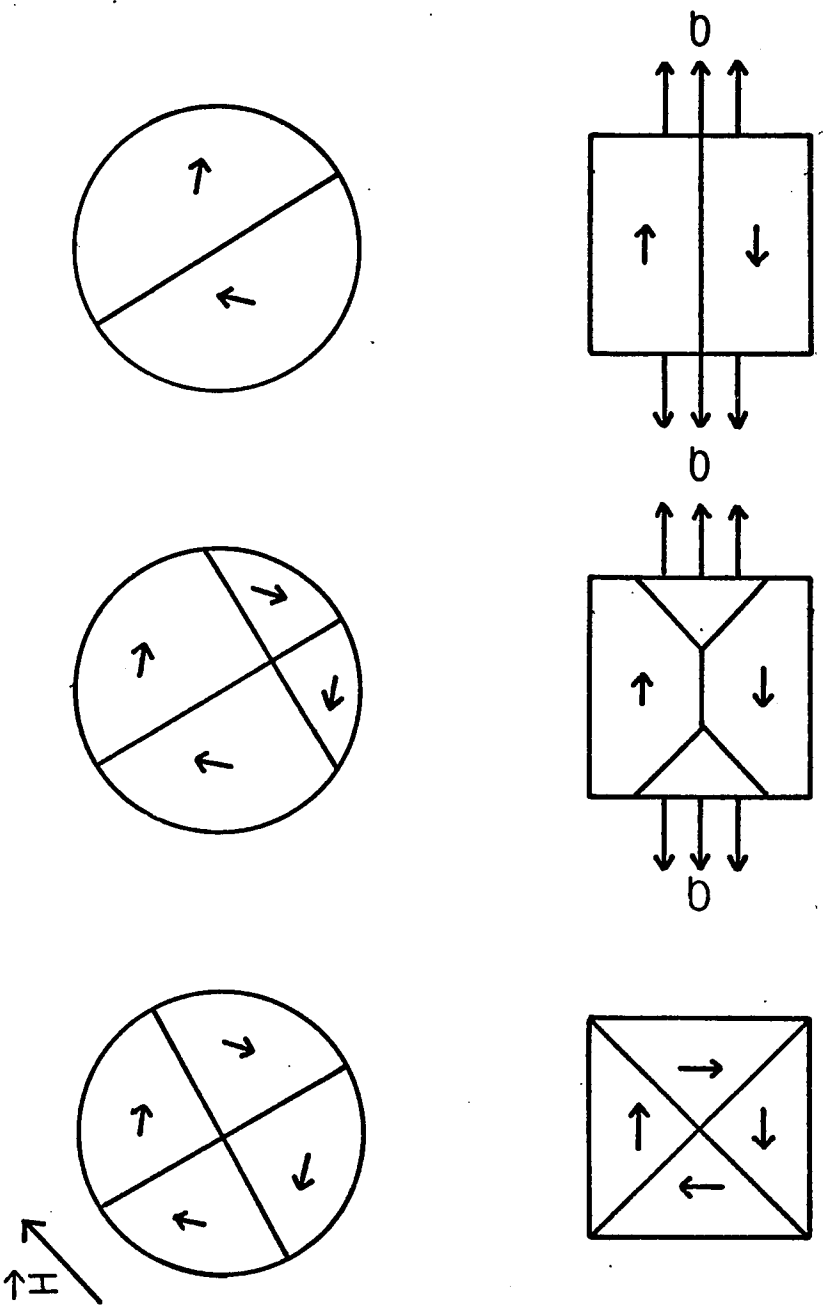

Fig. 19. Comparison between domain wall movements induced (a) by external magnetizing field (b) by external tensile stress for $\lambda > 0$.

Either a magnetizing field or an external stress is thermodynamically equivalent to a hydrostatic pressure within each domain, acting on its domain walls. This is because the unit of $f_{k,me}$ is energy per unit volume which is equivalent to pressure. The basic idea is that when a wall divides two regions with different energy density it tends to move to reduce the total energy of the crystal by expanding the volume of the domain with the lower energy density. This is to say that the wall moves by virtue of net pressure acting on it and this pressure is the difference between the energy densities in the domains divided by the wall.

Before the motion of a Bloch wall is considered it may be useful to inspect equation (3.28). Suppose two domains in Fe, say y and z domains, are subjected to an external uniaxial stress applied along the z-axis. From equation (3.28), which is rewritten below,

$$f_{k,me} = K_1(\alpha_1^2\alpha_2^2 + \alpha_2^2\alpha_3^2 + \alpha_3^2\alpha_1^2) - \frac{3}{2}\lambda_{100}\sigma(\alpha_1^2\gamma_1^2 + \alpha_2^2\gamma_2^2 + \alpha_3^2\gamma_3^2) - 3\lambda_{111}\sigma(\alpha_1\alpha_2\gamma_1\gamma_2 + \alpha_2\alpha_3\gamma_2\gamma_3 + \alpha_3\alpha_1\gamma_3\gamma_1) \tag{3.28}$$

we can write the energy density in each domain at the moment when the stress is applied. For the z-domain, it is

$$f_z = -\frac{3}{2}\lambda_{100}\sigma$$

while $f_y = 0$. If the stress is tensile the sign of σ is positive, and since $\lambda_{100} = +21 \times 10^{-6}$, the total energy will be lower in the domains oriented in the $\pm$ z-directions. If the stress is compressional f_x will be positive and is higher than f_y. Suppose that the magnetization vector originally pointing along the y-axis is rotated toward the z-axis in the y-z plane. The angle dependence of $f_{me,k}$ is immediately written as

$$f_{K,me} = K_1 \cos^2\theta \sin^2\theta - \frac{3}{2}\lambda_{100}\sigma\cos^2\theta \qquad (3.36)$$

where θ is the angle between the magnetization vector and the z-axis. Taking $\partial f_{me,k}/\partial\theta = 0$, we get

$$\theta_c = \sin^{-1}\left[\frac{1}{2} - \frac{3}{4K_1}\lambda_{100}\sigma\right]^{\frac{1}{2}} \qquad (3.37)$$

where θ_c is the direction of magnetization for the maximum $f_{me,k}$ at a fixed value of σ. $f_{me,k}$ is plotted in Figure 20 as a function of θ for $\sigma > 0$. If $|\theta_c| > 0$ the magnetization vector oriented along the y-axis, $\theta = 0$, cannot immediately turn around toward z because $f_{me,k}(0)$ is at the local minimum. A sudden turning motion of the magnetization vector will only happen when θ_c becomes zero in the classical picture. Substituting the values of k_1 and λ_{100}, the magnitude of tensile stress to make $\theta_c = 0$ will be

$$\sigma_c = \frac{3}{2}\frac{K_1}{\lambda_{100}}$$
$$= \frac{2}{3} \times 4.8 \times 10^5 / 21 \times 10^{-6}$$
$$\cong 1.524 \times 10^{10}\ \text{erg/cm}^3\ (= \text{dyne/cm}^2)$$
$$= 1.524 \times 10^4\ \text{bar}$$

which is about 30 times larger than the yield strength of an Fe single crystal at room temperature. The rotational motion of a spin from the z-axis to y-axis requires a compressional stress of the same magnitude applied along the z-axis.

Since rotational motion of the magnetization is not possible by an external stress, we now turn our attention to the motion of Bloch

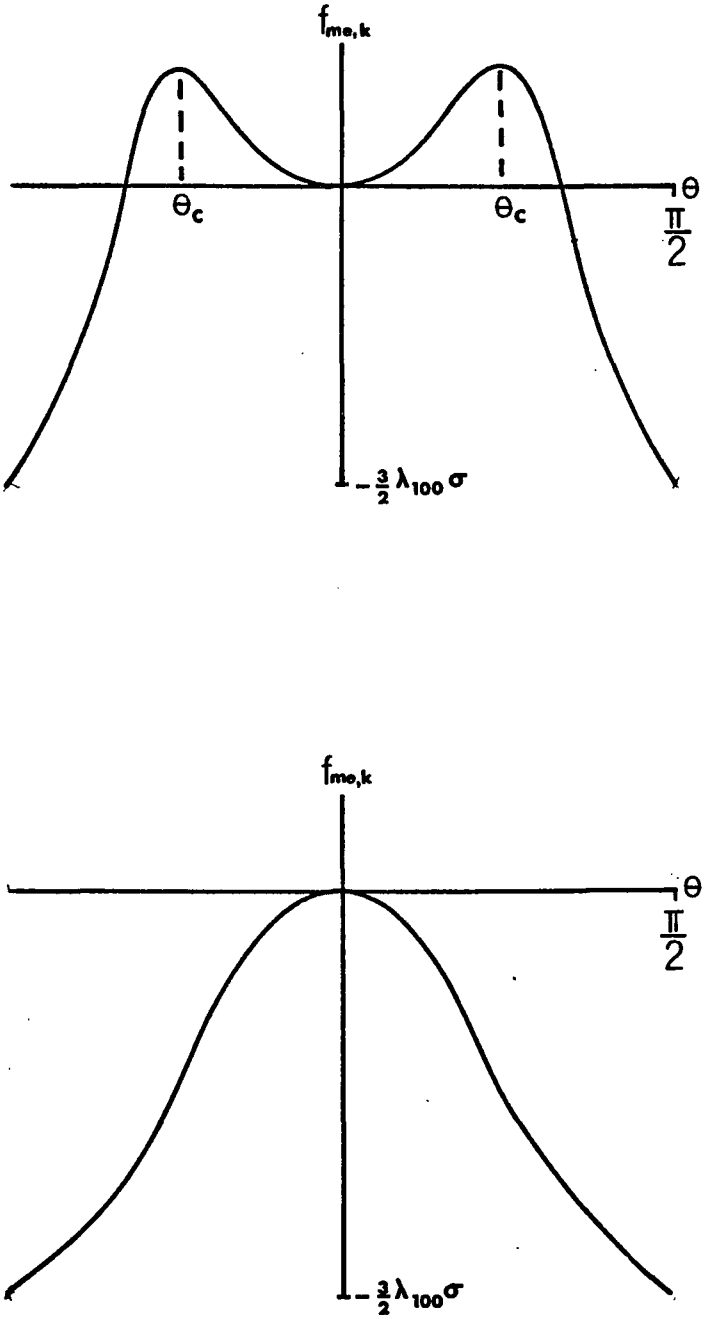

Fig. 20. Angular dependence of $f_{me,k}$, where θ is the angle between the magnetization and the stress axis.

walls in Fe. The translational motion of Bloch walls activated by an external stress will be resisted by the irregularly shaped potential hills as discussed in the previous section. To complete their motion, that is to expand the volume of favored domains as far as possible, the Bloch walls must pass over the highest potential humps they meet. The average pressure on the walls must be the same as that which is needed to bring the sample from its partial magnetization at remanence (Fig. 18) to the unmagnetized state. Then the Bloch walls can move beyond the highest hills. This pressure is estimated to be $\sim M_s H_c$, where M_s is the spontaneous magnetization and H_c is the coercive force. The value of M_s in Fe at room temperature is 1740 Gauss and H_c is about 1 Gauss.

The net pressure on a 90° Bloch wall can be written in a simple form:

$$|P_{90^\circ}| = \frac{3}{2} \lambda_{100} |\gamma_i^2 - \gamma_j^2| |\sigma| \qquad (3.38)$$

Further, it can easily be seen that the net pressure on a 180° Bloch wall is always zero regardless of the orientation of the axes along which the uniaxial stress is applied.

The magnitude of the critical stress applied along a crystal axis of Fe to complete the domain wall motion is thus estimated to be

$$\frac{3}{2} \lambda_{100} \sigma \simeq 1740 \ dyne/cm^2$$

so,

$$\sigma = \frac{2}{3} \frac{1740}{21 \times 10^{-6}} \simeq 55 \times 10^6 \ dyne/cm^2 = 55 \ bar$$

This critical stress for domain wall motion is about one tenth of the yield strength of an Fe single crystal, which is about 530 bar.

In the case of Ni, the easy magnetization directions are along the eight equivalent $\langle 111 \rangle$ orientations. Therefore, a description of the motion of Bloch walls is very complicated. However, the value of K_1 in Ni is 5×10^4 erg/cm^3, which is smaller than that of Fe by an order of magnitude so that rotational motion of the magnetization vector is possible. By a calculation similar to equation (3.37) the critical stress for domain rotation is estimated to be about 240 bar when the stress is along one of the crystal axes. The basic difference in Ni is that the favored orientations of the magnetization are perpendicular to the stress axis if it is tensile, which is opposite to the case of Fe.

IV. POINT DEFECTS AND ELASTIC DIPOLES

An impurity introduced in the lattice of a crystal creates a local distortion. Such a distortion is either isotropic or anisotropic depending upon the symmetry at the position of the impurity in the host lattice. It will be shown that the local distortion due to an impurity at an interstitial site of a BCC crystal is anisotropic. This local distortion can be related to the "elastic dipole" concept.[38] This approach has been developed in analogy with the classical electric dipole.

An immediate consequence of such an interaction to this uniaxial stress μ^+SR experiment is that the stress tends to align the elastic dipole associated with a muon along a certain direction. The principal axis of the elastic dipole at an interstitial site of a BCC crystal is determined by the orientation of the tetragonal axes passing the site (section A). The dipolar fields at each interstitial site in Fe are also determined by the orientation of the tetragonal axis (Appendix C) of the site. Therefore the site occupation probability of a hopping muon will be different for sites with differently oriented tetragonal axes and this will cause a drastic change in the field acting on the muon.

The first part of this chapter is a discussion of the symmetry associated with a point defect in a crystal. The second gives the basic idea of the simplest case of the "stress-induced point defect relaxation" summarized from reference 38.

A. Crystal and Defect Symmetry

The symmetry of a perfect crystal is most fully defined by its space group, which is the collection of symmetry operations that take the atomic arrangement into an identical (indistinguishable) one. For the present purpose, we are interested only in the rotational type of symmetry operations, not in translations. The reason for this choice is that the applied stress is always taken to be uniform, so that the type of site is important only as far as the response to stress is concerned.

Consider a crystal which contains just one point defect. This defect may be as simple as an extra or missing atom, as complex as a cluster of several foreign or diaplaced atoms extending over several lattice sites. The presence of a defect destroys the translational symmetry of the crystal, and the resultant crystal may be thought of as a large molecule. For brevity, the point-group symmetry of this defective crystal is called the defect symmetry. The defect symmetry may be lower than or equal to that of the perfect crystal.

We consider two types of point defects. There is the elementary point defect, which consists of either a single substitute atom, a vacancy, or an interstitial atom. The second type of point defect is a composite one more complex than those belonging to the first type. Since a muon in a crystal should belong to the first type of point defect, we will only examine this type.

In the case of the first type, it is easy to see that the defect symmetry is simply the site symmetry. This is valid unless the surrounding lattice atoms relax to cause a further lowering of the symmetry. But in most cases the relaxation occurs with no change in symmetry

of the defect, since it takes place in a manner which is symmetrical both with respect to the atoms comprising the defect, and to the site about which they are situated. The term site symmetry denotes the point symmetry of the perfect crystal at which the defect is created.

The defect symmetry of the first type is illustrated in Figure 21. Site a, at a cube corner, has full cubic symmetry (see Reference 40 for notations), O_h, while site c, at a face center has full tetragonal symmetry D_{4h} with the tetragonal axis perpendicular to the page. Side d, on the edge center, also has D_{4h} symmetry, but now the tetragonal axis is parallel to the y axis. Such a symmetry consideration on the two-dimensional lattice can easily be extended to a three-dimensional BCC or FCC lattice. Figure 22 shows the symmetry at interstitial sites in a BCC lattice.

B. Elastic Dipoles

The insertion of a point defect into a crystal produces a local elastic distortion. As a result, there will be an interaction between the defect and an external stress (not hydrostatic) applied to the crystal. In some way this interaction is analogous to the interaction of an electric dipole with an applied electric field. Accordingly, a defect which produces local distortion has been called an elastic dipole. A major difference is that, whereas an electric dipole moment is characterized by a vector quantity which determines its interaction with the (vector) electric field, an elastic dipole is characterized by a second-rank tensor since it interacts with a stress field.

Suppose an electric dipole in a crystal is defined by a dipole moment, μ , and by its orientation relative to the crystal axes. In

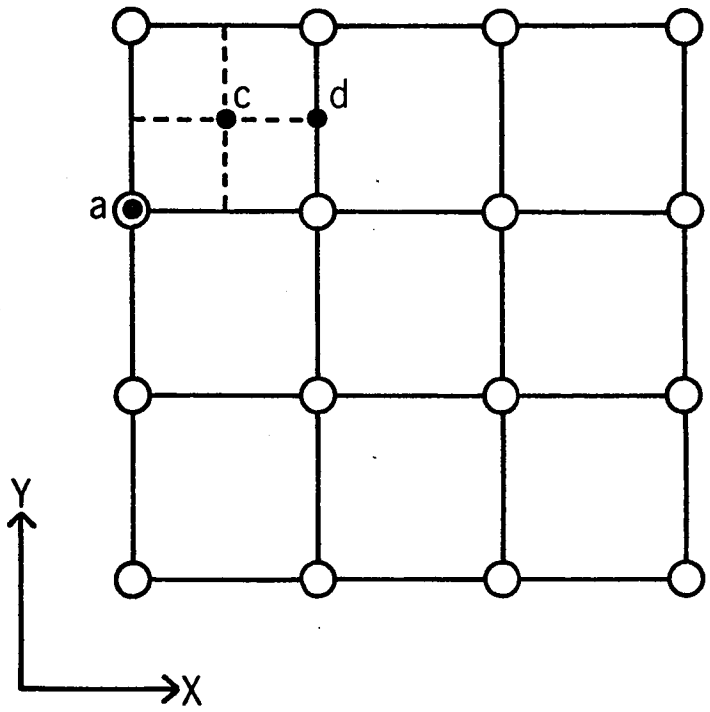

Fig. 21. Illustration of defect symmetry in a two dimensional square lattice.

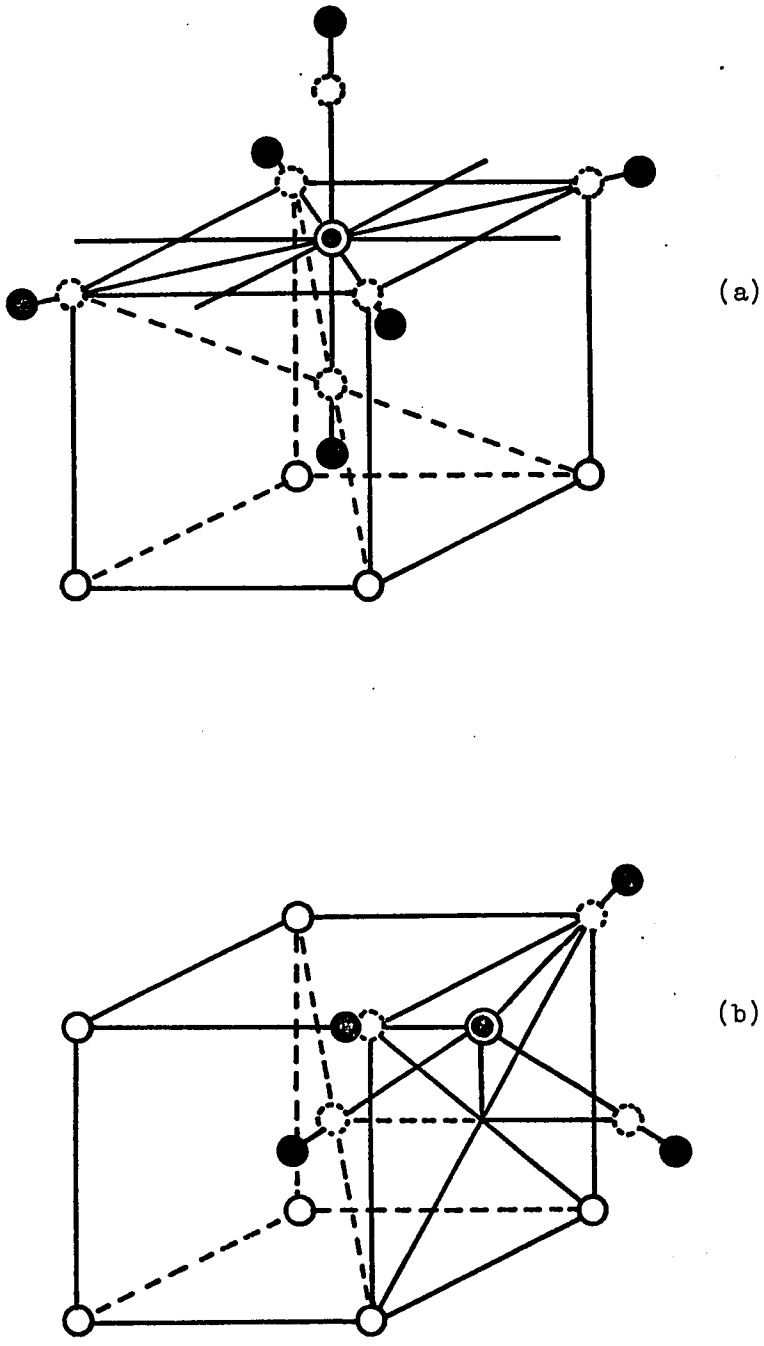

Fig. 22. A BCC unit cell containing a point defect at (a) octahedral site (b) tetrahedral site. Possible displacements of neighboring atoms are also indicated.

general there will be several, say n, crystallographically equivalent orientations which the dipole may assume in the lattice. The magnitude of μ of the dipole moment is independent of its orientation, but its particular direction relative to a set of axes fixed in the crystal does require specification. Accordingly, the dipole is denoted by the vector $\vec{\mu}^{(P)}$. The energy of interaction of such a dipole with an electric field is given by

$$U_P = \sum_i \mu_i^{(P)} E_i \tag{4.1}$$

In the absence of the electric field, the energy of the dipole in any one of the n crystallographic equivalent directions is the same. Equation (4.1) shows, however, that the presence of the field serves to split the energies of the various crystallographic orientations so that, in general, they are no longer equal.

Consider U_p in equation (4.1) as the energy per unit volume per unit concentration of dipoles all aligned in the Pth direction. The quantity $\mu_i^{(P)}$ is then regarded as the dipole moment per unit volume per unit concentration. In terms of these definitions, equation (4.1) leads readily to the analoguous expressions for the elastic dipole. If a number of defects are all aligned in the same orientation in a stress field, the energy of the interaction with the stress field, U_p, per unit volume per unit concentration is given by:

$$U_P = -\sum_{i,j} v_{ij}^{(P)} \sigma_{ij} \equiv -v_o \sum_{i,j} \lambda_{ij}^{(P)} \sigma_{ij} \tag{4.2}$$

Since v_{ij} has the unit of volume, it is convenient to introduce the dimensionless parameters λ_{ij}, as in equation (4.2), by factoring out the

atomic (or molecular) volume $\mathcal{V}_0$. The quantities $\mathcal{V}_{ij}^{(p)}$ are components of pure (not involving a rotation) strain exhibited by the crystal when a unit concentration of defects is introduced into the crystal, all aligned in the Pth orientation. Thus:

$$\mathcal{V}_{ij}^{(p)} = \left(\partial \epsilon_{ij} / \partial n_p\right) \quad ; \quad \lambda_{ij}^{(p)} = \left(\partial \epsilon_{ij} / \partial c_p\right) \tag{4.3}$$

where ϵ_{ij} are the strain components, n_p is the number of defects per unit volume in orientation p, and $c_p = n_p \mathcal{V}_0$ is the mole fraction of defects in orientation p.

Since the $\lambda_{ij}^{(p)}$ are components of pure strain, they constitute a symmetry tensor (see Reference 41). The tensor $\lambda_{ij}^{(p)}$, (for brevity it is called the "λ-tensor"), can be transformed to take a diagonal form:

$$\overleftrightarrow{\lambda} = \begin{pmatrix} \lambda_1 & 0 & 0 \\ 0 & \lambda_2 & 0 \\ 0 & 0 & \lambda_3 \end{pmatrix} \tag{4.4}$$

The quantities λ_1, λ_2 and λ_3 are called the "principal values" of the λ-tensor, and may be represented by a strain ellipsoid, as shown in Figure 23. Since all defect orientations, p = 1, 2, ... n, are crystallographically equivalent, it follows that each tensor $\lambda_{ij}^{(p)}$ must have the same set of principal values. Thus three values λ_1, λ_2 and λ_3 are independent of p. However, it must be noted that the λ-tensor is not the only method for characterizing the behavior of a defect in the presence of stress.

Kanzaki[39] has introduced the following very useful concept for a theoretical description of the strain field around the point defect in a

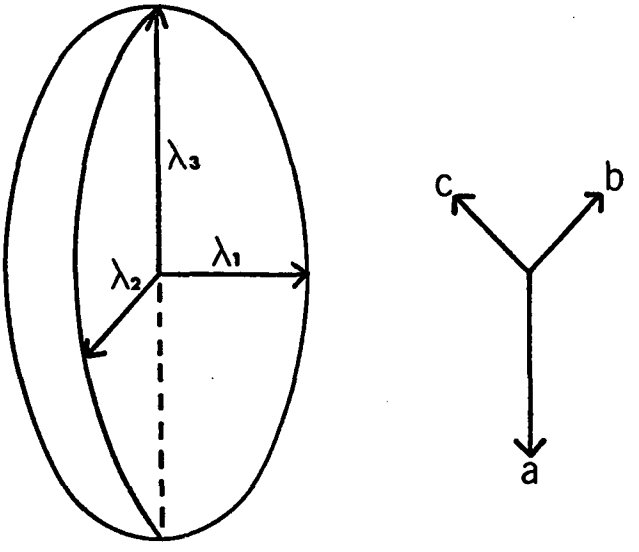

Fig. 23. Three principal values of a λ-tensor represented by a strain ellipsoid. These principal axes can have any orientation relative to the crystal axes a, b, c.

crystal. The actual displacements of the lattice atoms by the defect can be stimulated in a defect-free lattice by applying virtual forces f_j^m (called the Kanzaki force) to each lattice atom m (with its position $\vec{r}^{(m)}$ from the defect site). The force distribution can be described by a multipole expansion in analogy to a charge distribution in the electrostatic case. It turns out that for most cases it suffices to take only the "dipole part" of the force distribution

$$P_{ij} = \sum_m f_j^m x_j^m \tag{4.5}$$

the double-force tensor. Furthermore, only forces on a few atoms (for example, only up to the next nearest atoms of the defect) are necessary to give a good description of the displacements.

To be consistent with notation conventions used in the elastic dipole, the double force tensor will be written as $P_{ij}^{(p)}$ to specify the orientation of the defect generating the tensor. Since the $P_{ij}^{(p)}$ are defined as a negative stress to maintain constant strain per unit concentration defects introduced into the orientation p,

$$P_{ij}^{(p)} = -\partial\sigma_{ij}/\partial n_p = -v_o(\partial\sigma_{ij}/\partial\epsilon_p) \tag{4.6}$$

By equations (4.3), (4.6) and the stress-strain relation, we get

$$P_{ij}^{(p)} = v_o \sum_{k,\ell} C_{ijk\ell}\lambda_{k\ell}^{(p)} \tag{4.7}$$

or

$$\lambda_{ij}^{(p)} = v_o^{-1} \sum_{k,\ell} S_{ijk\ell} P_{k\ell}^{(p)} \tag{4.8}$$

$C_{ijk\ell}$ and $S_{ijk\ell}$ are the elastic stiffness and compliance tensor components, respectively. The change in volume of the crystal by defects can be written in terms of the parameters defined previously:

$$\Delta V/V = \sum_i \epsilon_{ii} = C_0 \, \mathrm{Tr}\, \lambda_{ij} = \frac{C_0}{3v_0} K \, \mathrm{Tr}\, P_{ij} \tag{4.9}$$

where

$$C_0 = \sum_p C_p$$
$$K = 3(S_{11} + 2S_{12}) = 3/(C_{11} + 2C_{12}) \tag{4.10}$$

and K is the compressibility of the crystal. Since the λ -tensor is independent of p, the superscript p is not used in equation (4.9). The quantities $\Delta V/V$ and C_0 can be measured. Thus Tr λ_{ij} is obtained.

C. Thermodynamics of the Relaxation of Elastic Dipoles Under Uniaxial Stress

Suppose there are m equivalent defect orientations in a crystal. Upon the application of an external stress, the degeneracy of the free energy level of elastic dipoles will be removed. Such a split in the energy level causes dipoles along a certain orientation to be energetically favored by the stress. To reduce the total interaction between elastic dipoles and the external stress, the reorientation of less favored dipoles should take place. This reorientation of elastic dipoles can be accomplished by the migration of point defects from their original sites to others. Such a process is called the "stress induced ordering" and this process continues until the equilibrium distribution of elastic dipoles is reached.

It is most convenient to describe the state or order in the crystal by the parameter η_p which is defined as

$$\eta_p = C_p - (C_0/m) \qquad (p = 1, 2, \cdots, m) \tag{4.11}$$

If C_0 is conserved

$$\sum_{p=1}^{m} \eta_p = 0 \ .$$

For simplicity, assume that there are only two possible orientations which are equivalent in the absence of stress. Therefore, m = 2. Further simplification is made by assuming that the stress is applied along a principal axis of one of the dipolar orientations. The tensile strain can be written:

$$\epsilon = J_u \sigma + \sum_{p=1}^{2} \lambda^{(p)} \eta_p + L(T - T_{ref}) \qquad (4.12)$$

The constant J_u represents the ordinary instantaneous compliance (see Reference 38) and the last term takes into account the thermal expansion of the specimen. Since m = 2, equation (4.12) can be rewritten as

$$\epsilon = J_u \sigma + (\delta\lambda)\eta_1 + L(T - T_{ref}) \qquad (4.13)$$

where $\delta\lambda \equiv \lambda^{(1)} - \lambda^{(2)}$.

For a given temperature T and the state of stress, the equilibrium value of the order parameter η_1 is completely determined. Thus, a thermodynamical Gibbs type free energy function may be written as a function of T and σ only. On the other hand, the change in η_1 is not instantaneous, but it is rather controlled by atom movements governed by an Arrhenius-type equation. Consequently, it is possible by some treatment (for example, application of external stress, followed by lowering the temperature) to hold the order variable, η_1, at given value while measuring the conventional thermodynamic properties of the system. It is

possible to define a pseudo free energy function in which σ , T and η_1 , are taken as independent variables. If this function G(σ , C, T) is expanded about $\sigma = 0$, C = 0 it must take the form

$$G(\sigma, C, T) = G(0,0,T) + \tfrac{1}{2} a\sigma^2 + b\sigma\eta_1 + \tfrac{1}{2} c\eta_1^2 + d\sigma \tag{4.14}$$

for small values of σ and η_1, where G(0, 0, T), a, b, c and d are in general, functions of temperature and C_0. The absence of a term η_1, alone follows from the fact that for $\sigma = 0$, η_1 must be zero.

Recognizing that the G function is a generalized Gibbs free energy, we note that its differential form must be

$$dG = -V_0 \epsilon \, d\sigma - S dT - A d\eta_1 \tag{4.15}$$

where V_0 is the molar volume of the crystal at T_{ref}, S is the entropy and A is a thermodynamic variable conjugate to η_1 which is often called the "affinity". In thermodynamic equilibrium at constant σ and T, the requirement that G must be a minimum, means that A = 0. Under non-equilibrium conditions A may be taken as a measure of the driving force toward equilibrium. Comparison of equation (4.14) and (4.15) shows

$$\epsilon = -\frac{1}{V_0} \frac{\partial G}{\partial \sigma} = -\frac{1}{V_0} (a\sigma + b\eta_1 + d) \tag{4.16}$$

Finally, comparison of the above equation with equation (4.13) gives

$$a = -V_0 J_u \, , \quad b = -V_0 (\delta\lambda) \, , \quad d = -V_0 L(T - T_{ref}) \tag{4.17}$$

Now, we define a quantity Δg as the difference in the free energy when a specific dipole is converted from an orientation of type 2 to one of type 1. It is given by

$$\Delta g \equiv \frac{\partial G'}{\partial N_1} = \frac{1}{N_A}\frac{\partial G'}{\partial \eta_1} = -v_o(\delta\lambda)\sigma + \frac{1}{N_A} c\eta_1 \qquad (4.18)$$

where

$G' = G - (-TS_{cf})$

N_A = Avogadro's number.

The quantity S_{cf}, the configurational entropy, arises from the configurational degeneracy which is not present in an Einstein crystal. However, in a crystal with defects the sites are equivalent but distinguishable. In the ideal lattice gas theory, the contributions to the entropy can be written as a sum of two terms. The first term comes from the number of ways the A distinguishable atoms can be distributed among B labeled sites, which is given by

$$\frac{B!}{A!(B-A)!} \quad .$$

The second term comes from the pure vibrational motion of defect atoms in a potential well supplied by the host lattice. Since we may not want to include the contribution from Scf, its contributions to G and c were subtracted in equation (4.19). Equation (4.18) states that the free energy difference between a dipole in an orientation of type 1 and type 2 depends, in general, on both the stress and the state of order. The dependence on stress is just the splitting of the free energy levels of the two crystallographically equivalent orientations by the application of stress, which provides the basis for the redistribution among sites, and therefore, for the existence of a relaxation process. The last term of equation (4.18) is somewhat less obvious. If c is not zero, it means

that the existence of a state of order will, in itself, result in a splitting of states. Such a term was first proposed by Zener, represents an interaction among the dipoles, and is therefore referred to as an "interaction term".

In the μ^+SR experiment with an external uniaxial stress the interaction term explained above is completely negligible since an infinite dilution of the point defect is always possible. Hence in this work we use the simpler form of equation (4.18) which is written as

$$\Delta q = - v_o (\delta\lambda) \sigma \tag{4.20}$$

The physical meaning of equation (4.20) is illustrated in Figure 24.

Equation (4.20) can be rewritten in a more convenient form:

$$\Delta q = -(S_{11} - S_{12}) (P_1 - P_2) \sigma \tag{4.21}$$

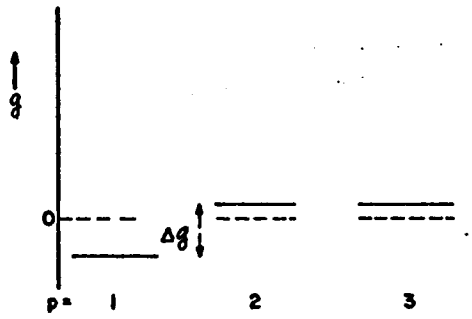

Fig. 24(a). Schematic illustration of the splitting of the free energy levels by stress for a set of three equivalent dipoles. Dashed lines: before application of stress; solid lines: after stress applied.

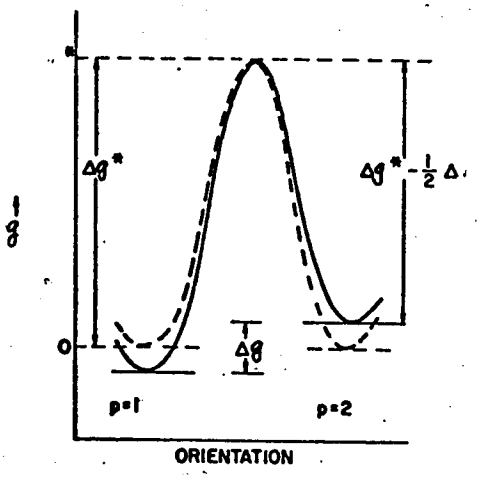

Fig. 24(b). Illustrating the activation barriers before (dashed lines) and after (solid lines) the splitting of free-energy levels by stress. Δg^* is the activation energy before the application of external stress.

V. RESULTS AND DISCUSSION

A. Results on Fe <100> Sample

The presentation of results on this sample is essentially divided into four steps:

1. application of uniaxial stress without an external magnetic field
2. application of an external magnetic field without the uniaxial stress
3. application of uniaxial stress with a fixed external field
4. repetition of step 1.

To check the reversibility, an additional measurement was always performed following every measurement with an external uniaxial stress.

a. Step 1

Figure 25 shows the change in frequency as a function of the tensile strain induced along the long axis of the sample. As indicated in the figure, two measurements were performed before the sample was put in the stress rig ("in air" measurements). The frequency on one face is 48.413 MHz and on the other face is 48.507 MHz. This difference in frequency is assumed to be caused by a slight surface tension which was not removed after the crystal was grown.

After this sample was placed in the puller by the process described in Chapter II the frequency of the first face dropped down to 48.308 MHz. Even though metal crystals are known to be very difficult to handle without mechanically disturbing them (Cottrel, 1952, p 101)[3], such

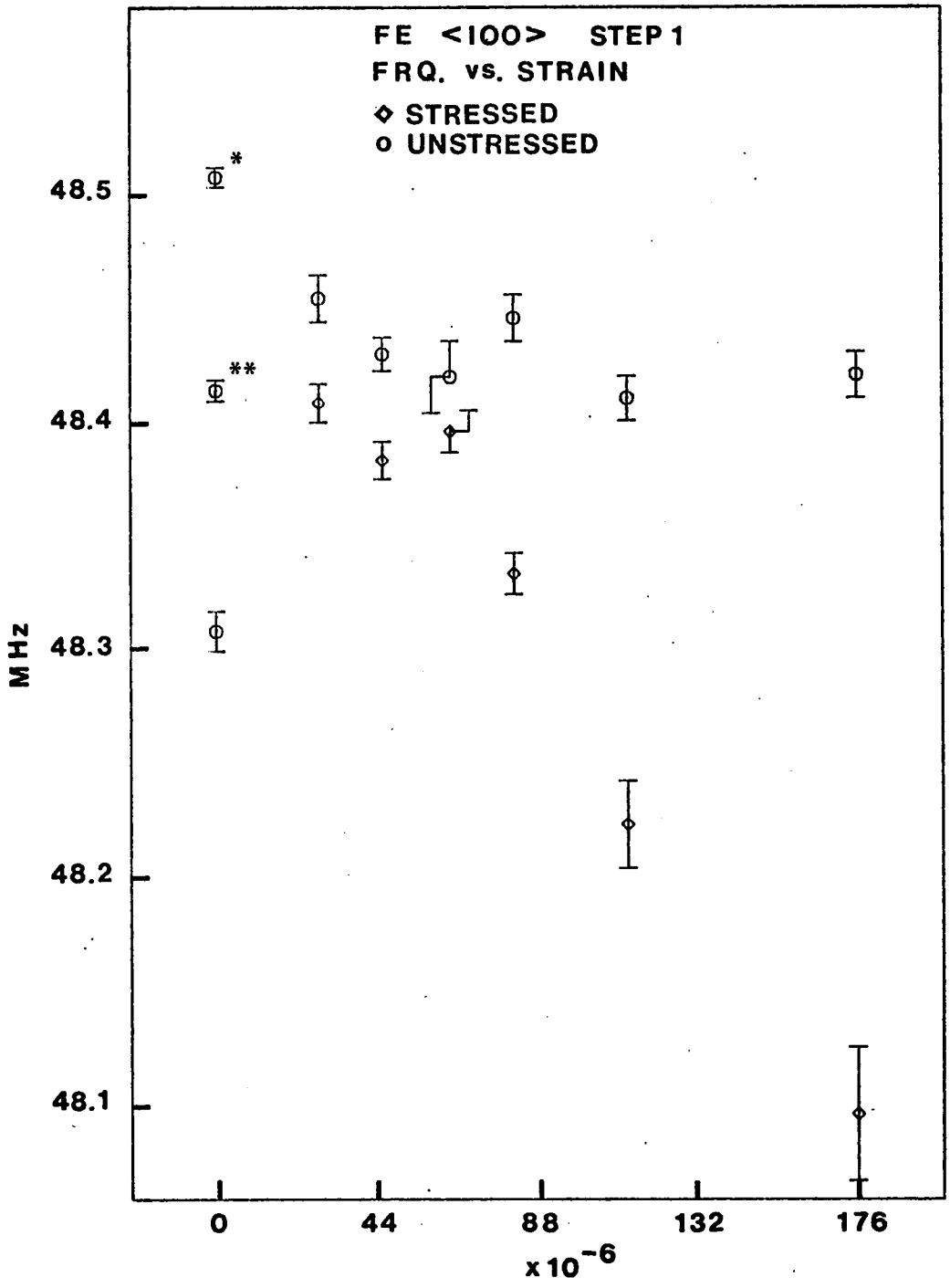

Fig. 25. * "in air" measurement
** measurement on the other face

a drop in frequency is rather surprising. However, when a strain of 28.3×10^{-6} was induced the frequency went slightly below the frequency previously measured (in air) on this face. Upon the removal of the external stress, the frequency fell between the two values in air. This can be thought of as relieving some of the initial residual strain difference between the two faces and of the possible disturbance created by the handling process. The rest of the measurements were performed on this face.

Also seen in Figure 25 is that changes in frequency were slight in the low strain region, an effect associated with the existence of domains aligned in directions other than the stress axis. As discussed in Chapter III, Bloch walls in Fe move to expand the volume of domains aligned along the axis of tensile stress. Beyond the critical strain, about 65×10^{-6} in this case, the frequency dropped linearly in strain indicating a full alignment of domains along favored directions.

Figure 26 shows the change in $\lambda_T (= 1/T_2)$ in this step. In the low strain region where domains are not fully aligned along the stress axis, the values of λ_T, or the differences between the stressed and released state, do not show a clear tendency. On the other hand, in the high strain region (induced strain $> 65 \times 10^{-6}$) λ_T increased systematically and also recovered well upon release of the external stress.

According to Arrott et al.[2] the local strain in an Fe crystal always decreases the frequency. Such a decrease in frequency was shown to be accompanied by an increase in λ_T as confirmed by Grynszpan et al.[1] The effect on λ_T was attributed to dislocations in both works. This

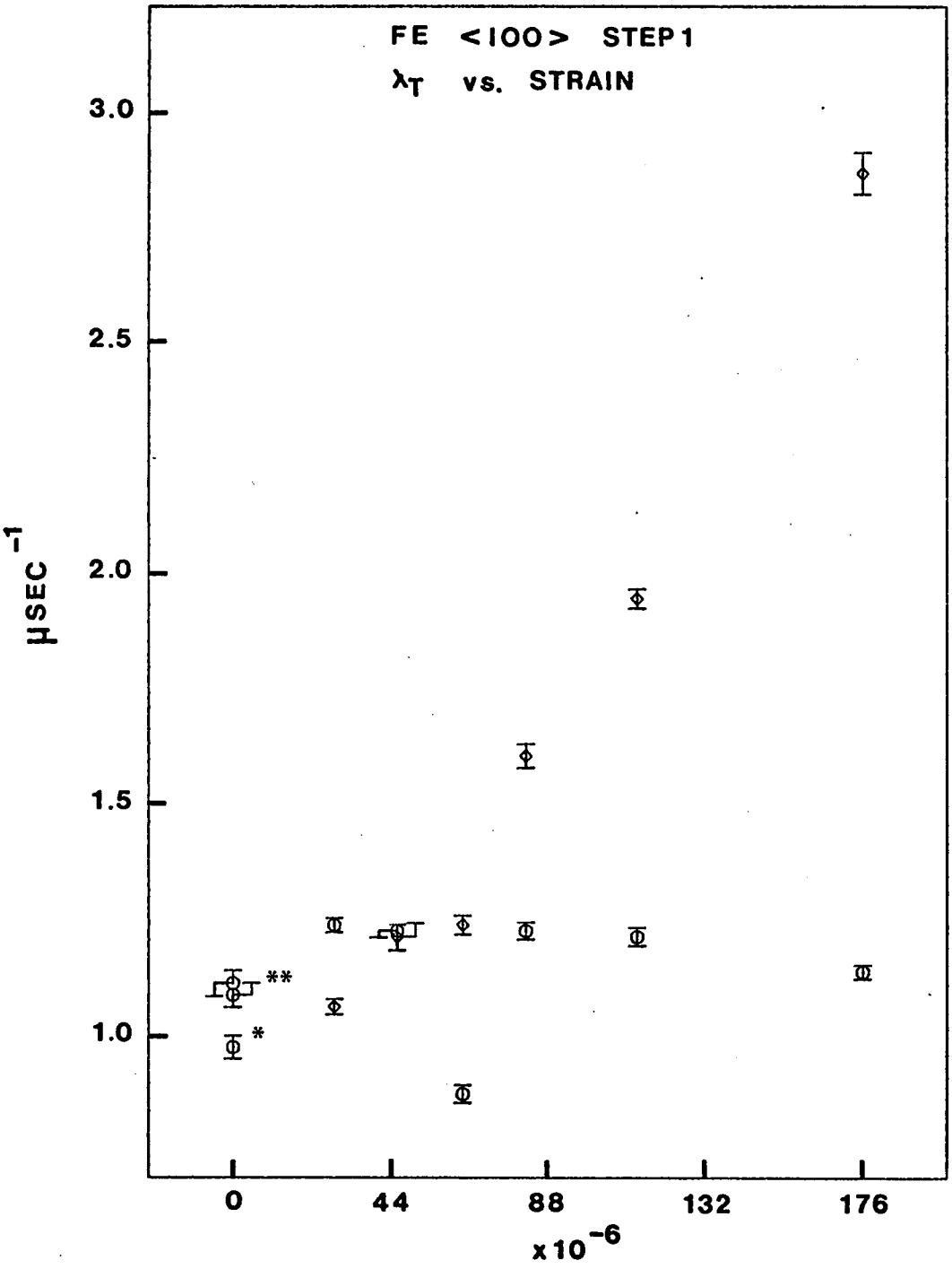
FE <100> STEP 1
λ_T vs. STRAIN
3.0
2.5
2.0
1.5
1.0
μSEC^{-1}
**
*
0
44
88
132
176
x10^{-6}

Fig. 26

indicates that the volume of material strained by dislocation increased upon application of the external stress and then returned to the original state when the stress was released.

It is well known that any dislocation line, not exactly parallel to the stress axis, moves when an external stress is applied to a specimen. This motion of the dislocation line is blocked either by impurities or other dislocations in the crystal. If the dislocation line is blocked at two points, called the pinning points, it bends.[3,42,43] Such a bending of dislocation lines can happen even under a very low external stress (far below the yield strength) and thus always increases the volume of material associated with the local strain. Although the increase in λ_T can be explained by the above argument, it is only qualitative and there is no clear evidence that the bending of the dislocations is the sole physical origin of the effect of stress on λ_T.

According to the Frank-Read dislocation multiplication mechanism,[42,43] a severely bent dislocation line forms a closed loop. Once created in the crystal, the closed loop can only be removed by a proper heat treatment. On the other hand, a line which is not severely bent returns to its original shape upon release of the external stress. The recovery of λ_T in the high strain region clearly indicates that the formation of closed loops is negligible.

The yield strength of an Fe single crystal is about 520 bar at room temperature.[44] The strain along the $\langle 100 \rangle$ -axis corresponding to this stress is 403×10^{-6}. A slip motion occurs when a single crystal is subjected to a high external stress. A portion of the crystal is divided

by thin discs (a few hundred angstrom thick) to form a slip band under a stress beyond the yield strength. In the slip band the relative motion between discs is constrained along certain directions on a crystallographic plane. The direction of slip motion is ⟨111⟩ on the ⟨110⟩ plane for a BCC crystal.[42] The critical shear stress in the ⟨111⟩ direction of an Fe crystal is 274 bar and it corresponds to a tensile stress of 577 bar along the ⟨100⟩ direction. The Frank-Read mechanism was proposed to explain the slip motion in a crystal. Therefore, by applying an uniaxial stress far below the yield stress, the formation of closed loops should not be serious.

The explanation of the effect of stress on λ_T in terms of the local strain immediately raises a question. If λ_T is increased by an increase in the local strain, whereas the effect of the local strain has been confirmed to decrease the frequency then was the decrease in frequency upon the external stress shown in Figure 25 due to the local strain? The answer is no. This will become clear from the observation of results in later steps.

Results on $\lambda_L (= 1/T_1)$ are plotted in Figure 27. The values scattered all around, showing no general tendency. However, for each pair of measurements λ_L is higher in the stressed state than it is in the released state. The mathematical expressions of λ_L and λ_T can be obtained from the Redfield theory and are written as follows:[45]

$$\lambda_L = \frac{1}{T_1} = \gamma_\mu^2 \left(\langle B_{\mu x}^2 \rangle + \langle B_{\mu z}^2 \rangle \right) \frac{\tau_c}{1 + \omega_\mu^2 \tau_c^2}$$

$$\lambda_T = \frac{1}{T_2} = \gamma_\mu^2 \langle B_{\mu z}^2 \rangle \tau_c + \frac{1}{T_1}$$

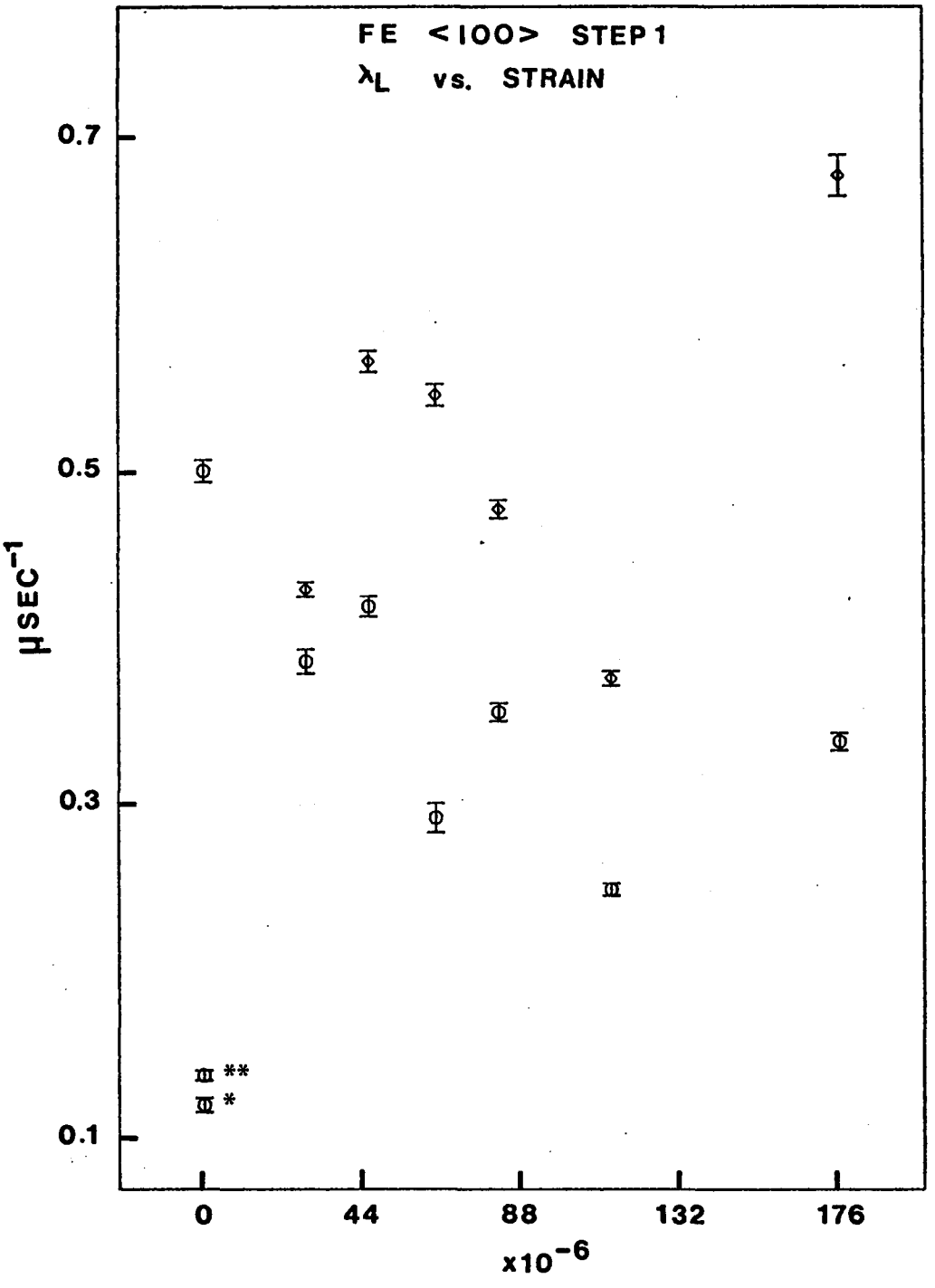
FE <100> STEP 1
λ_L vs. STRAIN
0.7
0.5
0.3
0.1
μSEC^{-1}
0
44
88
132
176
$x10^{-6}$
**
*

Fig. 27

where τ_c is the correlation time of the μ^+ at each site, ω_μ is the precessional frequency of the μ^+ spin and z is the direction of the domain magnetization. In the region free of local strain $\langle B_{\mu x}^2 \rangle$ and $\langle B_{\mu y}^2 \rangle$ are zero. This means the change in λ_L will be very sensitive to a local strain introduced into the region in which a muon diffuses. Therefore, the parameter λ_L can easily be affected by any irreversible change in the crystal and the fluctuation in values of λ_L in Figure 27 results.

Figure 28 shows the change in F_T/F_L as a function of the induced strain. The expressions for these parameters (defined in Appendix B) are rewritten here.

$$F_T = f_x \sin^2\theta_x + f_y \sin^2\theta_y + f_z \sin^2\theta_z$$

$$F_L = f_x \cos^2\theta_x + f_y \cos^2\theta_y + f_z \cos^2\theta_z$$

If we take the stress axis as the z-axis, the fractional volume of domains along the x-axis (i.e., oriented $\pm$ x) will be the same as that along the y-axis. Thus one gets: $f_x = f_y$. The sample was positioned such that $\theta_x = \pi/2 - \theta_y$ and $\theta_z = \pi/2$. Then, $F_T = f_x + f_z$ and $F_L = f_x$. This clearly indicates that F_T/F_L should increase as f_z increases at the expense of f_x and f_y. For an ideal crystal, without any local strain, the value of F_T/F_L must be infinity when domains are fully aligned along the stress axis which is perpendicular to the initial muon spin orientation. As shown in Figure 28 the largest value of this parameter was obtained when the sample was placed in the stress rig. This and the corresponding point in Figure 25 indicate that an accidental tensile stress was applied to the sample during this particular measurement. However, the value of

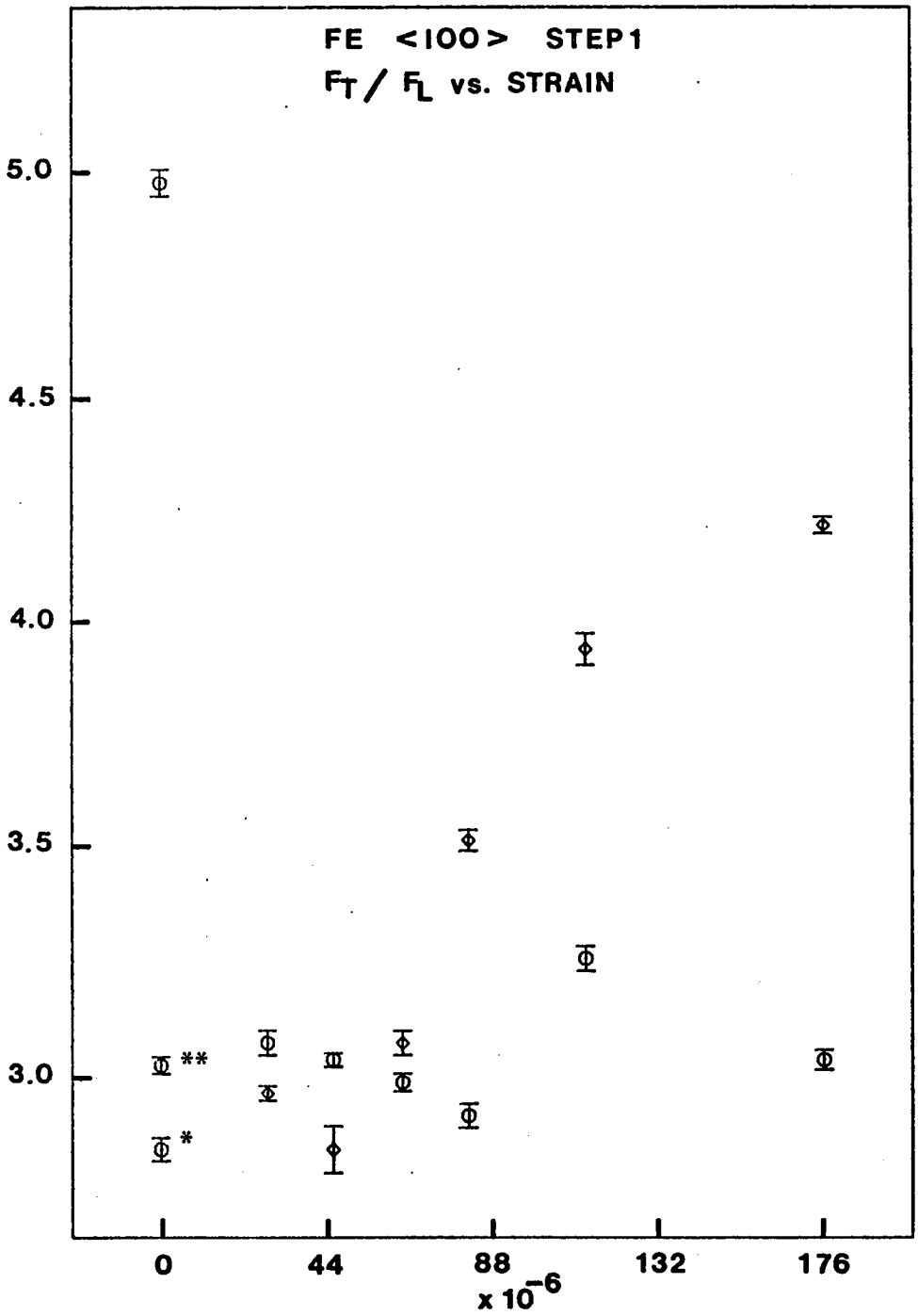

Fig. 28

F_T/F_L returned to its original value after the first stress cycle. After relieving the initial tension during the first stress cycle, subsequent measurements should have been unaffected by the arbitrary initial condition.

b. Step 2

In this step the measurements were performed by applying only the external magnetic field along the long axis of the sample. The change in the frequency is shown in Figure 29 as a function of the external field. Assuming the sample geometry is ellipsoidal, the demagnetizing field estimated with the formulas given by Osborn[46] is about 125 G when technical saturation is achieved. Since the direction of $\vec{B}_\mu$ is opposite to that of $\vec{M}_S$, the application of an external field which penetrates the sample must decrease the frequency and this is seen from the last three points in Figure 29.

The increase in frequency seen with the applied field lower than the demagnetizing field cannot be explained in a simple way. A model is proposed to explain this rise in frequency in a weak applied field and it will be discussed later in this section.

Figure 30 shows λ_T as a function of the applied field. The pecularity with λ_T's in this step is the rapid increase in magnitude upon the applied field. Since the geometry is not ellipsoidal, the demagnetizing field is not uniform in the sample. At H_{ext} = 125 G where the technical saturation is believed to be reached, $\lambda_T = 1.89\ (\mu\text{sec})^{-1}$. This value of λ_T corresponds to $\Delta H_{1/2}$ of 45 G. This almost agrees with the calculated inhomogeneity of the demagnetizing field in Appendix D. To explain

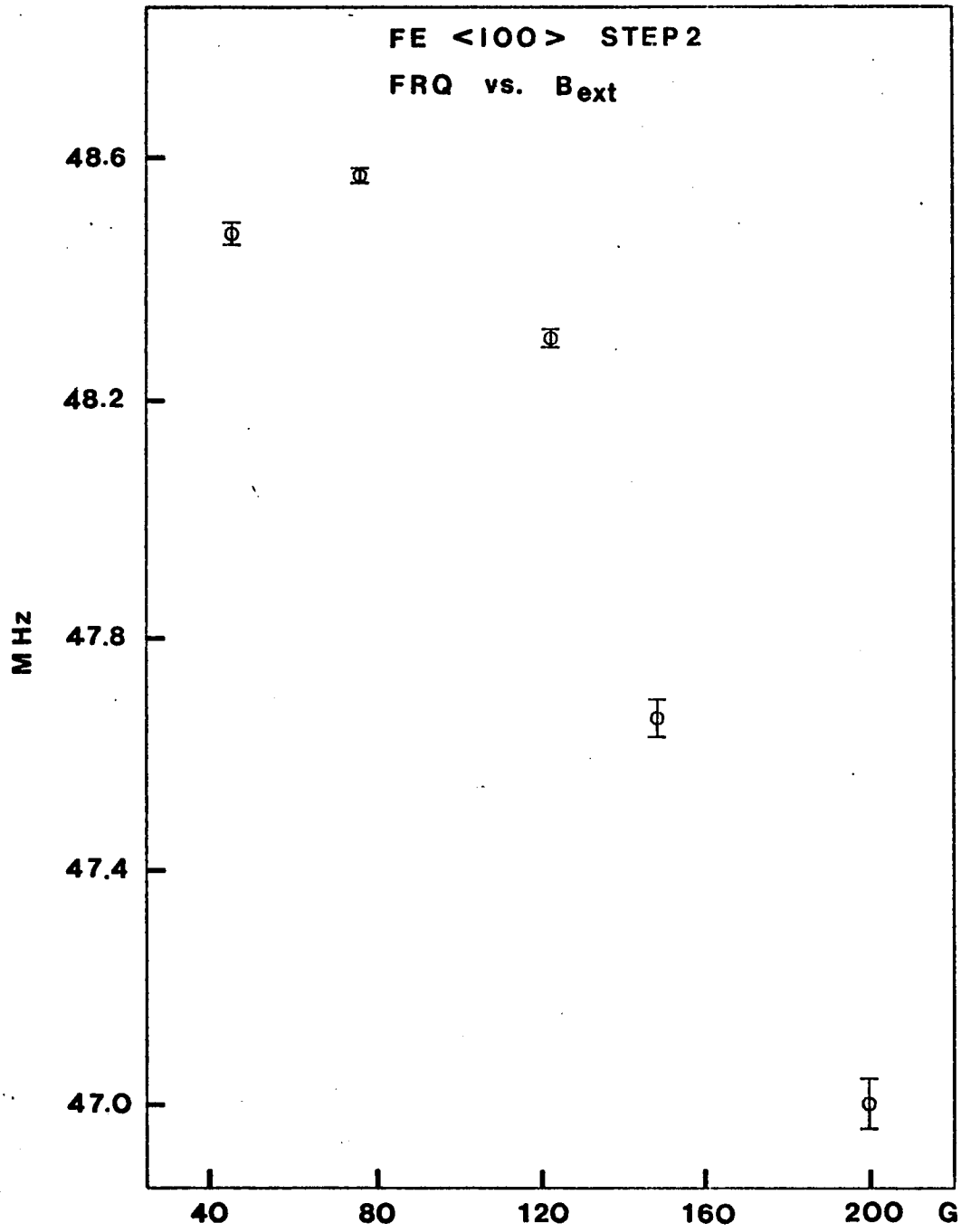
FE <100> STEP2
FRQ vs. Bext
48.6
48.2
47.8
47.4
47.0
MHz
40
80
120
160
200
G

Fig. 29

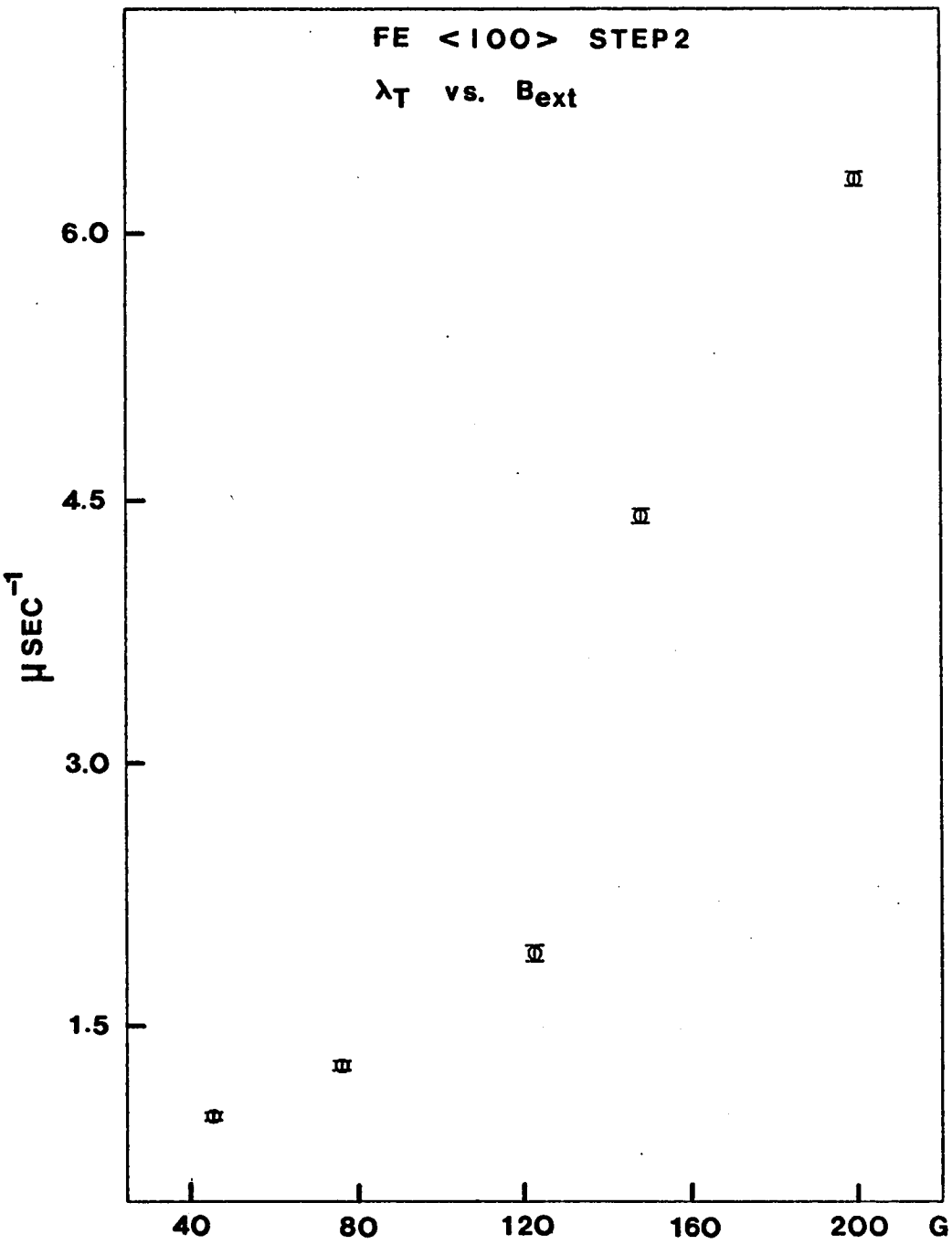
FE <100> STEP2
λ_T vs. B_{ext}
6.0
4.5
3.0
1.5
μSEC^{-1}
40
80
120
160
200
G

Fig. 30

the rapid increase in λ_T beyond this point, many ideas have been proposed but none of them is satisfactory. Thus it will not be discussed further.

The field dependences of λ_L and F_T/F_L shown in the next two figures (31 and 32) also have some peculiarities. The increase in λ_L by a weak applied field might be explained by the motion of Bloch walls in response to the field applied to reach saturation. This is because when Bloch walls tend to move or change their shape, the dislocation structure is altered by the interaction between Bloch walls and dislocation lines. Such an interaction usually causes a repulsive force between them. The effect is likely to increase the degree of local strain which increases λ_L. Then, the sudden decrease in λ_L at H_{ext} = 125 G must result from the mutual stable rearrangement between dislocations and Bloch walls since most of the walls passed over the highest potential peaks in their paths. The next point of λ_L at H_{ext} = 150 G has the highest value measured in this step. According to Träuble,[47] 90° Bloch walls produce long-range internal stresses and the interaction between these walls and dislocations is much stronger than that of 180° Bloch walls and dislocations. This means that 180° Bloch walls are more mobile than 90° Bloch walls. In addition to this, the pressure on 180° Bloch walls is twice that on 90° Bloch walls at a given H_{ext}. Therefore, only the motion of 180° walls is believed to be finished at H_{ext} = 125 G and 90° walls are yet to pass over the potential peaks. Then, at the external field higher than 125 G, only the 90° walls move.

Because the interaction is stronger, the local strain increase in this process is higher, resulting in a high value of λ_L. Upon finishing the motion of 90° Bloch walls λ_L returned to its value at H_{ext} = 125 G and it is seen at the point at H_{ext} = 200 G.

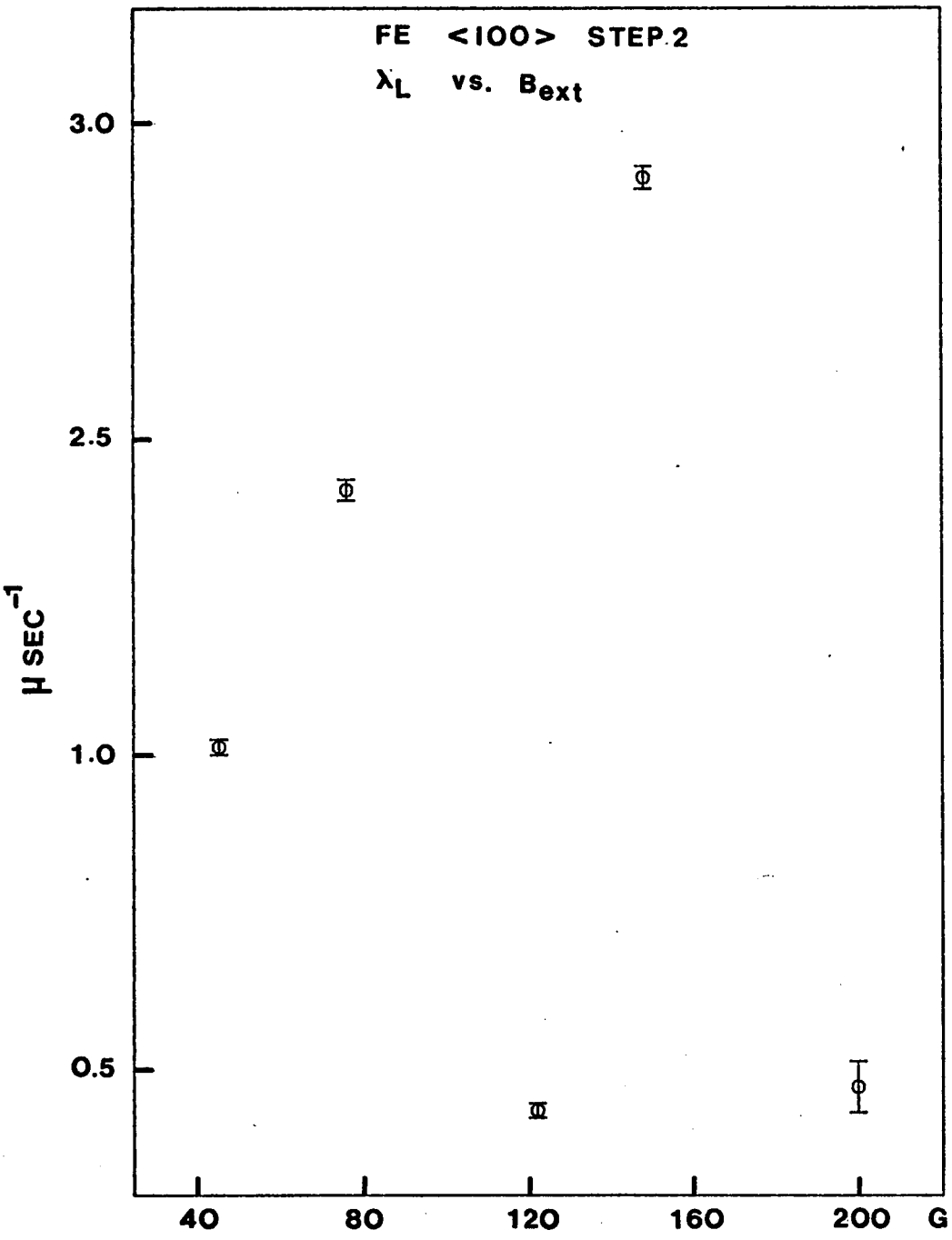
FE <100> STEP 2
λ_L vs. B_{ext}
3.0
2.5
1.0
0.5
μSEC^{-1}
40
80
120
160
200
G

Fig. 31

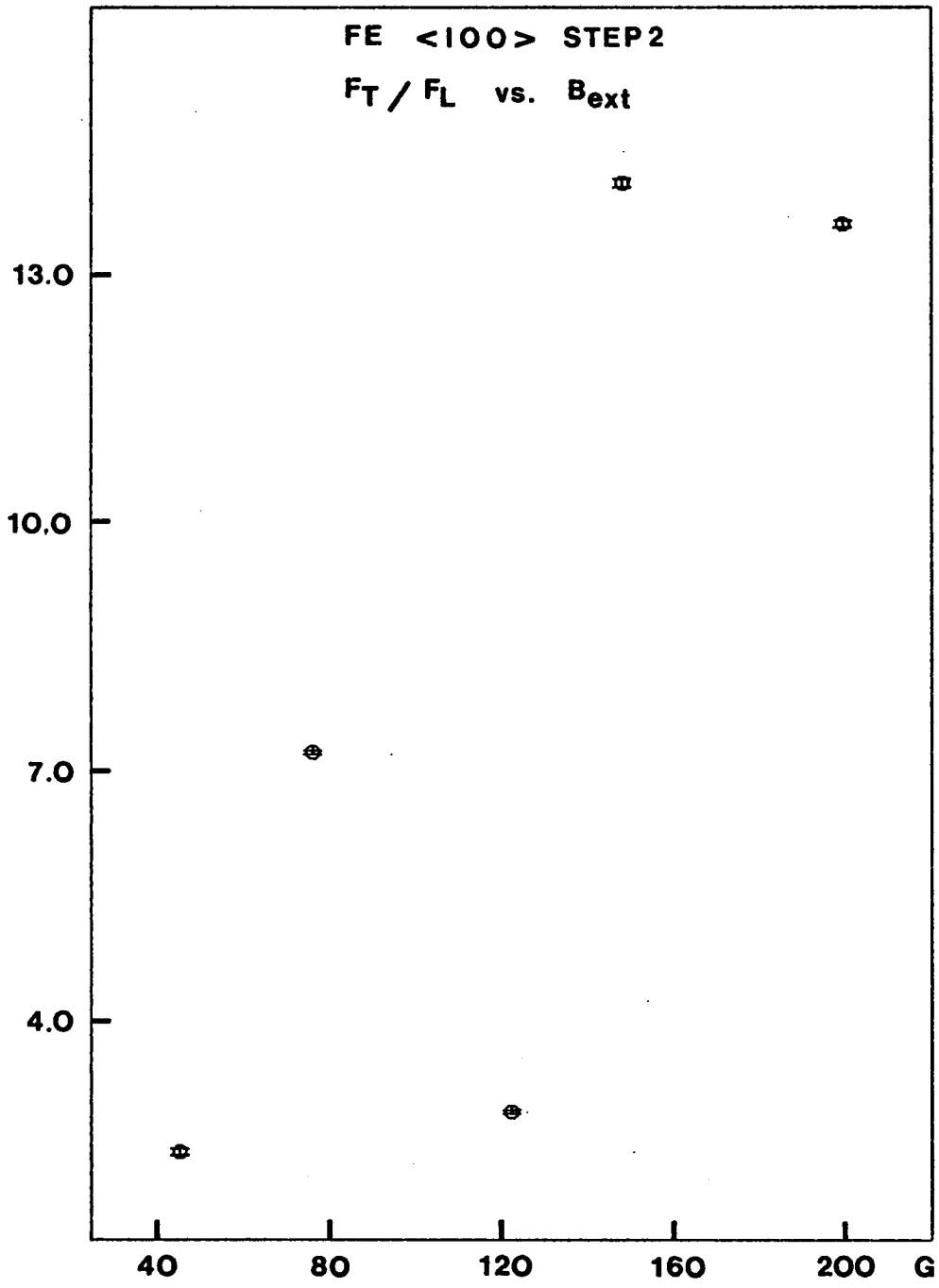

Fig. 32

The change in F_T/F_L shows a drop at H_{ext} = 125 G. This is not understood and will be left unexplained. Besides the peculiarity at H_{ext} = 150 G the values at the last two points are slightly annoying. Otherwise, the dependence of F_T/F_L on H_{ext} is what one can expect.

By applying the external field along the <100> -axis, the magnetostriction λ_{100} was also measured. Up to H_{ext} = 80 G there was no change in length of the sample but at H_{ext} = 125 G it was measured to be $\lambda_{100} = 26 \times 10^{-6}$ and was kept constant at higher values of H_{ext}. This value is somewhat higher than the usual one of 21×10^{-6} but it depends on each individual sample and its history.

c. Step 3

Here, measurements were performed by applying uniaxial stress under an external magnetic field along the same direction to that of the previous step but its magnitude was fixed at 150 G. Since changes in λ_T and λ_L are more difficult to understand in this step, only a few points will be discussed.

The important fact is the change in the frequency without initial hesitation in the low strain region of Figure 33. Because the technical saturation already has been accomplished, domains were aligned along one direction on the stress axis. With this the question which arose in Step 1 can be answered. The decrease in the frequency must be due to the pure tensile strain induced on the unit cells in the region of the crystal free (or nearly free) of local strain induced by lattice imperfections, mainly dislocations. If the decrease in frequency had been caused by the enhanced local strain then its dependence on the induced strain should have been of the same form in both Figures 25 and 33.

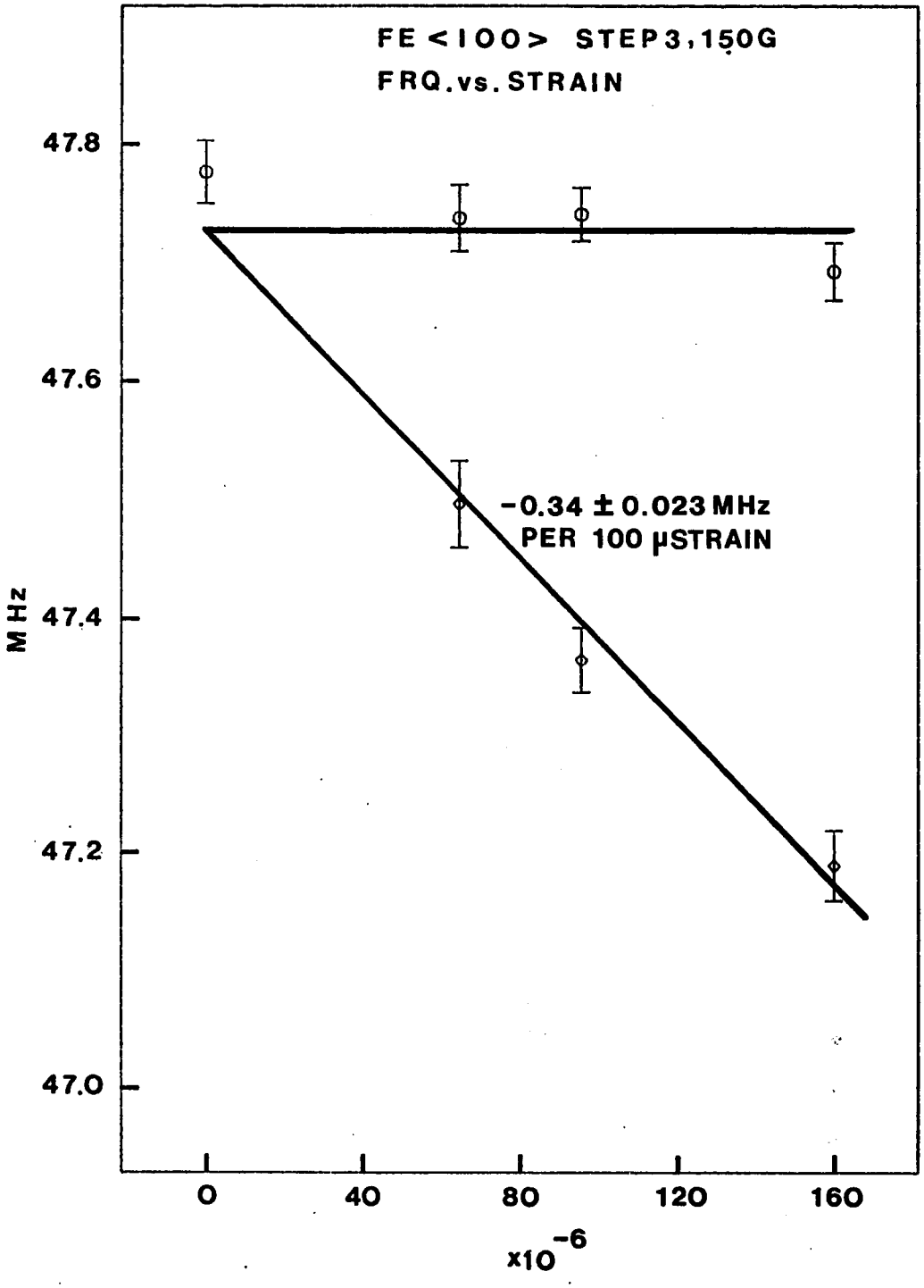
FE <100> STEP3,150G
FRQ.vs.STRAIN
47.8
47.6
47.4
47.2
47.0
MHz
-0.34 ± 0.023 MHz
PER 100 μSTRAIN
0
40
80
120
160
x10^-6

Fig. 33

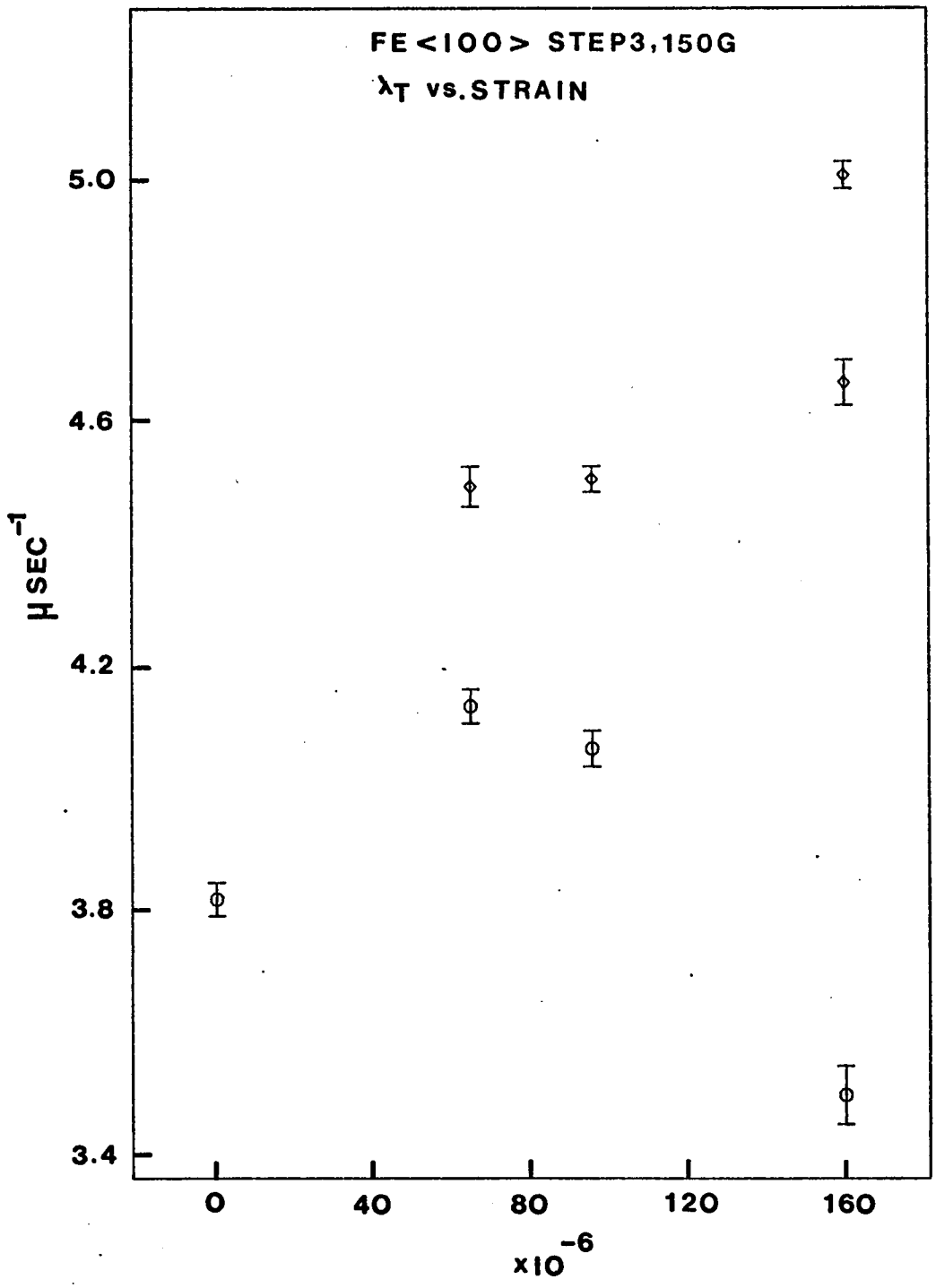
FE<100> STEP3,150G
λT vs.STRAIN
5.0
4.6
4.2
3.8
3.4
μSEC-1
0
40
80
120
160
x10-6

Fig. 34

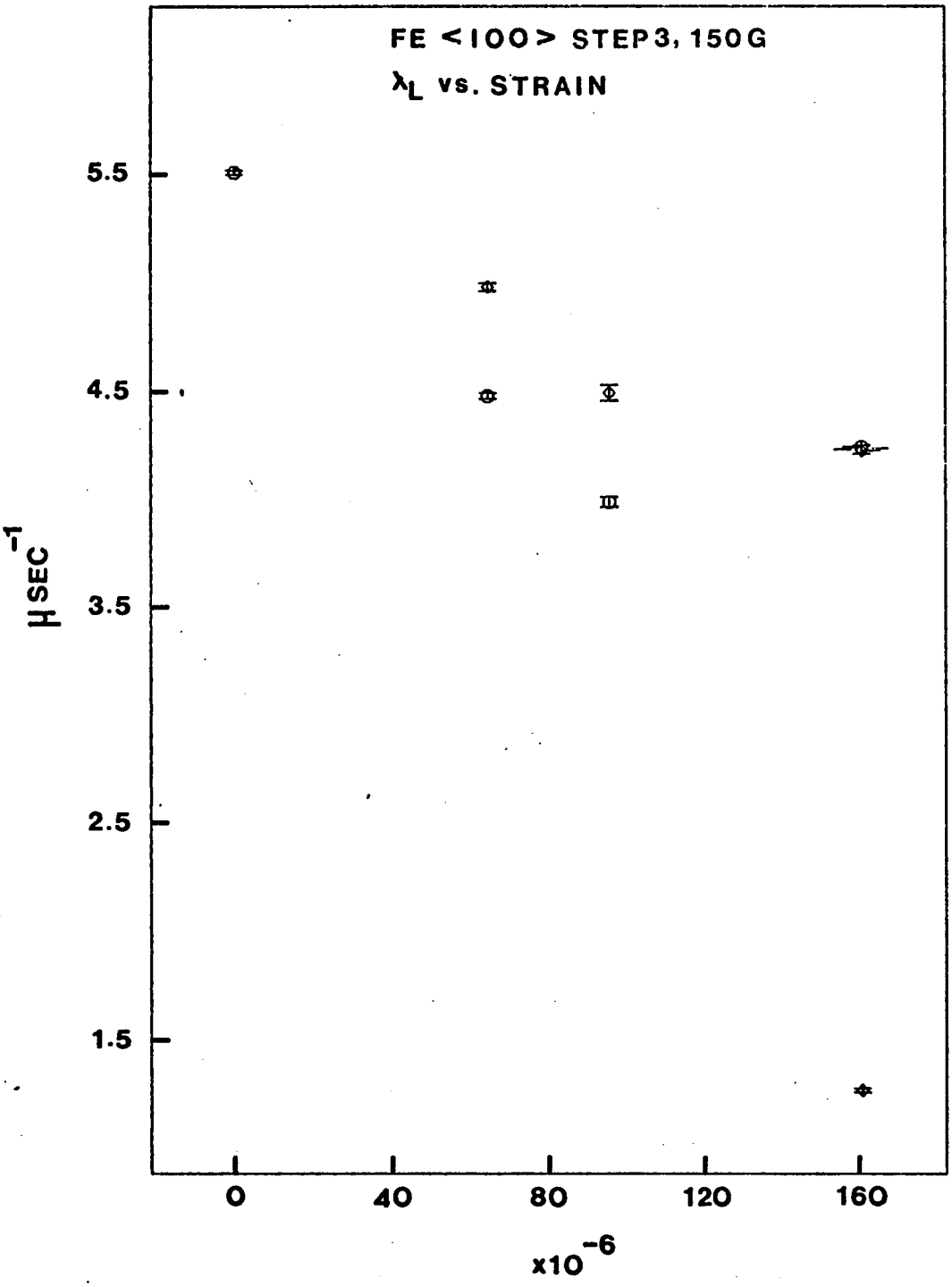
FE <100> STEP3, 150G
λ_L vs. STRAIN
5.5
4.5
3.5
2.5
1.5
μSEC^{-1}
0
40
80
120
160
$x10^{-6}$

Fig. 35

It is undoubtedly true that the frequency decreases in domains aligned along the axis of tensile stress. This means we need to prove that the frequency must increase in domains perpendicular to the tensile stress axis to explain the small change in frequency in the low strain region of step 1. In the case of the dipolar field it is trivial to prove that the sum of fields, in domains oriented along three different axes but strained in the same way, is always zero. However, the sum of hyperfine fields in three different domains cannot be shown to be zero. For this reason, the increase in frequency in domains perpendicular to the tensile stress axis will be proved later in this section after the interpretation of frequency decrease in favored domains.

The results for F_T/F_L plotted in Figure 36 are satisfactory in the sense that they are higher than those shown in Figure 28. This indicates that there existed a portion of domains not aligned along the stress axis in step 1. This is not surprising because each individual Bloch wall encounters different potential barriers along its path and a perfect alignment cannot be expected by a tensile stress alone. The values of F_T/F_L in Figure 36 are generally lower than those of Figure 32 and thus is not explained because in this step the tensile stress is believed to enhance the effect of the applied field in saturating the sample. The fluctuation of values of this parameter in Figure 36 also is not immediately explained.

d. Step 4

After turning off the external field, measurements were repeated. Since results in this step are similar to those of step 1, only a few remarks will be made.

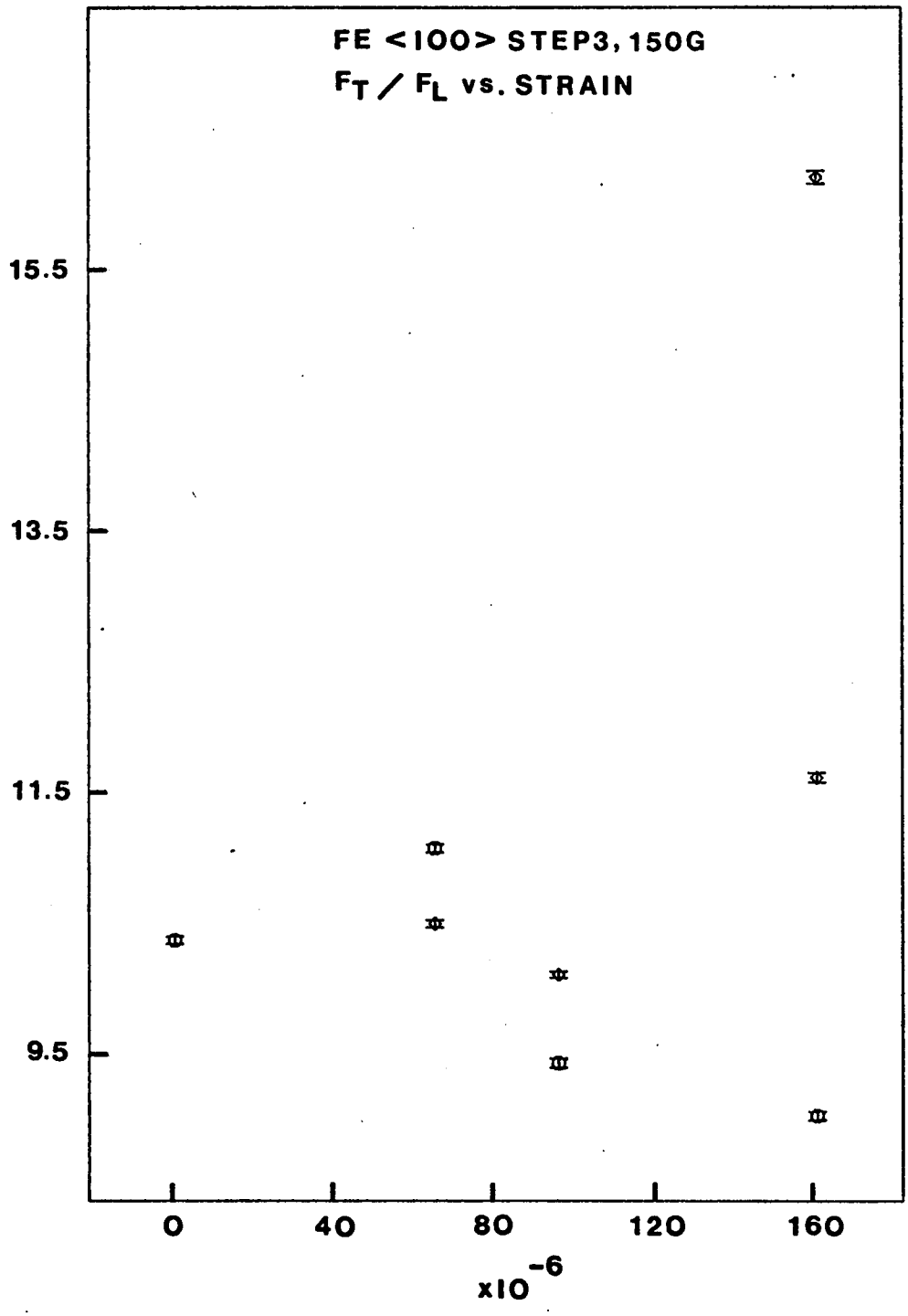
FE <100> STEP3, 150G
F_T / F_L vs. STRAIN
15.5
13.5
11.5
9.5
0
40
80
120
160
x10^{-6}

Fig. 36

The critical strain of domain alignment is seen to be 38×10^{-6} in this step (Figure 37). This is much smaller than that of 65×10^{-6} in step 1. As was discussed in Chapter III, the removal of external field after saturation always leaves the sample in a partially magnetized state. At this stage domain walls can easily move to expand the volume of favored domains without facing high potential barriers. Therefore, the critical strain for the domain alignment must be less in this step.

Results on λ_L plotted in Figure 39 show a completely different pattern which has never been observed in previous steps. Except for the first two points, the change in λ_L is very systematic and recovers well upon releasing the external stress. An indication from this result is that repeating the stress cycle under an external field in the previous step must have caused some drastic changes in the magnetic and structural properties of the sample. At the present moment we do not know what were the effects of such a treatment on the sample state.

Figure 40 shows the result on F_T/F_L in this step. The first point at zero strain has a high value because the sample was partially magnetized. After this, the sample was strained (22×10^{-6}) and F_T/F_L dropped slightly from its previous value. This is opposite to the change in F_T/F_L predicted by the wall motion due to a tensile stress.

Furthermore, when the stress was released it dropped down to 2.17, which is lower than any value previously obtained. Also, this value of F_T/F_L is very close to 2.0 for an ideal Fe single crystal sample, free of lattice imperfections, where domains are randomly distributed among the easy axes. The value of λ_L in Figure 39 corresponding to this

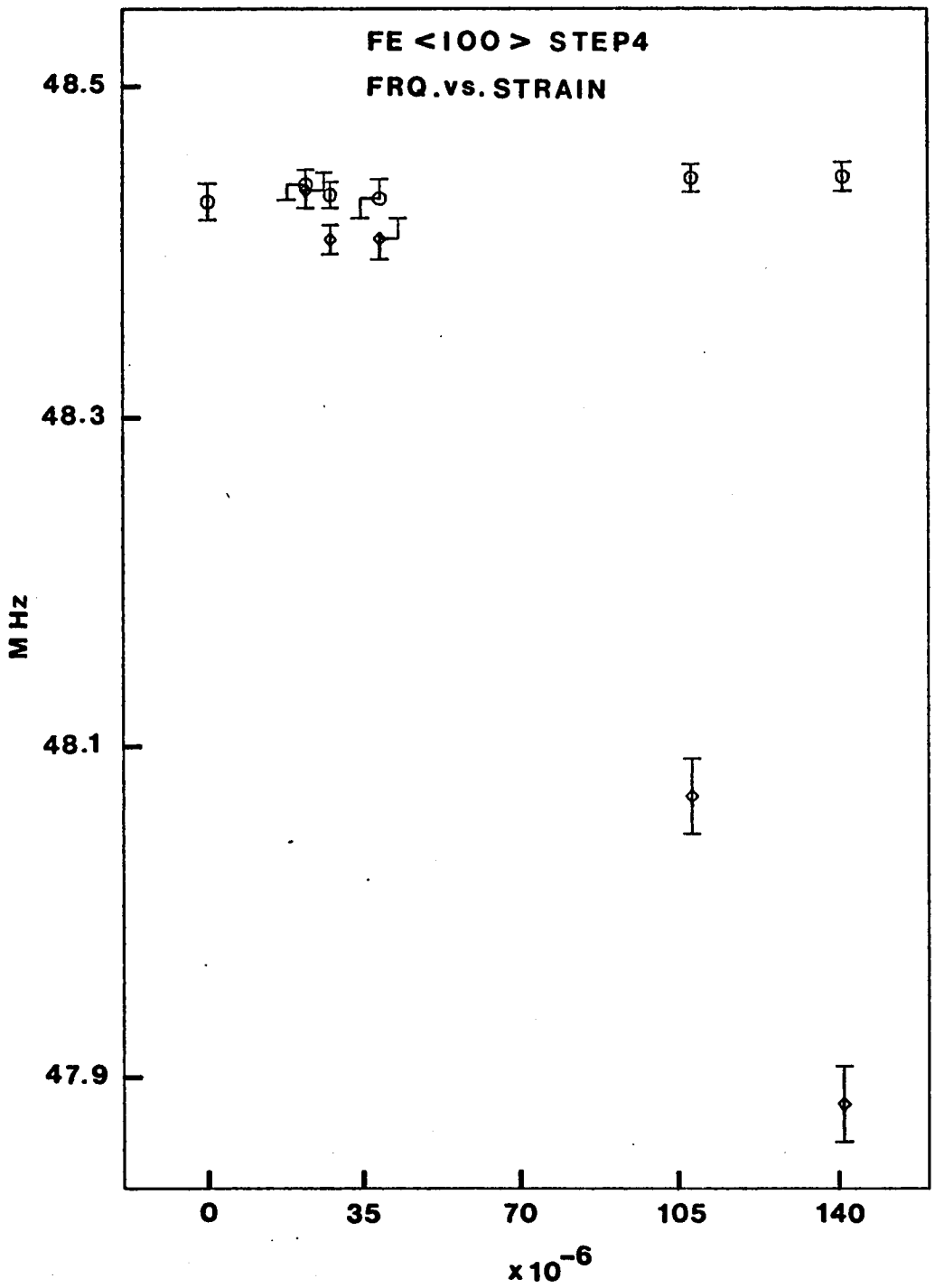
FE <100> STEP4
FRQ.vs.STRAIN
48.5
48.3
48.1
47.9
MHz
0
35
70
105
140
x10^-6

Fig. 37

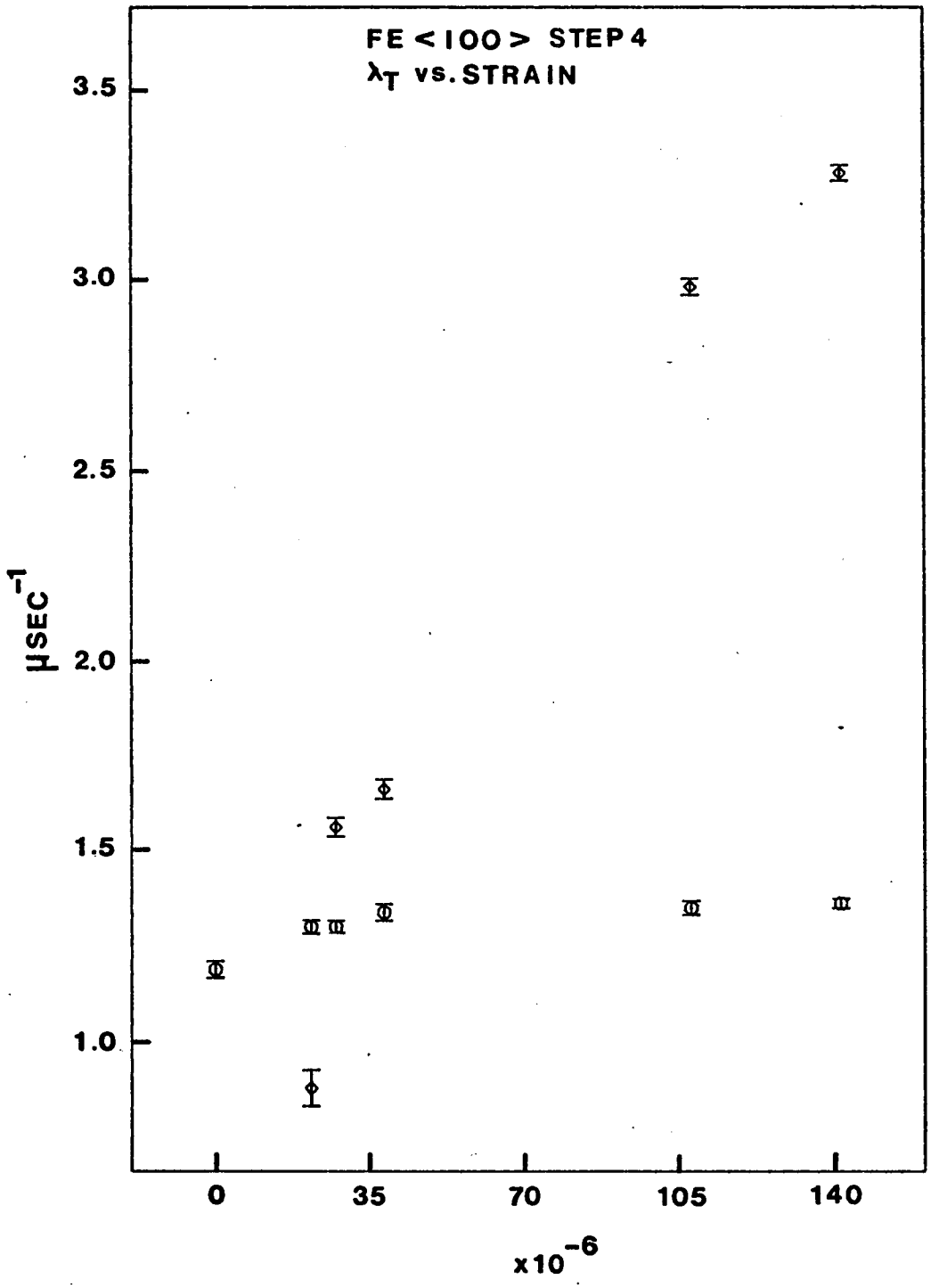
FE <100> STEP 4
λ_T vs. STRAIN
3.5
3.0
2.5
2.0
1.5
1.0
μSEC^{-1}
0
35
70
105
140
$x10^{-6}$

Fig. 38

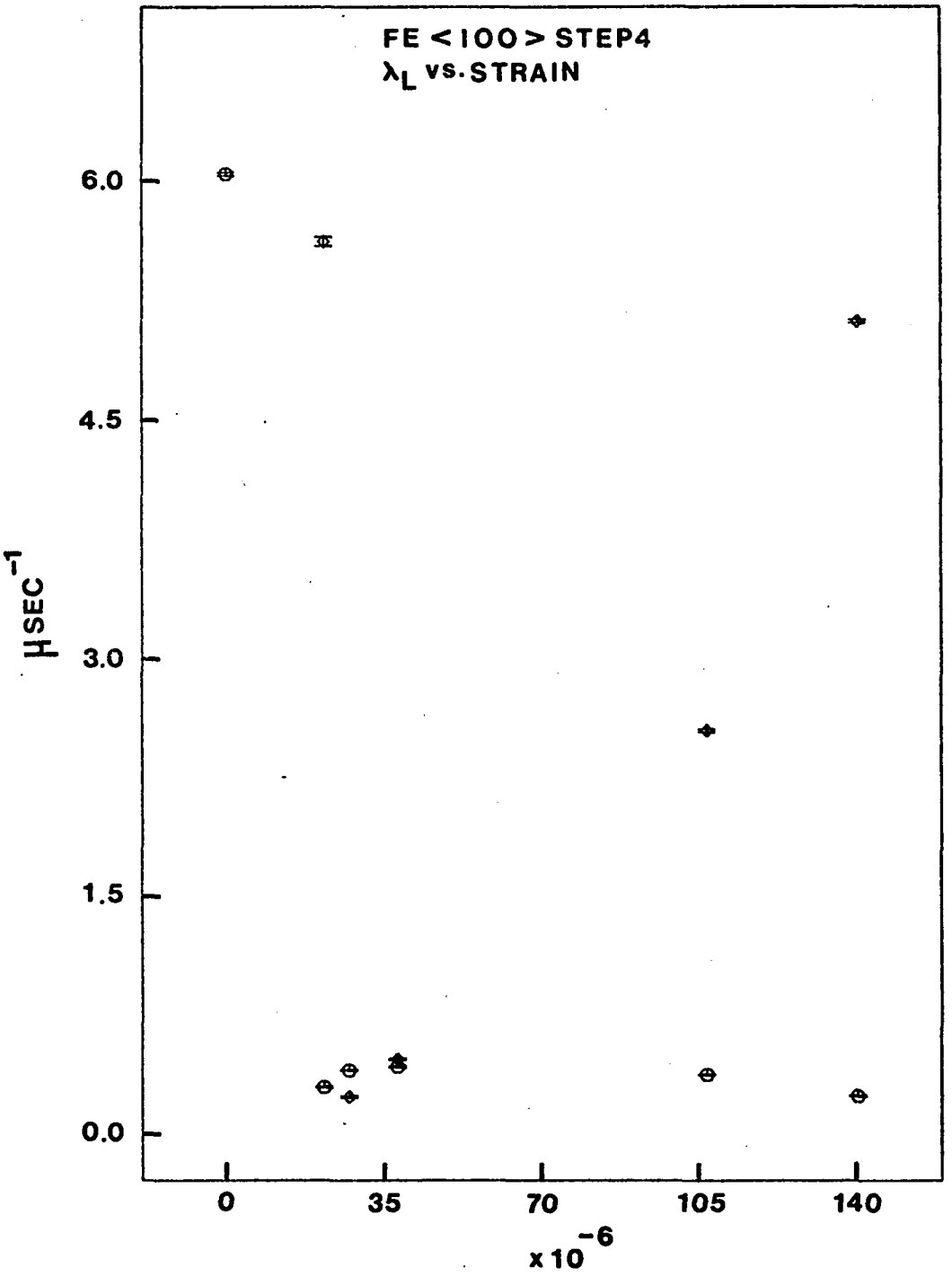
FE <100> STEP4
λ_L vs. STRAIN
6.0
4.5
3.0
1.5
0.0
μSEC^{-1}
0
35
70
105
140
$x 10^{-6}$

Fig. 39

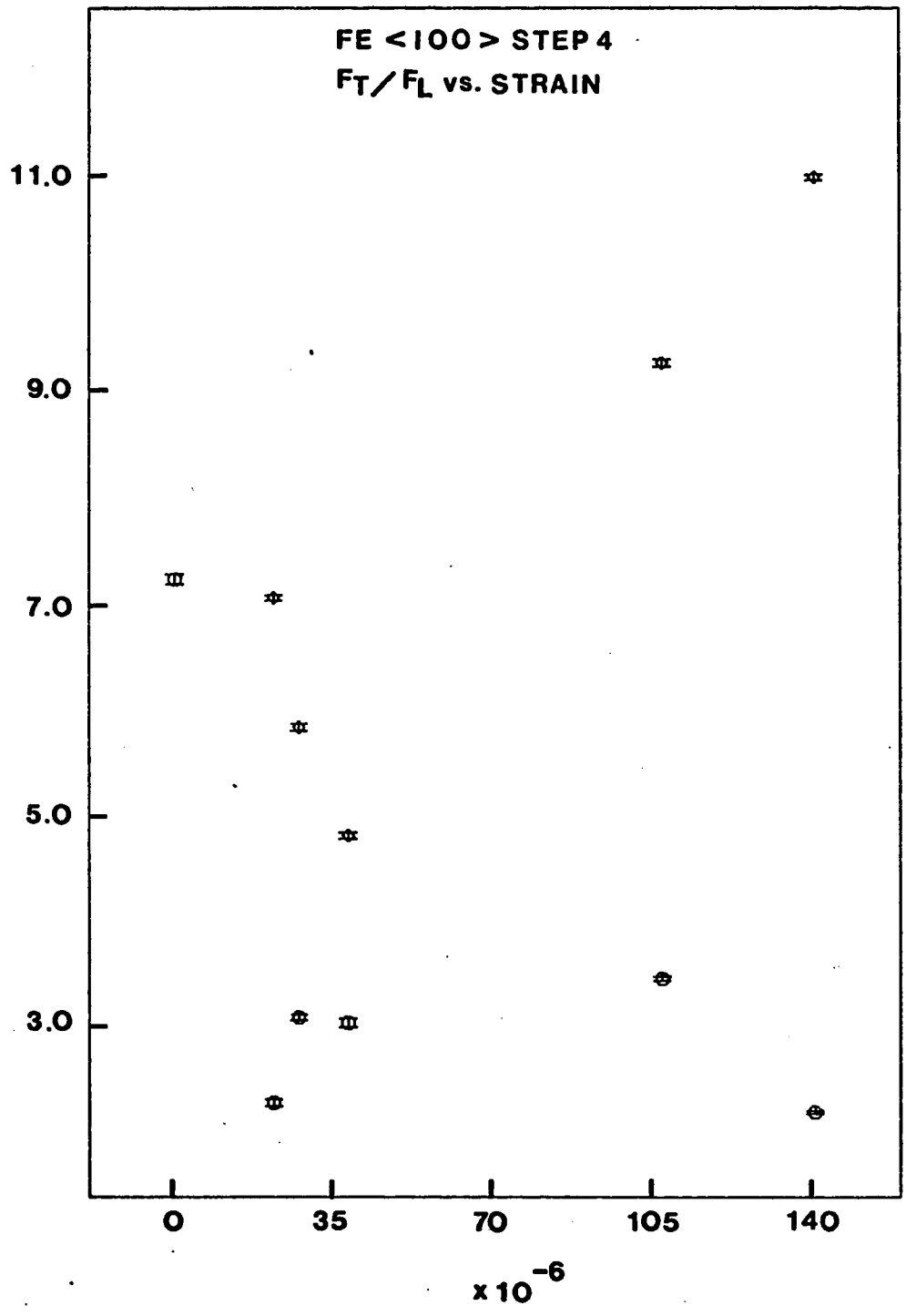

Fig. 40

point of F_T/F_L is also very low, indicating small variations in the longitudinal components of the local field, and seeming to imply that this F_T/F_L corresponds to an almost random distribution of domains.

An unmagnetized sample cannot be magnetized by an external uniaxial stress along, nor can a partially magnetized sample be brought into the unmagnetized state by a uniaxial stress along the magnetization axis,[33] provided that the external stress does not alter the shape of the potential surface, keeping the sample partially magnetized. Then, one might think that the small induced strain has affected the potential to bring the sample to a nearly unmagnetized state. This may be true but there is no clear evidence to support this argument.

B. Interpretation of the Results from the Fe ⟨100⟩ Sample

From the discussion given in the previous section it is clear that the stress dependence of certain parameters, like λ_T and λ_L, cannot be explained further. This is because they strongly depend on the history of the sample and it is extremely difficult to trace back the effect of previous treatment (mechanical and/or magnetic) in later measurements of these parameters. Therfore, in this section the interpretation will be made mainly upon the stress dependence of B_μ, the local field at the muon.

The slope of $\partial B_\mu / \partial \epsilon$ was taken from the results of step 3 (Figure 33) for an obvious reason. The average of the frequencies in released states was calculated to be 47.74 ± 0.125 MHz. The result of the stright line fit for four points gave $\partial B_\mu / \partial \epsilon = +25.1 \pm 1.70$ G/100μ strain. The sign of the slope was taken to be positive because the decrease in the magnitude of ω_μ means B_μ is less negative.

a. Contributions to the change in B_μ

From the expression of $\vec{B}_\mu$:

$$\vec{B}_\mu = \vec{B}_L + \vec{B}_d + \vec{B}_{hf} + \vec{B}_{ext} + \vec{B}_{dem}$$

the last two terms are independent of the induced strain and thus will not be considered. If we allow the Lorentz shpere to distort as the strain is induced in the crystal, the deviation of B_L from $4\pi M_s/3$ is -0.7 G/100 μ strain. This value is obtained by assuming that M_s is not changed by the external stress. Of course this is not true, but it will be seen to be negligible. However, if one calculated the dipolar field, B_d, inside a perfect sphere in the strained lattice the Lorentz field is still $(4\pi/3)M_s$ and the only thing to be considered is the change in M_s by the external stress.

As far as we know, no direct measurement of the dependence of M_s on the external uniaxial stress has been reported on pure Fe. The thermodynamic relation between variables including M_s and σ , uniaxial stress, can be written[30]

$$\left(\frac{\partial \lambda_s}{\partial H}\right)_{\sigma,T} = \left(\frac{\partial M_s}{\partial \sigma}\right)_{H,T}$$

where λ_s is the saturation magnetostriction along the external field H and the left hand side of the above equation is called the magnetostriction of paraprocess or the forced magnetostriction (see Figure 12). Calhoun et al.[48] have measured $(\partial \lambda_s / \partial H)_{\sigma,T}$ along various directions in a single crystal disk of pure Fe and the value along <100> was 2.3×10^{-10}/G at room temperature with no external stress. Therefore, we take $(\partial M_s/\partial \sigma)_{H,T} = 2.3 \times 10^{-4}$ G/bar and this is not expected to be significantly changed with

a high stress. From this one gets $\Delta M_s \simeq 0.12G$ at the yield strain of 400×10^{-6}. The smallness of this change in the saturation magnetization is indirectly confirmed by Belov's measurements in Fe alloys.[49] He demonstrated that $(\partial M_s / \partial \sigma)_{H,T}$ was anomalously high in alloys and it was almost undetectable in pure ferromagnetic metals. Furtherfore, $(\partial M_s / \partial \sigma)_{H,T}$ had a peak in the vicinity of the Curie temperature. On this basis, we conclude that the contribution of ΔM_s to B_L is negligible.

Under the experimental conditions of this work all terms contributing to B_μ are collinear and the vector notation is not needed. Differentiating B_μ with respect to the induced strain, we have

$$\partial B_\mu / \partial \epsilon = \partial \tilde{B}_d / \partial \epsilon + \partial \tilde{B}_{hf} / \partial \epsilon$$

Terms in the right hand side of the above equation are written as derivatives of averaged fields. This is because in Fe the rapid motion of a muon always averages both B_d and B_{hf} over magnetically inequivalent sites. The dipolar field at each site (not on the muon) is shown in Figure 41.

If an Fe crystal is unstrained $\tilde{B}_d$ is zero because the free energies of sites of each type (octa- or tetrahedral site) are the same. When the crystal symmetry is lowered by an external stress (other than hydrostatic pressure) $\tilde{B}_d$ is not zero any more and it can be calculated (see Appendix C). Hyperfine fields at magnetically inequivalent sites may also be different but we know that $B_{hf_1} \neq B_{hf_2} = B_{hf_3}$ under the situation illustrated in Figure 41.

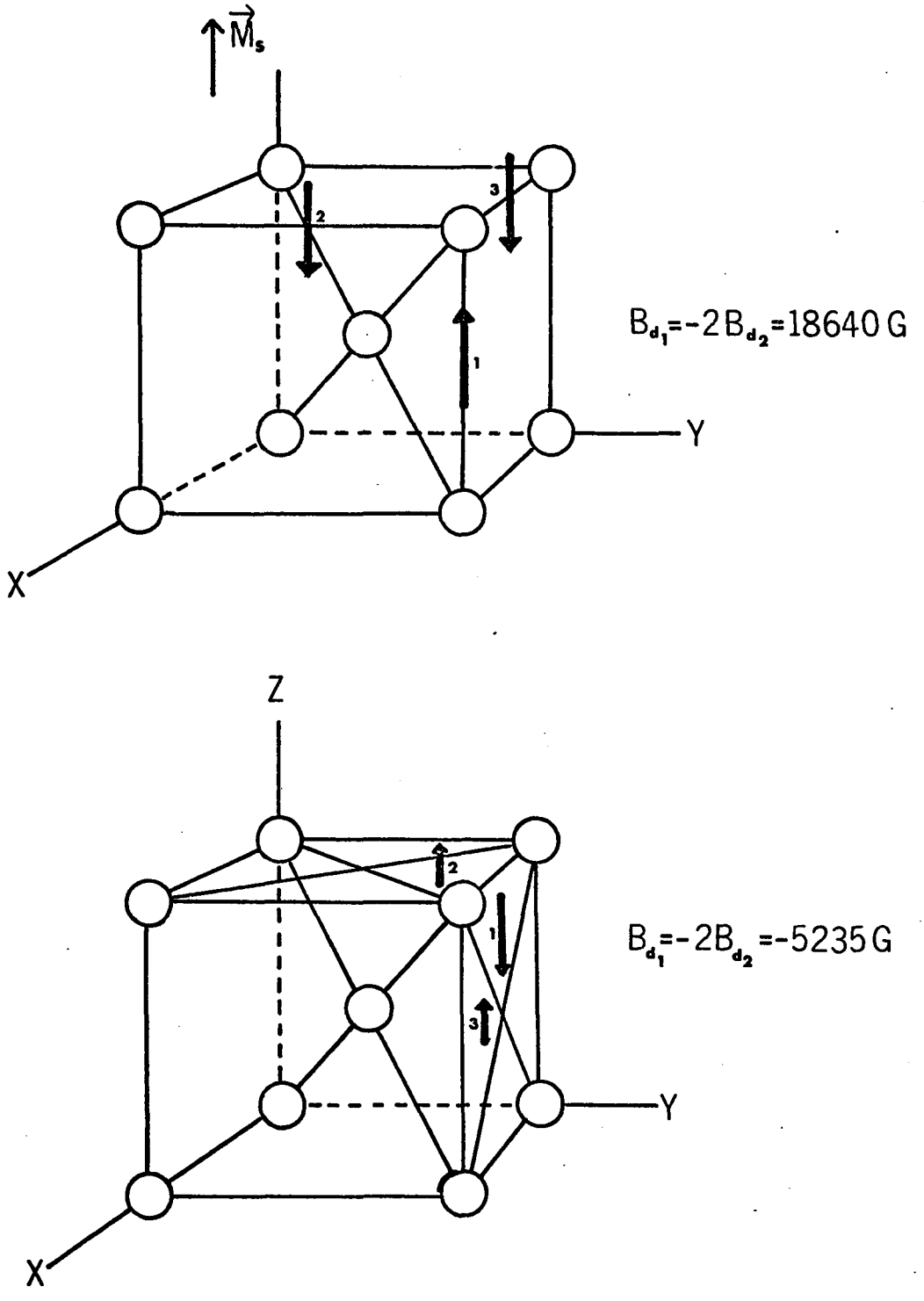

Fig. 41. The dipolar field at each site with (a) octahedral and (b) tetrahedral symmetry in the absence of the muon.

b. The change in B_{hf}

The hyperfine field at a muon is usually written as

$$\mathcal{B}_{hf} = -\frac{8\pi}{3}\eta(0)(n_0^+ - n_0^-)$$

where $\eta(0)$ represents the spin density enhancement by the presence of the muon and $(n_0^+ - n_0^-)$ is the intrinsic local magnetization at a site that a muon is to occupy. It is usually assumed that the change in $(n_0^+ - n_0^-)$ roughly follows that in M_s.

From the result of Hartman et al.[4], it is seen that $\Delta\tilde{B}_{hf} \simeq 0.97\, B_{hf}\frac{\Delta V}{V} \simeq -36$ for a volume strain of 300×10^{-6}, which corresponds to a linear strain of 100×10^{-6}. If we assume that $\Delta\tilde{B}_{hf} = \frac{1}{3}\sum_i \Delta B_{hf,i} = \Delta B_{hf,i}$ in the case of Hartman's experiment, the change in $B_{hf,i}$ due to the external uniaxial stress can be estimated.

Combining experimental results of $\partial \ln M_s/\partial p = -0.28 \times 10^{-3}$/k bar[50] and $\partial \ln V/\partial p = -0.59 \times 10^{-3}$/k bar,[51] one gets $\Delta M_s = \frac{\Delta V}{V} \times 0.475 M_s$. With this it can be estimated that $\Delta M_s = 0.234$ G per the volume strain of 300×10^{-6}, by the application of a hypothetical inverse hydrostatic pressure, which corresponds to a linear strain of 100×10^{-6}. Thus we can say that the linear strain of 400×10^{-6} by the inverse hydrostatic pressure will produce $\Delta M_s = 0.936$ G. This value is much higher than that of 0.12 G previously obtained for the uniaxial strain of 400×10^{-6}.

According to Kondoroskii et al.,[52,53] an external hydrostatic pressure changes values of exchange integrals by changing interatomic distances. Such changes in exchange integrals alter the molecular field acting upon the conduction electrons, thus affecting M_s. The transfer of

electrons from the s band to d band, or vice versa, occurs under lattice compression (see References 50, 52 and 53 for details). Therefore, the smaller value of ΔM_s by a uniaxial stress, compared with that caused by a corresponding hydrostatic pressure, indicates that the effect on the local electronic structure must be smaller in the case of uniaxial stress.

A shift of $\Delta B_{hf} \simeq -0.3$ G for a linear strain of 100×10^{-6} by a uniaxial stress applied along the $\langle 100 \rangle$ -axis of Fe is obtained with the assumptions summarized below:

i) a linear relationship between $(n_0^+ - n_0^-)$ and M_s

ii) no significant difference between changes in $\eta(0)$ by hydrostatic and uniaxial stress

iii) $\Delta \tilde{B}_{hf} = \Delta B_{hf}$ from the measurements by Hartman et al.

It should be noted that, by (iii) above, we are tentatively assuming the same (or almost same) magnitude of the hyperfine field at sites of each type. This means that the hyperfine field should not significantly depend on sites of one type. Figure 42 shows the local magnetic moment distribution in an Fe unit cell deduced from the neutron scattering experiment.[54] According to this figure, the local magnetization is the same at the three sites of octa- or tetrahedral symmetry.

c. The change in the muon-occupation-probability at an interstitial site

Host atoms around an interstitial site occupied by a muon displace to form an elastic dipole as discussed in Chapter IV. Not considering the magnetostriction, that is the fact that the edge of a unit cell in Fe is slightly longer along the direction of M_s, elastic dipoles at three sites, with the same symmetry, are initially in the same free

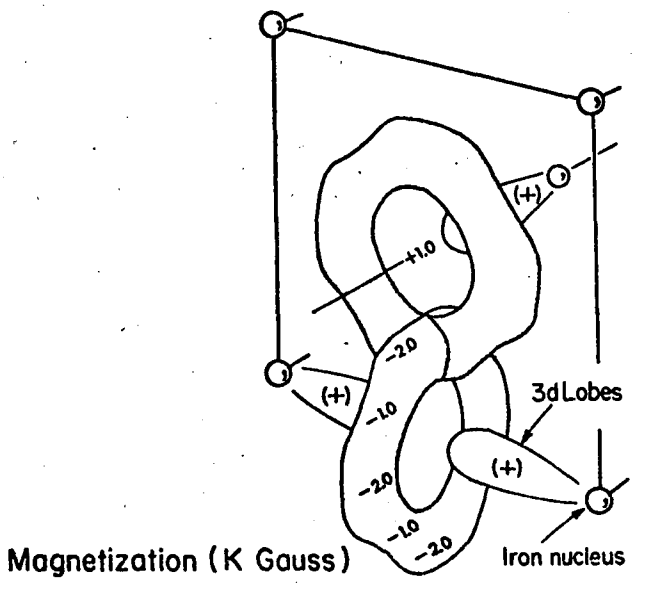

Fig. 42. Local magnetization in an Fe unit cell measured by neutron scattering experiment. Reproduced from Reference 54.

energy level. An external stress applied along the ⟨100⟩ axis removes the degeneracy of this energy level as shown in Figure 24. From equation (4.21) the difference between energy levels is

$$\Delta g = -(S_{11} - S_{12})(P_1 - P_2)\sigma$$
$$= -(S_{11} - S_{12})/S_{11} \cdot (P_1 - P_2) S_{11}\sigma$$

The factor $(s_{11} - S_{12})/S_{11}$ is estimated to be 1.374 and $S_{11}\sigma$ is the strain induced along the ⟨100⟩ -axis. Hence the above expression of Δg can be rewritten as, in the case of Fe,

$$\Delta g = -1.374 (P_1 - P_2) \epsilon_{100}$$

The notation convention is: $\Delta g \equiv g_1 - g_2$ and g_1 is the free energy of site 1 where the tetragonal axis is parallel to the stress axis. For example, for octahedral sites, $P_1 > P_2$ and by a tensile stress g_1 becomes lower than g_2.

The value of $(P_1 - P_2)$ is not available for the muon in Fe. However, from the results of calculations by Sugimoto et al.[55] in Nb we can approximate a value for Fe. Their results for the muon in Nb are reproduced in Table 5(a). The configurations of 1T, 4T(0) and 6T are shown in Figure 43. They also studied for hydrogen the effects on the numerical results when the lattice parameter is reduced. These are shown in Table 5(b). From this they found that the reduction of the lattice parameter always tends to stabilize the 4T(0) configuration. For hydrogen, this can be seen from the values of $E_{1T} - E_{4T}$ in cases 1 and 3 in Table 5(b).

Since the lattice constant of Fe is smaller than that of Nb (2.87 A° vs. 3.3A°), parameter values in Table 5(a) should be different

Table 5(a)* Properties of the self-trapped state of positive muons in Nb

Configuration	Energies (eV) ΔE_0	E_L	ΔE	Displacements (a/200) first neighbor u_1	u_2	second neighbor u_3	u_3	TrP (eV)	P tensor $3(P_1-P_2)/TrP$
1T	-1.367	0.429	-0.938	8.6	3.1	-0.3	-0.2	12.90	-0.25
4T	-1.435	0.454	-0.981	14.4		0.8		11.18	0.93
6T	-1.151	0.454	-0.697	7.1		3.0	0.0	15.16	0.19

*Reproduced from Reference 55

Table 5(b)* Self-trapping energy and double-force tensor of H atoms in 1T and 4T configurations in group-V Metals.

Case	a(Å)	Element†	Potential parameters	Self-trapping energies (eV) ΔE_{1T}	ΔE_{4T}	$\Delta E_{1T}-\Delta E_{4T}$	P tensor TrP(eV) 1T	4T	$3(P_1-P_2)/TrP$ 1T	4T	Note
1	3.3	Nb	ρ_1,ρ_2	-0.476	-0.423	-0.053	10.35	9.42	-0.12	0.85	H in Nb
2	3.3	Ta	ρ_1,ρ_2	-0.429	-0.372	-0.057	10.96	10.18	-0.15	0.76	H in Ta
3	3.0	Nb	ρ_1,ρ_2	-0.429	-0.385	-0.044	10.13	9.11	-0.11	0.87	
4	3.0	Nb	(ρ_1,ρ_2)x3.0/3.3	-0.494	-0.447	-0.047	10.48	9.47	-0.13	0.89	
5	3.0	V	(ρ_1,ρ_2)x3.0/3.3	-0.523	-0.493	-0.030	10.13	8.85	-0.11	0.89	H in V

†Element for which the Green's function was calculated.

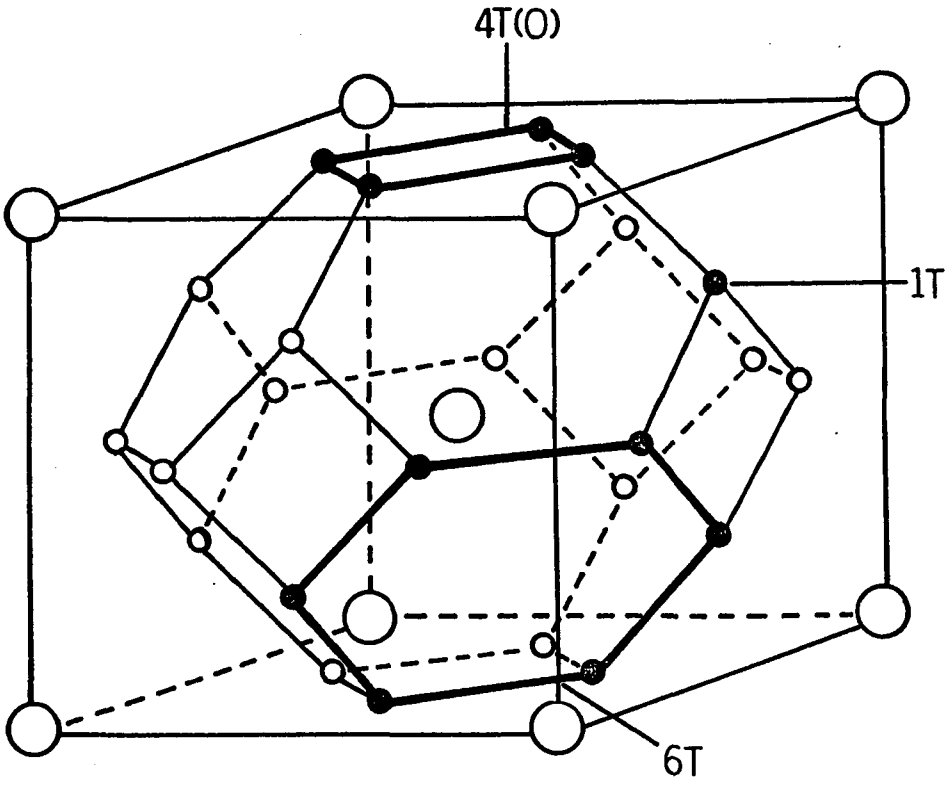

Fig. 43. Three possible occupational configurations of interstitials in a BCC crystal.

for Fe. For a simple comparison, (P_1-P_2) was calculated for each configuration from line 1 and line 4 in Table 5(b). The magnitude of (P_1-P_2) increased by 9.7% and 5.3% for 1T and 4T(0)-configurations, respectively, upon reducing the lattice parameter from 3.3 A° to 3.0A°. Assuming linearity, changes in (P_1-P_2) will be 13.9% and 7.5% for 1T and 4T(0)-configurations, respectively, by reducing the lattice parameter from 3.3 A° to 2.87 A°. Applying the same rates of change, values of (P_1-P_2) for the muon in Nb are estimated as given below.

Configuration	$(P_1-P_2)$for 3.3 A°	(P_1-P_2) for 2.87 A°
1T	-1.075	-1.23
4T(0)	3.466	3.73

The unit of (P_1-P_2) is electron-volt. We assume that values of (P_1-P_2) in Fe should be close to those in the second column.

d. The stress dependence of B_μ

In part c of this section the change in B_{hf} at any site has been estimated to be about-0.3 G per 100 μ strain. Since several assumptions have been made to get this result, the numerical value may not be accurate but the order of magnitude should be correct. Hence neglecting this change in the individual B_{hf}, we can write

$$\frac{\partial B_\mu}{\partial \epsilon} = \sum_i \left(\frac{\partial B_{d,i}}{\partial \epsilon} f_i(\epsilon=0) + \frac{\partial f_i}{\partial \epsilon} B_{d,i}(\epsilon=0) \right) + \sum_i \frac{\partial f_i}{\partial \epsilon} B_{hf,i}$$

If we assume $B_{hf,1} = B_{hf,2}(=B_{hf,3})$, the last term vanishes. Then the change in B_μ upon the external stress results from the change in B_d, and the interpretation of the stress dependence of B_μ is straightforward.

Remembering that the direction of $\vec{B}_\mu$ is opposite to that of $\vec{M}_s$, it is clear that $\tilde{B}_d$ must be parallel to $\vec{M}_s$. As shown in Figure 41, for octahedral sites, the muon spends more time at site 1 when the unit cell is strained along M_s. The dipolar field at site 1(2) is +18.46 (-9.23) kG and so even a 0.1% increase of the muon correlation time for site 1 will cause an increase of 27.7 G in the averaged dipolar field.

In the case of tetrahedral sites the muon spends less time at site 1 and $B_{d,1}$ is negative there. Thus the resulting effect on B_d will be the same, that is, positive. Therefore, regardless of the type of sites that the muon occupies, B_d always contributes to a decrease in the frequency if the domain magnetization is aligned with the axis of the tensile stress applied along one of the crystal axes.

The slow decrease in frequency at low strain regions of steps 1 and 2 can easily be explained. For this we do not need the assumption that the $B_{hf,1}$'s are all the same. Suppose there are three unit cells all strained in the same direction but magnetized in different directions. We can overlap these unit cells such that three different octa-or tetrahedral sites are brought into a point and their magnetizations point in one direction. As shown in Figure 44, the resultant crystal is spherically symmetric about the origin and the total dipolar field at this origin must be zero (see Appendix C). Therefore, the decrease in frequency in the domain aligned along the stress axis is always compensated by the frequency increase in other domains.

If we assume that $B_{hf,i}$'s are all the same at sites of octa- or tetrahedral symmetry, B_{hf} should be zero. Even though they are not

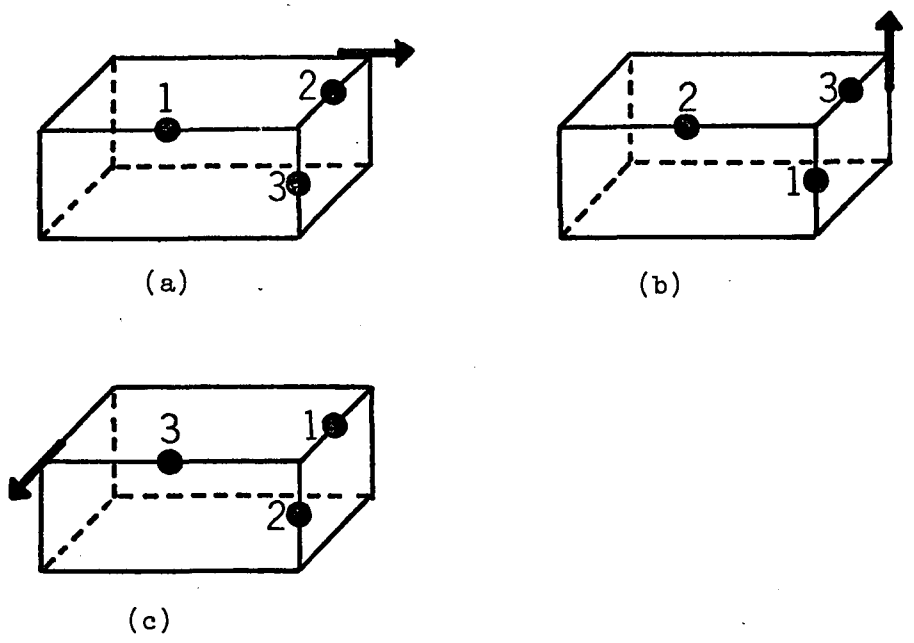

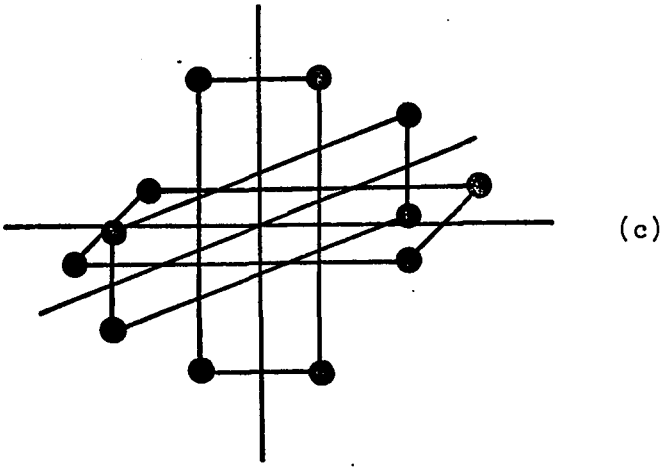

Fig. 44. Overlapping of the three sites of (a), (b) and (c) forms a crystal which is spherically symmetric about its origin as shown in (d). These show that the dipolar field averaged over a region of the sample must be zero.

the same, we can see that B_{hf} should be close to zero in the low strain region. This is because the summation of Δf_i over the three i^{th} sites in (a), (b) and (c) of Figure 44 is almost zero and the same is true for tetrahedral sites. This means that ΔB_{hf} in the low strain region should be zero or very small. Hence if domains are randomly distributed among easy axes, there will be almost no change in frequency upon the application of external tensile stress. Since the tensile stress breaks the randomness of the domain distribution, the slight decrease of frequency in the low strain region is well understood.

e. (P_1-P_2) estimated for the muon in Fe from the experimental result

The estimate of values of (P_1-P_2) was made assuming that the $B_{hf,i}$'s are the same at sites of each octa-or tetrahedral symmetry. Such an assumption is supported by the fact that the local magnetization density measured by neutron scattering does not show any difference between sites of the same symmetry. This can be seen in Figure 42. With this assumption, $\partial \tilde{B}_{hf}/\partial \epsilon = 0$. Therefore, we get a simple equation

$$\frac{\partial B_\mu}{\partial \epsilon} = \sum_i \left\{ \frac{\partial B_{d,i}}{\partial \epsilon} f_i(\epsilon=0) + \frac{\partial f_i}{\partial \epsilon} B_{d,i}(\epsilon=0) \right\}$$

where, from the experiment, $\frac{\partial B_\mu}{\partial \epsilon} = 25.1$ G/100 μ strain.

Writing $f_1 = f_0(1 + c_1 \epsilon)$, we can easily obtain

$$c_1 = \frac{2}{B_{d1,0}} \left(\frac{\partial B_\mu}{\partial \epsilon} - \frac{1}{3} \frac{\partial}{\partial \epsilon} \sum_i B_{d,i} \right)$$

and

$$P_1 - P_2 = \frac{kT}{1.374 \epsilon_{100}} \ln \left[\frac{2(1 + c_1 \epsilon_{100})}{2 - c_1 \epsilon_{100}} \right]$$

For a point like muon (or with a short ranged spherical wave function) which does not produce a local lattice distortion around it,

$B_{dl,0}$ is calculated to be 18.64 kG for the octahedral site and -5.253 kG for the tetrahedral site. $\frac{\partial}{\partial \epsilon} \sum_i B_{d_i}$ is also calculated to be -11.9 G/100 μstrain and -5.4 G/100 μstrain for the octahedral site and the tetrahedral site, respectively. The (P_1-P_2) thus calculated are 0.85 eV for the octahedral site and -2.39 eV for the tetrahedral site.

Comparing these values of (P_1-P_2) with those given in the second column of the table in part d, the agreement seems to be better in the case of the tetrahedral site. Then does this mean that muons prefer to stop at tetrahedral sites in Fe? The answer is no. This is because without having the local distortion of the lattice around the muon (P_1-P_2) is indeed meaningless. If we simply assume that the muon displaces the neighboring atoms in Fe as it does in Nb, with the information given in Table 5(a), $B_{dl,0}$ can be calculated to be 13.563 kG and -3.726 kG for octa- and tetrahedral sites, respectively. Then (P_1-P_2) is 1.17 eV for the octahedral site and -3.42 eV for the tetrahedral site. Since the lattice parameter of Fe is smaller than that of Nb, the ratio u/a should be larger in Fe resulting in larger magnitudes of (P_1-P_2) in both cases. However, the further correction can be shown to be small. For example, if we take $u_{Fe} = U_{Nb} \times 3.3/2.87$, then $B_{dl,0}$ in the octahedral site becomes 12.99 kG which gives $(P_1-P_2) = 1.21$ eV.

Up to this point we have treated the muon wave function as spherically symmetric and very short ranged. Since the interstitial sites of BCC lattices possess tetragonal symmetry, the muon wave function is not likely to be spherical. For this reason, we chose a particular form of the muon wave function so that the probability density is

$$|\psi_\mu(\vec{r})|^2 = \frac{1}{\alpha^2\beta\pi^{3/2}} e^{-\frac{x^2+y^2}{\alpha^2}} e^{-\frac{z^2}{\beta^2}}$$

for a site with the tetragonal axis parallel to $\vec{M}_s = M_s\hat{Z}$ and calculated (see Appendix C)

$$\langle B_d \rangle = \int B_d(\vec{r})\, |\psi_\mu(\vec{r})|^2 d\vec{r}$$

Wave functions of the muon in Nb are shown in Figure 45 for both configurations.[55] By a visual comparison, the value of α was estimated to be about 0.19 for both configurations and β is expected to be close to $\alpha/\sqrt{2}$. Since we do not know the value of α in Fe, in the calculation α was varied from 0.15 to 0.25 for the 4T(0)-configuration and from 0.15 to 0.22 for the 1T-configuration. The functional form of

$$\psi_\mu(x) = e^{-x^2/2\alpha^2}$$

is shown in Figure 46 for several values of α.

Figure 47 and Figure 48 show the results of the calculation of $B_{dl,0}$ in the 4T(0) and 1T-configuration, respectively. Similar calculations were performed on Bd_1 and Bd_2 with $\epsilon_{100} = 100 \times 10^{-6}$ for both configurations. The calculated results of $\frac{1}{3}\frac{\partial}{\partial\epsilon}\sum_i B_{d_i}$ are plotted in the next two figures.

Figure 51 shows the result of (P_1-P_2) for the 4T(0) configuration. Two curves are drawn for $\alpha = \beta$ and $\alpha = \sqrt{2}\,\beta$. Because of the tetragonal symmetry of interstitial sites we consider the values of (P_1-P_2) along $\alpha = \sqrt{2}\,\beta$ as more realistic. If we assume $\alpha = 0.2$ for Fe, (P_1-P_2) should be about 1.8 eV. On the other hand, from the result for the 1T-configuration, shown in Figure 52, (P_1-P_2) should be close to -6.0 eV for $\alpha = 0.2$.

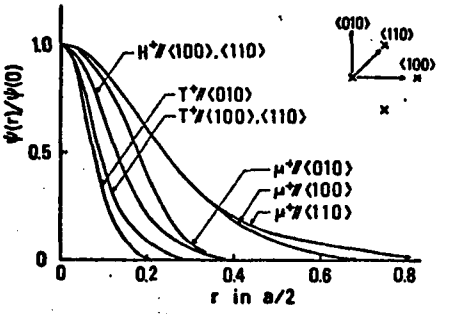

Fig. 45(a). Ground-state wave functions of a proton, a triton, and a positive muon in the 1T configuration in Nb. Variation of the amplitude in some principal directions on the (001) plane is shown.

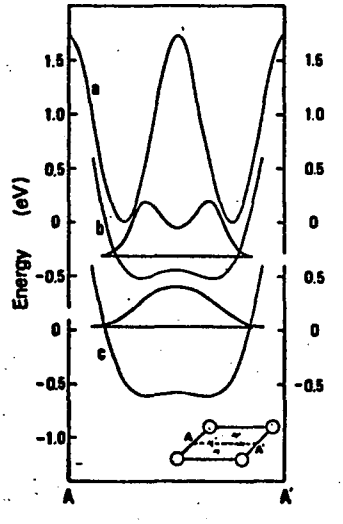

Fig. 45(b). Potential profiles and ground-state wave functions of a proton and a positive muon in the 4T configuration in Nb. Variation along the line AA' in the inset is shown.
(a) Potential profile in the undistorted lattice, (b) proton, and (c) muon.

$$\psi_\mu(x) = e^{-x^2/2\alpha^2}$$

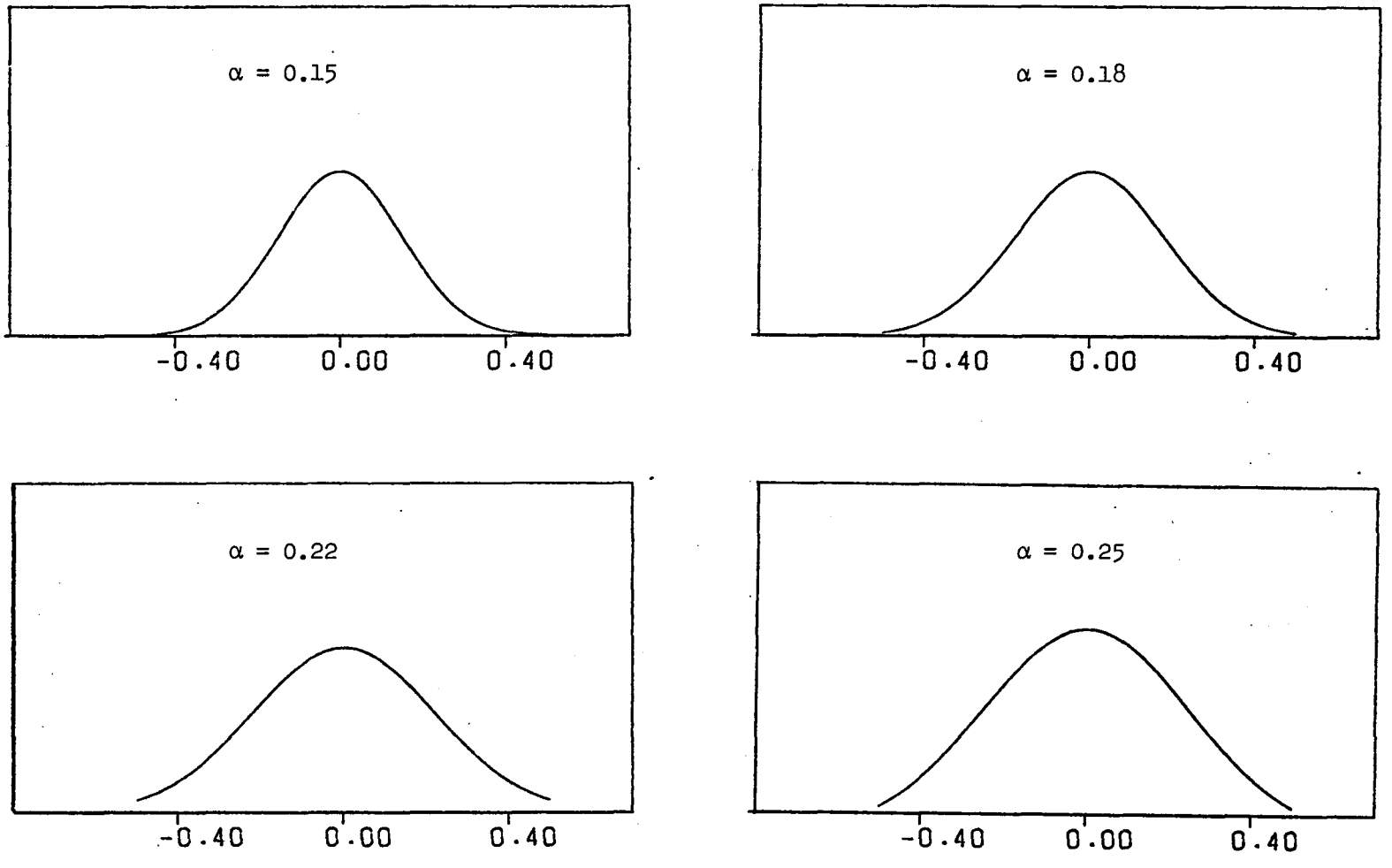

Fig. 46. The functional form of the one dimensional Gaussian type wave function. The horizontal axes are drawn in units of the lattice parameter.

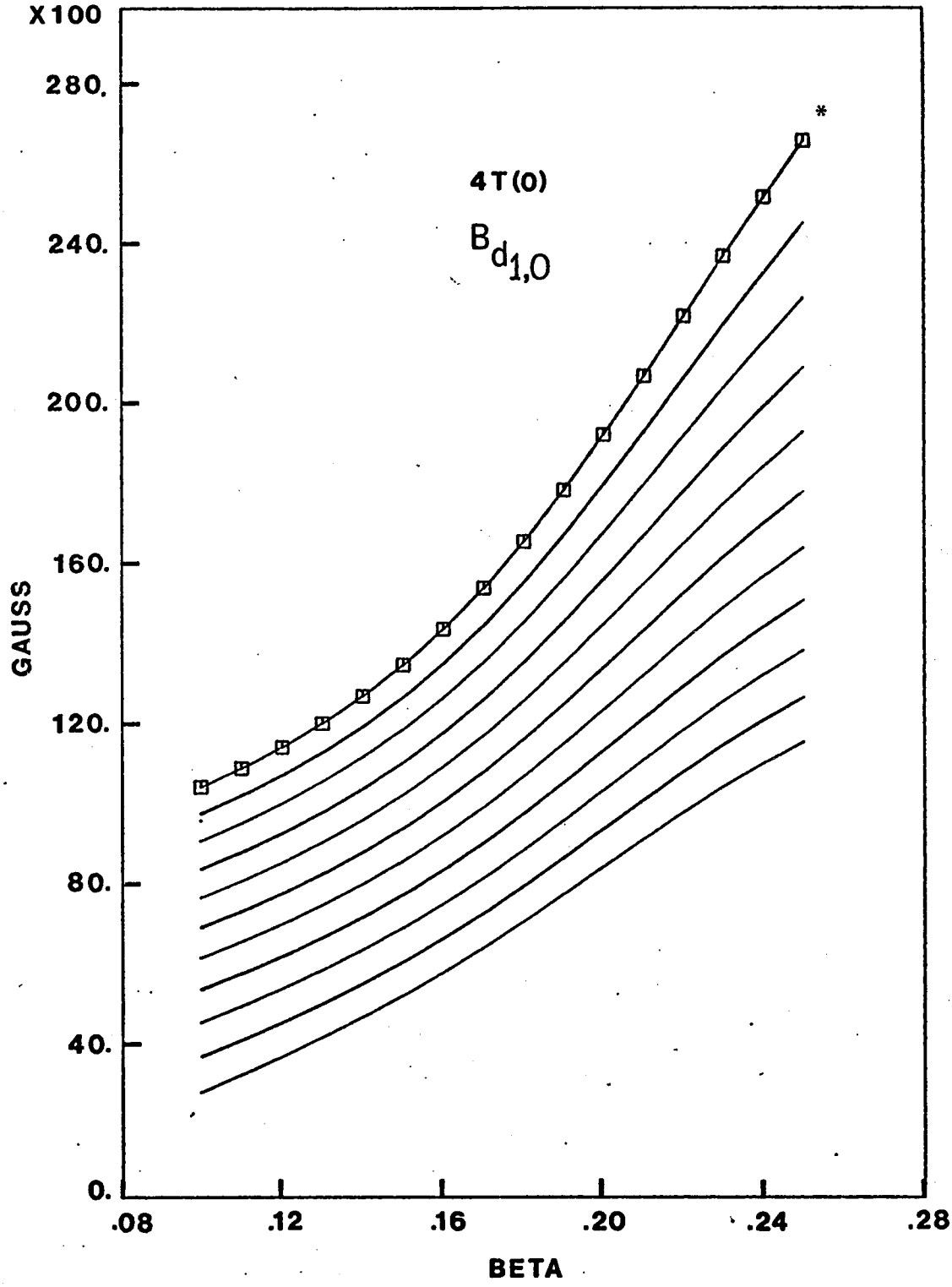

Fig. 47. * The curve with square symbols is for $\alpha = 0.15$. Subsequent curves are drawn with increasing α by 0.01. The next five figures are drawn in the same way.

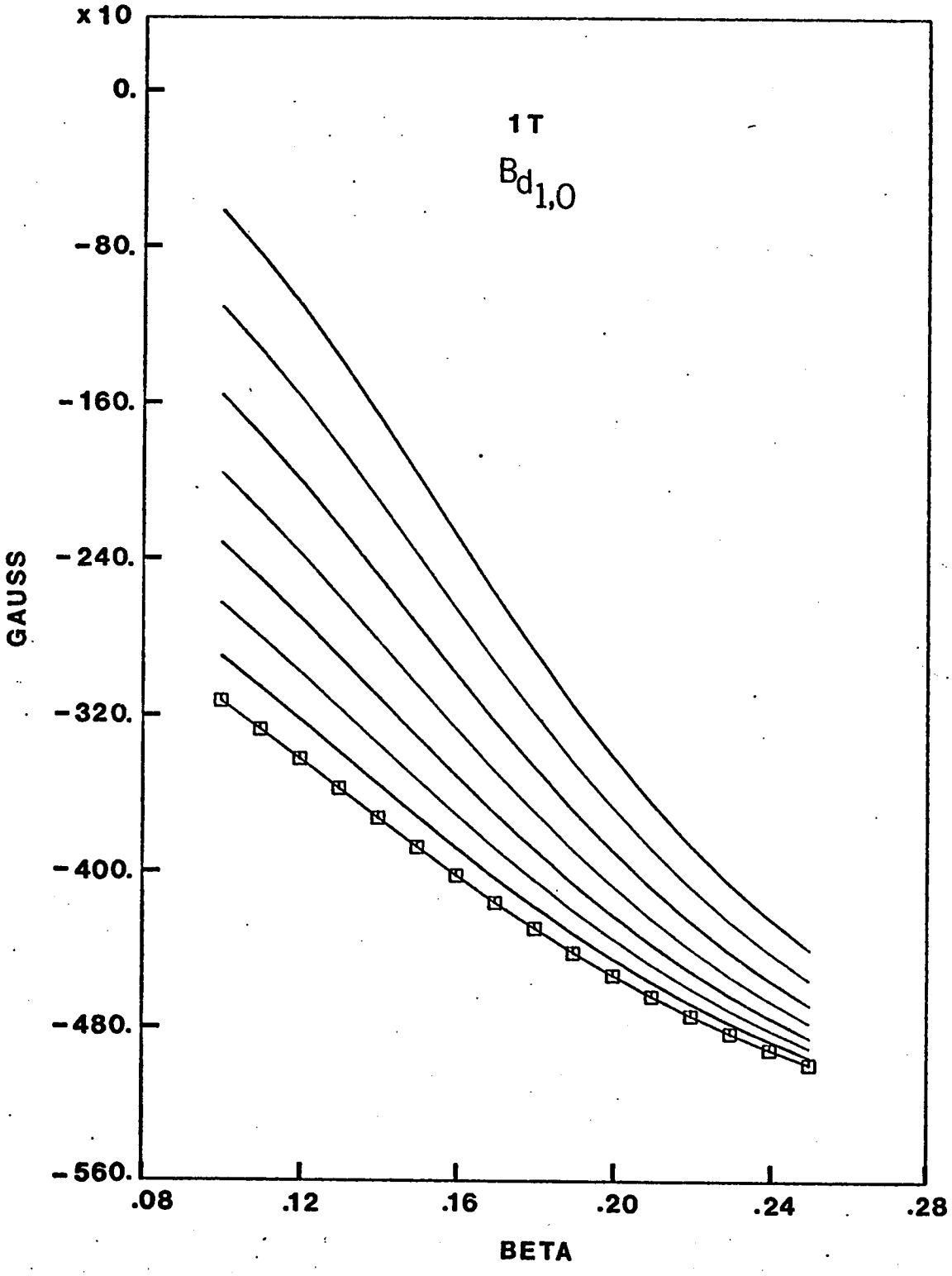
x 10
0.
1T
$B_{d_{1,0}}$
-80.
-160.
-240.
-320.
-400.
-480.
-560.
GAUSS
.08
.12
.16
.20
.24
.28
BETA

Fig. 48

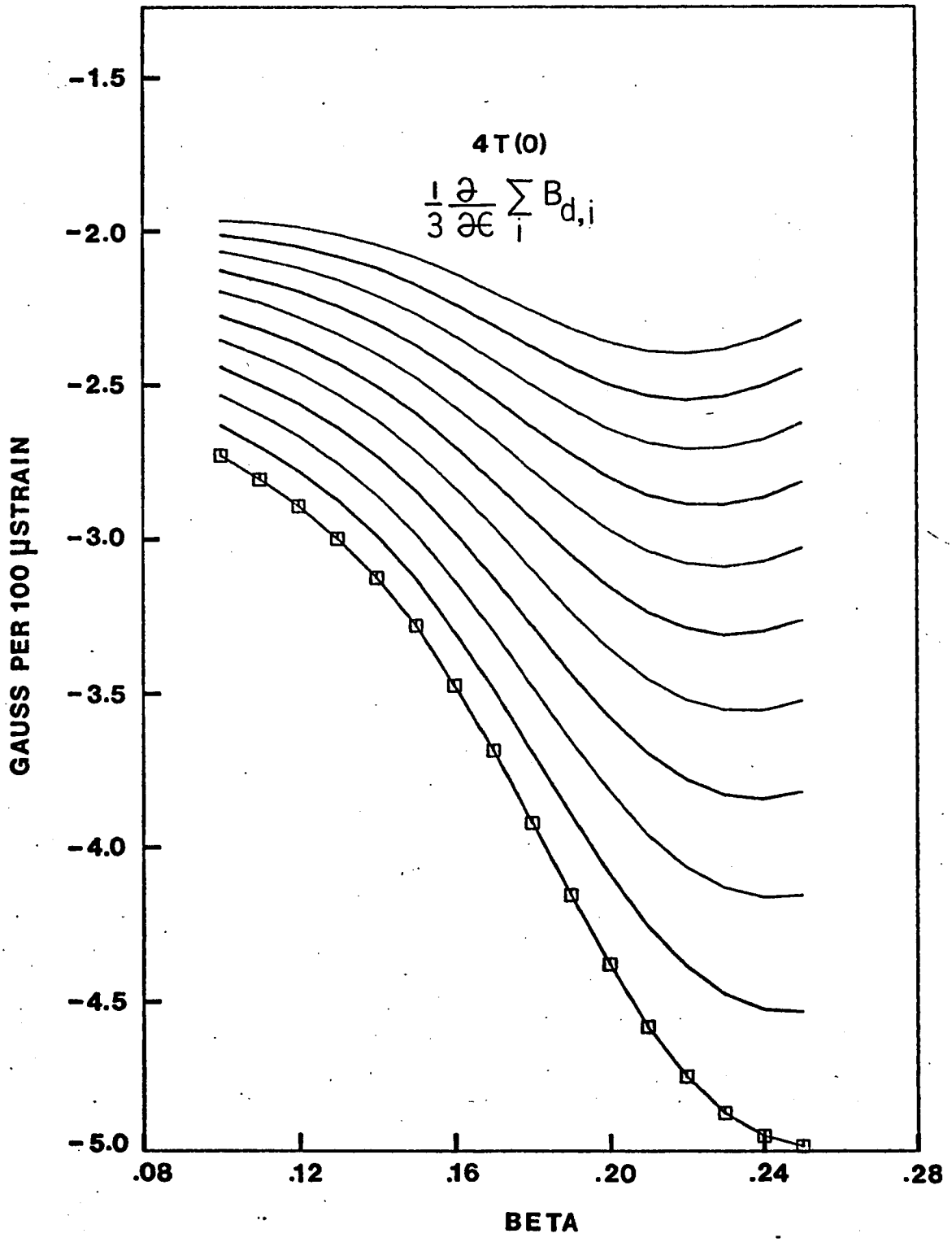
4 T (0)
$\frac{1}{3}\frac{\partial}{\partial \epsilon}\sum_i B_{d,i}$
-1.5
-2.0
-2.5
-3.0
-3.5
-4.0
-4.5
-5.0
GAUSS PER 100 μSTRAIN
.08
.12
.16
.20
.24
.28
BETA

Fig. 49

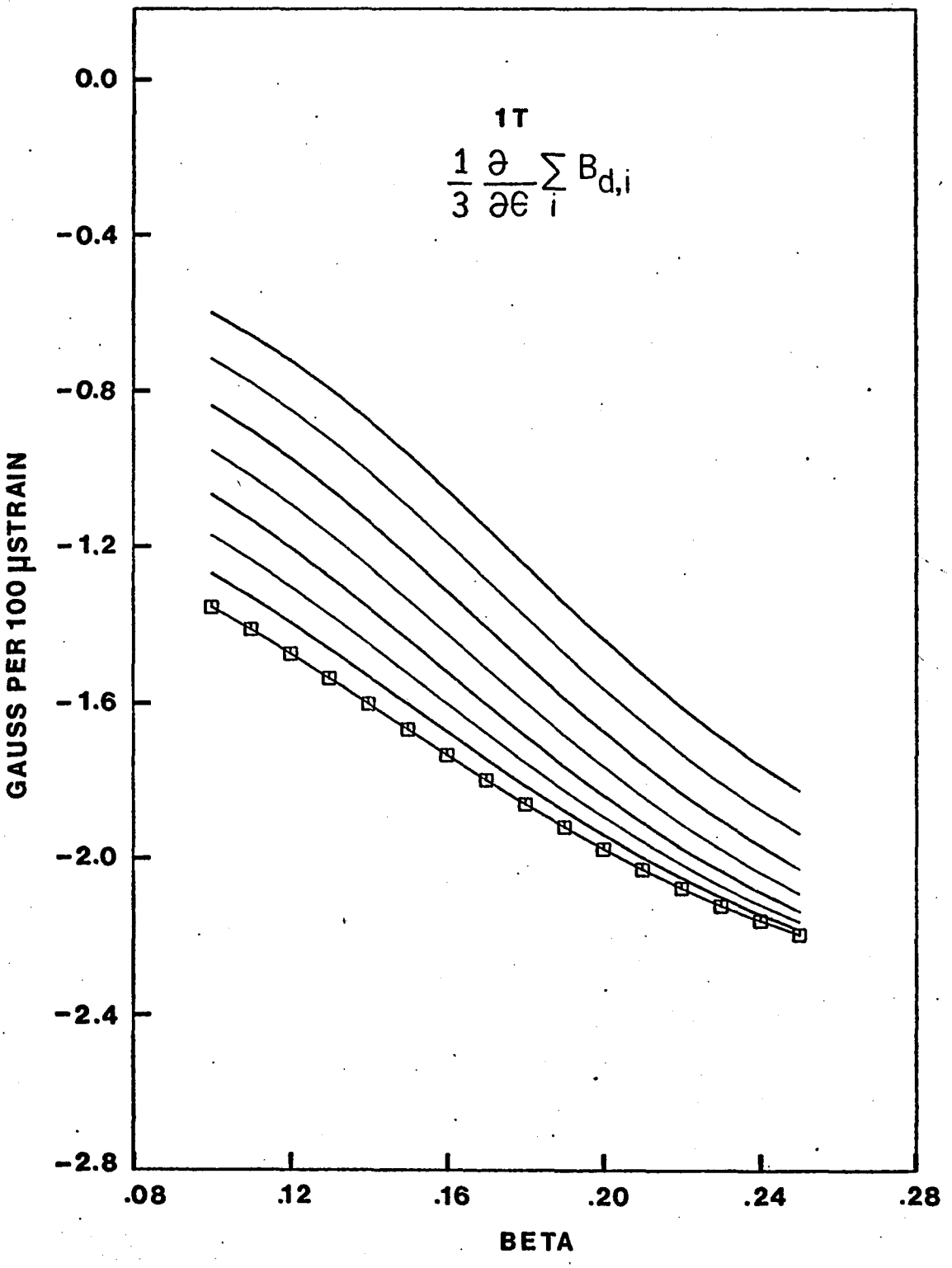
1T
$\frac{1}{3}\frac{\partial}{\partial \epsilon}\sum_i B_{d,i}$
0.0
-0.4
-0.8
-1.2
-1.6
-2.0
-2.4
-2.8
GAUSS PER 100 μSTRAIN
.08
.12
.16
.20
.24
.28
BETA

Fig. 50

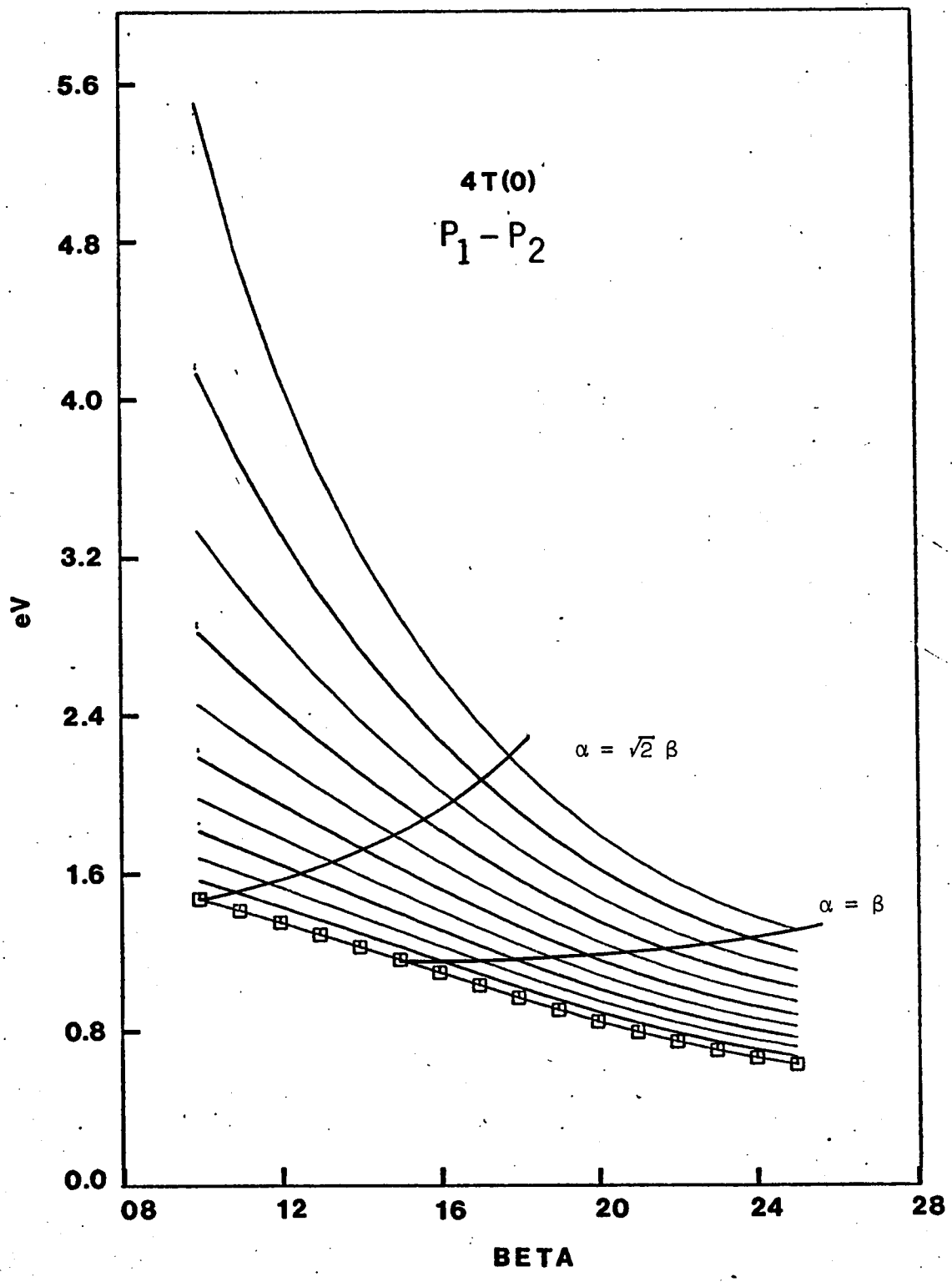
4T(0)
$P_1 - P_2$
5.6
4.8
4.0
3.2
2.4
1.6
0.8
0.0
eV
$\alpha = \sqrt{2}\,\beta$
$\alpha = \beta$
08
12
16
20
24
28
BETA

Fig. 51

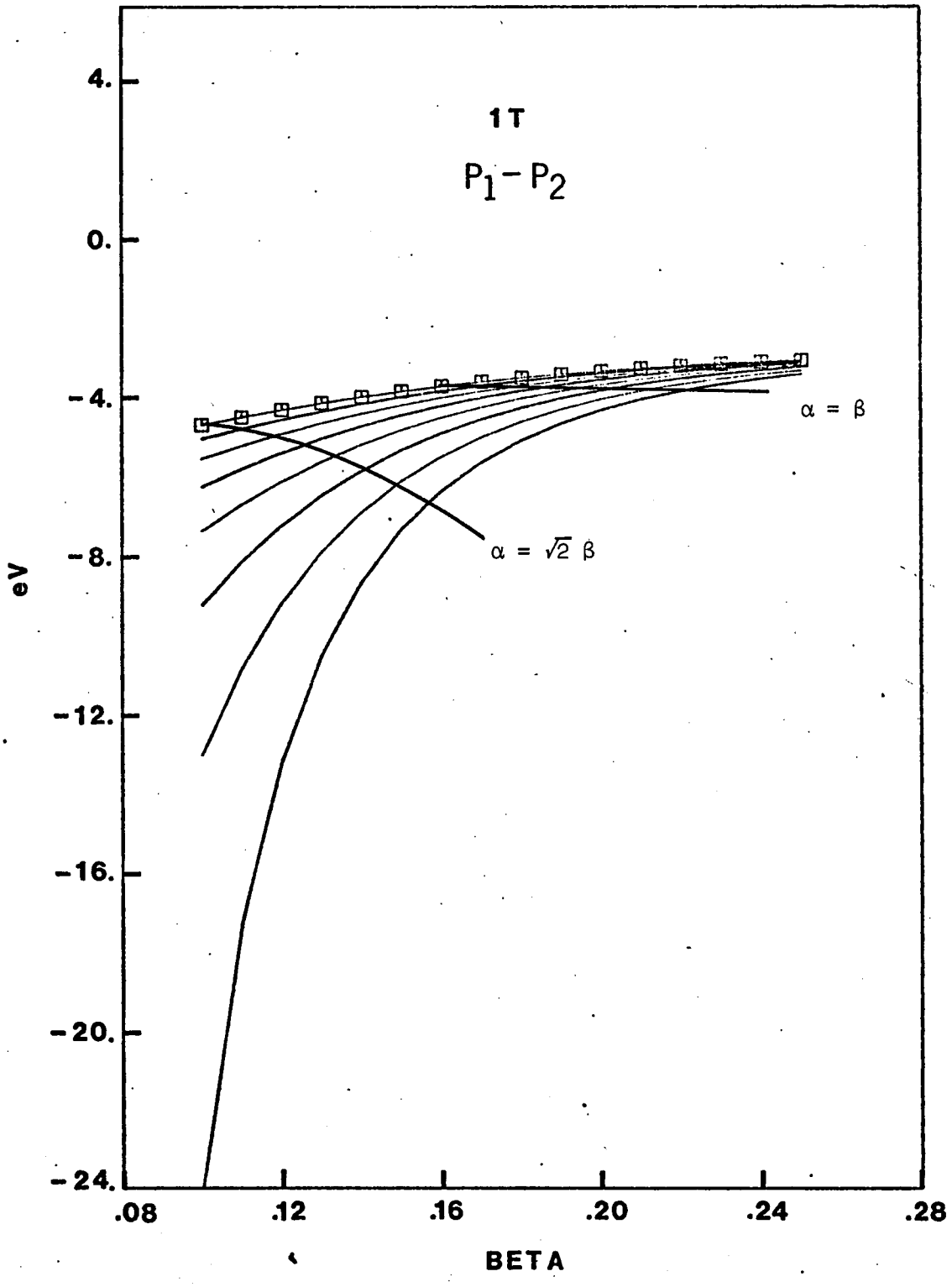
1T
$P_1 - P_2$
4.
0.
-4.
-8.
-12.
-16.
-20.
-24.
eV
.08
.12
.16
.20
.24
.28
BETA
$\alpha = \beta$
$\alpha = \sqrt{2}\,\beta$

Fig. 52

Previously, we estimated values of (P_1-P_2) for Nb with the lattice parameter of 2.87 A°. These are 3.73 eV and -1.23 eV for the 4T(0) and 1T-configuration, respectively. Comparing these with values estimated from the experimental results, we see that the agreement is much better in the 4T(0)-configuration. Furthermore, if we include the correction for U/a for Fe, the magnitude of (P_1-P_2) will increase by about 0.05 eV in each case. From this we conclude that the muon should have the 4T(0) occupational configuration in Fe.

As discussed by Sugimoto et al.,[55] lighter interstitial isotopes appear to be larger in size and the preferred occupation in a BCC crystal is the 4T(0)-configuration. Such a trend is verified in their calculation by showing that in Nb the more stable configuration is 1T for hydrogen, while it is 4T(0) for the muon. Also, the reduction of the lattice parameter always tends to stabilize the 4T(0)-configuration in a BCC crystal. Therefore, the stable site of a muon in Fe should probably be the 4T(0)-configuration.

The above discussion is also consistent with the calculated result of Johnson et al.,[56] who showed that large sized interstitials, C, O, N, occupy the octahedral sites of Fe and V by drastically lowering the potential energy with outward displacements of the two nearest-neighbor atoms.

f. Further discussion on (P_1-P_2)

We now turn our attention to possible corrections to the value of (P_1-P_2) obtained from the experimental result. The first thing to be considered is the calculation of $B_{d1,0}$ or B_{d1}. In the calculation we

assumed that the dipole moments are not affected by the presence of the muon but this probably is not true. The direction of the magnetic moment of atoms close to the muon may deviate from the direction of the domain magnetization. This would be especially so for the nearest-neighbor atoms around the tetrahedral site.

The Z-component of the dipolar field at the tetrahedral site due to the four nearest neighbor atoms should be reduced if the direction of their magnetic moments deviates from the Z-axis. Since the contribution of the four nearest atoms to $B_{dl,0}$ at the tetrahedral site is -8.92 kG (96% of the total magnitude), the decrease in $B_{dl,0}$ can be significant. If this is so, the magnitude of (P_1-P_2) calculated should be even larger than 6.0 in the 1T-configuration. Figure 53 (a) shows the deviation of the nearest neighbor moments from the Z-axis in the case of the 1T-configuration and (b) shows that there is no deviation for those around the octahedral site.

The next thing to be considered is another assumption we made in the dipolar field calculation. We assumed that each atom carries the same effective number of Bohr magnetons. As pointed out by Stronach et al.,[57] either the free itinerant electrons or the localized electrons can contribute to B_{hf} in Fe. If we assume that B_{hf} arises mainly from the localized electrons belonging to the nearest neighbor ions, we can no longer consider the effective number of Bohr magnetons carried by these ions to be the same as that for an ion located far from the muon. Then the contribution to the dipolar field by the nearest neighbor ions would decrease and it will subsequently increase the magnitude of (P_1-P_2) in both configurations.

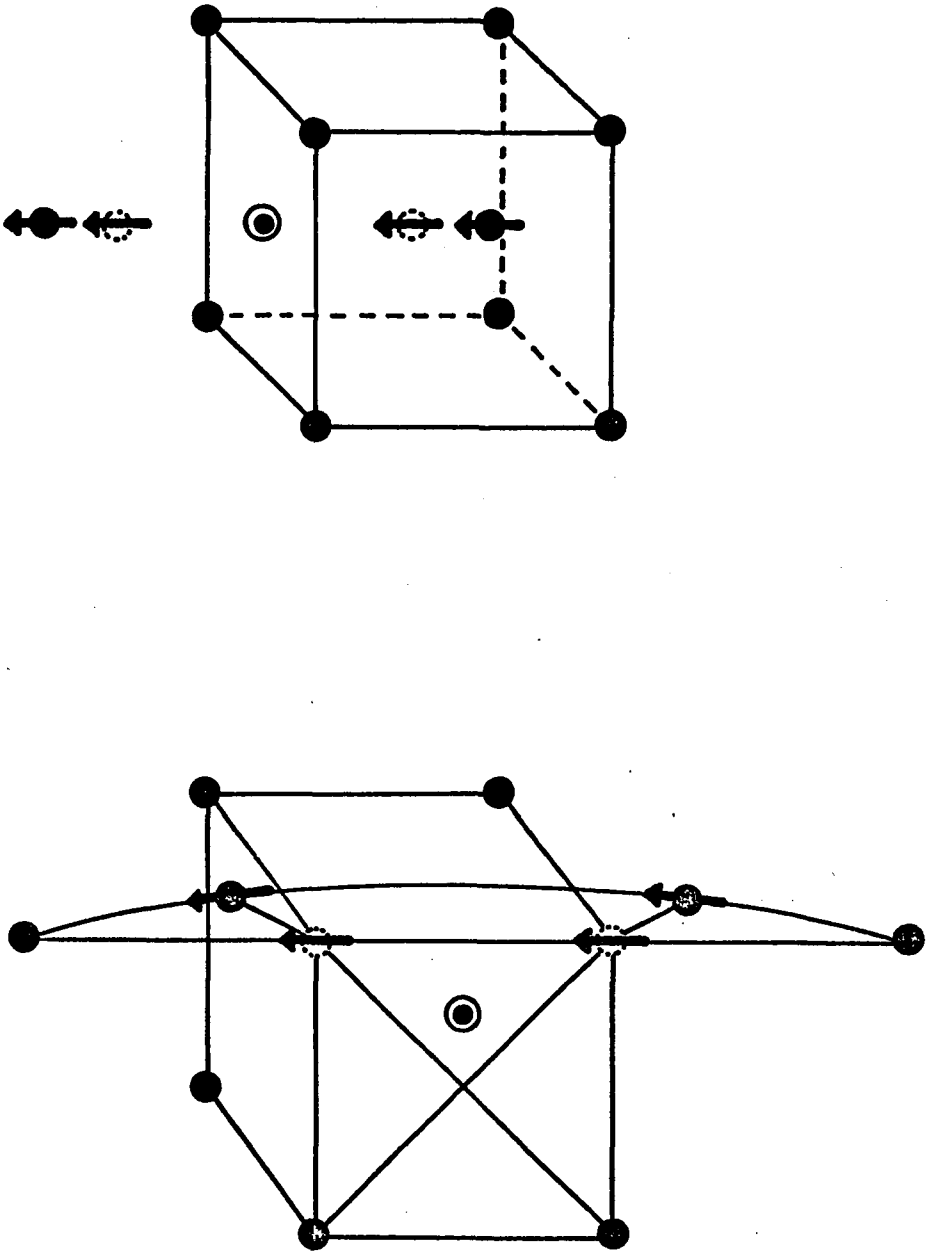

Fig. 53. The presence of a muon at a tetrahedral site can deviate magnetic moments of nearest neighbor atoms from the domain magnetization direction, (a), while it may not happen with a muon at an octahedral site, (b).

These factors reinforce our claim that the 1T-configuration is not correct for the muon occupation in Fe.

There are some other corrections we can think of. For example, we assumed that the probability of muon occupation at each site is the same when the sample is unstrained but this is not true. As experimentally verified by De Vries et al.,[58] interstitial carbon atoms prefer to occupy octahedral sites with tetragonal axes perpendicular to the domain magnetization direction. We can think that this is the same for the muon in Fe but the correction to the result for (P_1-P_2) is negligible. We may also assume that the hyperfine field is not the same at octa- or tetrahedral sites with different orientations of the tetragonal axis. However, due to lack of information we will not discuss it further.

C. Other Results

After the four steps of the experiment already described, the Fe <100> sample was put in a vise and was pressed to induce a permanent deformation on a small portion of its wide face. By pressing on one face, the sample was bent and when the external tensile stress was applied one face was under tension while the other one was under compression. Results from this experiment are shown in Table 6. Since the sample was bent (permanently), its shape before the application of external stress was not recovered by releasing the stress. Therefore, the comparison between the stressed and the released state is not obvious. A few points will be mentioned instead of giving rigorous interpretations:

1) To obtain values of χ^2 very close to unity, the transverse relaxation term e^{-t/T_2} in the fitting equation had to be replaced by $e^{-\sigma^2 t^2}$. This indicates that the motion of a muon was restricted to a certain small region in the crystal.

Table 6. Face 1 was under tension and face 2 was under compression by the application of an external tensile stress.

Face	Frequency (MHz)	F_T/F_L	Weight (kg)	State
1	48.196 ±0.0424	2.70	0.0	
	47.595 ±0.0565	2.36	9.84	S*
	48.396 ±0.0740	1.58		R
	47.944 ±0.0242	4.49	5.98	S
	48.143 ±0.0584	1.35		R
2	47.946 ±0.0769	1.04	0.0	**
	47.942 ±0.0735			
	47.892 ±0.079		5.98	S
	47.943 ±0.094			R

*S and R indicate the stressed and released states, respectively

**performed under the same condition

2) With a few exceptions the frequency in face 2 stayed around 47.94 MHz, which is close to the 47.9 MHz measured in a rolled Fe sample as reported by Arrott et al.

3) F_T/F_L and λ_L were not obtained in later experiments on face 2, indicating a pure transverse relaxation.

Inducing a permanent deformation in a crystal is known to increase dislocations and more unit cells were distorted in this experiment. It is not clear what is the origin of the effect restricting the motion of a muon in this case. Generally, it is assumed that an impurity atom is repelled from the compressed region above an edge dislocation while it is attracted by the extended region below the dislocation. If this is true it is possible that muons were trapped in the extended region of the crystal.

Since the distortion of unit cells around a dislocation is not uniform, it is necessary to see the effect of arbitrary distortion of unit cells on the frequency. For this we applied an external tensile stress to the Fe-polycrystal sample. Results from two separate measurements are presented in Figure 54. Because of the small collimator used in this experiment and the large average grain size of this sample it is possible that muons might have been stopped in a few grains oriented close to the stress axis. To exclude such a possibility, this result was compared with the result from a very similar sample using a larger sized collimator.

As seen in Figure 54 results from these two experiments show almost the same pattern except the downward shift of the points in the

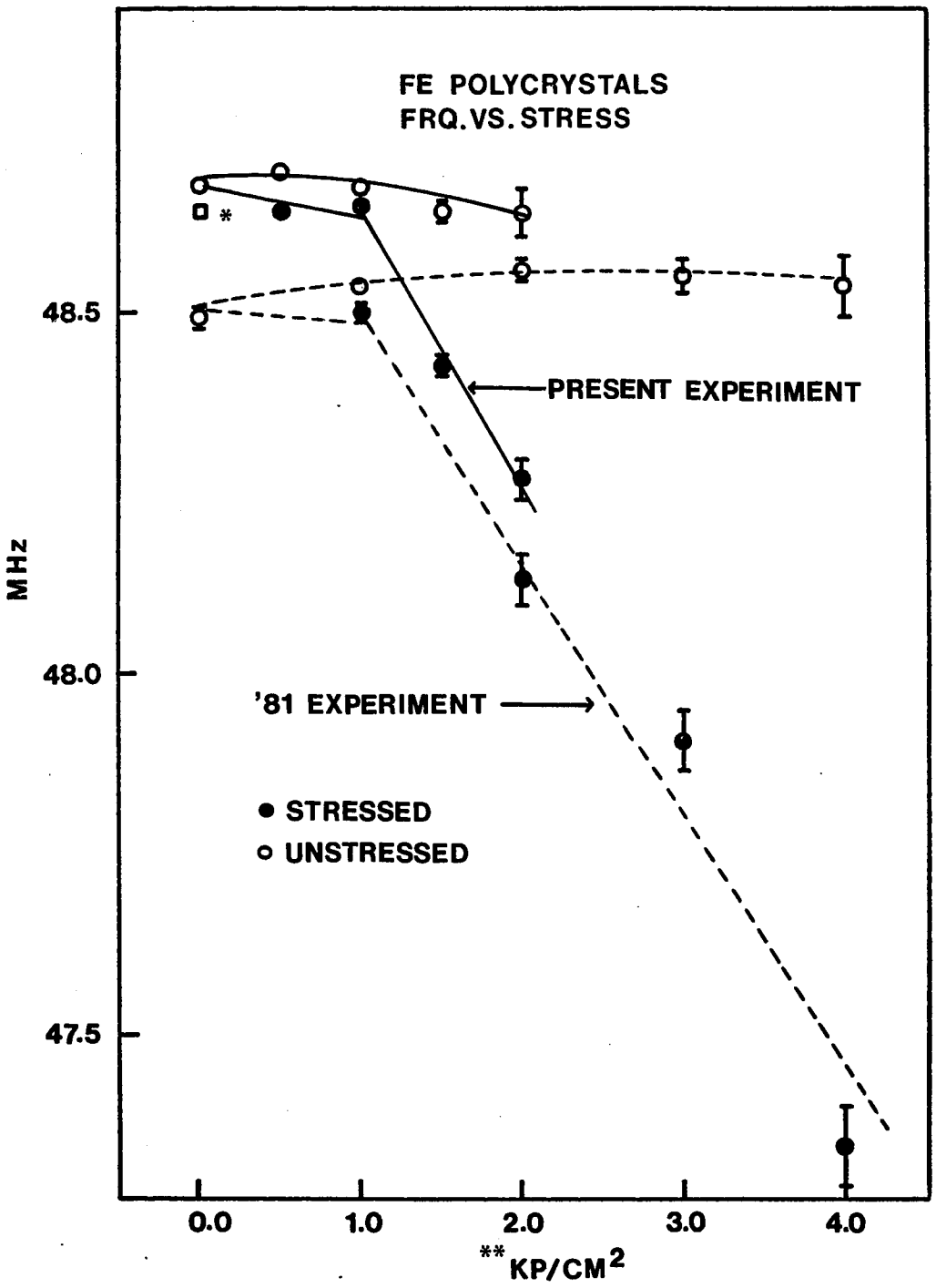

Fig. 54. * "in air" measurement of 1981 experiment
** 1 kp/cm^2 of air pressure corresponds to 3685 psi on the samples

old result. This shift is easily explained by the fact that in the old experiment the sample was clamped to sample holders which were held together by screws and it caused a tension on the sample surfaces. The change in frequency in these polycrystalline samples exactly resembles that in the Fe ⟨100⟩ sample.

The elastic dipole model certainly explains the frequency drop in polycrystalline samples. This is illustrated in Figure 55. Here, for simplicity, it is assumed that the stress is homogeneous in the sample which means any odd effect by grain boundaries upon transmission of the stress is not counted.

From the concept of magnetostriction it is true that if a unit cell is elongated along a direction of crystal axes by 22×10^{-6}, the magnetization of each atom should point the same direction. If the strain in a unit cell is not along a crystal axis the magnetization will align along the crystal axes closest to the strain axis. In fact the stress within a certain region around a dislocation is strong enough to distort unit cells so that the local magnetization deviated from the domain magnetization direction to follow the local distortion.

Therefore, with the argument used to explain the frequency drop in the polycrystal by an external tensile stress, the decrease in frequency in the region around a dislocation can be explained.

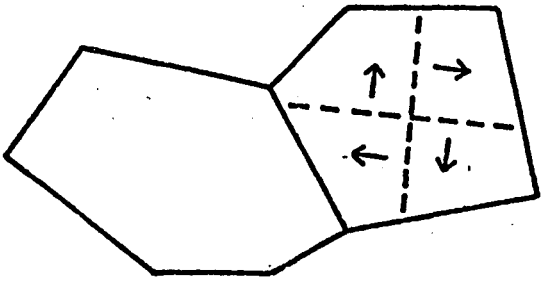

(a)

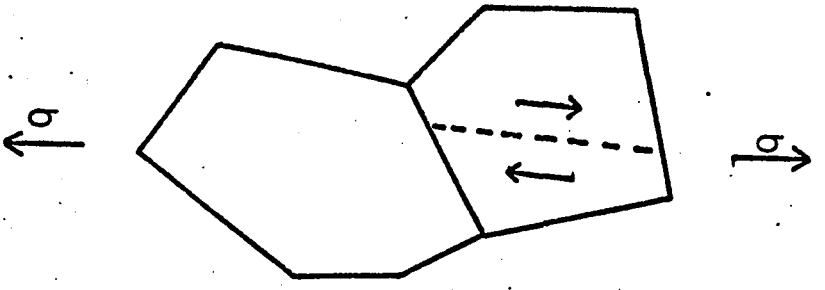

(b)

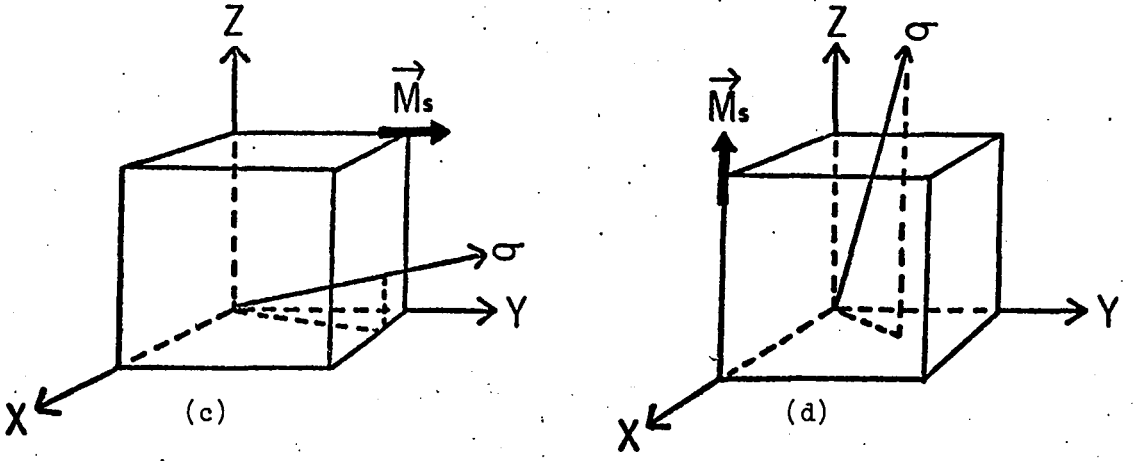

Fig. 55. Schematic illustration of domain alignment in a grain of an Fe polycrystal specimen due to external tensile stress. (a) is a typical case prior to application of stress, (b) shows alignment under stress, (c) and (d) represent two different possible orientations of the magnetization relative to the stress axis.

VI. SUMMARY AND CONCLUSIONS

A. Summary

In this experiment we observed the shift in B_μ upon externally applied uniaxial stress. This change in B_μ can arise from changes in the average field due to the localized dipoles on the Fe atoms and from changes in the hyperfine field. Since the strain dependence of the dipolar sum depends upon the muon site we have been able to provide evidence for a 4T(0) site preference.

We have found that $\partial B_\mu / \partial \epsilon$ is dominated by site occupancy change. Assuming that the hyperfine field is the same for crystallographically equivalent sites, using the best estimates we could make for lattice relaxation, and muon wave function extension and oblateness, we obtained the muon lattice double force tensor components P_1-P_2 or equivalently the free energy difference between magnetically inequivalent sites.

The F_T/F_L ratio is a measure of the domain alignment. We have observed that for external fields greater than 125 G the internal domains align. This is in agreement with bulk magnetization measurements on the sample. With the application of tensile stress along a crystal axis of Fe after the external field had been turned off we again observed domain alignment at approximately 1/8 of the elastic limit which, as far as we know, is the first time stress induced domain alignment internal to a

sample has been observed. These same effects were also observed in the frequency shift, for with randomly distributed domains one expects the average shift to be zero and it is until F_T/F_L becomes large.

We also applied tensile stress to polycrystalline Fe samples and obtained results similar to those for the single crystal. Combining these results, we were able to explain why local strains tend to decrease the muon frequency, i.e., the magnitude of B_μ , in Fe.

B. Future Perspective

The present experiment was performed at room temperature only and the shift in B_μ was explained by a site occupancy shift of the muon. To check the validity of this model, it is necessary to perform experiments at different temperatures. To see the effect of changing temperature, let's consider the following:

$$\frac{\partial B_\mu}{\partial \epsilon_{100}} \epsilon_{100} \cong \sum_i \frac{\partial f_i}{\partial \epsilon_{100}} B_{di,0}\, \epsilon_{100}$$

$$= \frac{z}{q} \left(B_{d1,0} - B_{d2,0}\right) \Delta g / kT$$

where

$$\Delta g = -1.374 \left(P_1 - P_2\right) \epsilon_{100}$$

Therefore, not even counting the increase of $B_{di,0}$ with decreasing temperature, we should get a $\partial B_\mu / \partial \epsilon$ twice as great at T = 150 K than at room temperature. With the change of $B_{di,0}$ it will be even greater.

To explain some peculiar results obtained for λ_T and λ_L, especially for the increase of λ_T upon the external field, we proposed a field inhomogeneity contribution due to surface irregularities of the

sample. Therefore, a suggestion from the present experimental results is to use samples with very smooth surfaces and a muon beam which would be stopped closer to the center of the slab samples.

APPENDIX A

The Depolarization of Muon Spins in Solids

The initial spin polarization of muons starts relaxing as soon as the muons are stopped in a solid. As mentioned in Chapter 1, there are two different mechanisms, namely, longitudinal and transverse relaxations. The time dependences of these relaxations provide the information on the behaviors of muons in solids.

The longitudinal relaxation process always involves an exchange of energy between the system of muon spins and its surrounding, which is the lattice. The time dependence of this process can easily be shown to be exponential and it will not be discussed here.

On the other hand, the transverse relaxation, which does not alter the energy of the spin system, originates from the local field inhomogeneity in the solid. The time dependence of this process is often either exponential or Gaussian, i.e.,

$$P(t) = P(0)\, e^{-\Gamma t} \tag{A-1}$$

for the exponential depolarization, and

$$P(t) = P(0)\, e^{-\sigma^2 t^2} \tag{A-2}$$

for the Gaussian depolarization. The physical origin of this process is the fact that the muon precession frequency is distributed with a finite width which causes the vector sum of muon spins to decrease as time elapses.

If the muons execute random jumping motion among their sites, the width of the frequency distribution will be reduced, i.e., motionally narrowed. With very fast jumping motions of muons, the relaxation can be shown to be exponential. Conversely, if the motions are slow or the muons are immobile, the relaxation will be approximately Gaussian. In this appendix we will discuss the physical nature of the relaxation processes.

a. The Ensemble Average of An Observable

Suppose we have a system which can be characterized by a wave function $\phi(\vec{r}_1, \vec{r}_2, \cdots \vec{r}_N, t) = \sum_k C_k(t) \phi_k(\vec{r}_1 \cdots \vec{r}_N)$. The probability that the system will be in a given state at a later time t' is proportional to the number of times it passes that state in time. However, instead of thinking of the system at different times, we can just as well think of identical (in different states) systems at the same time. Thus, instead of averaging over time, we can average over the ensemble. Then

$$\mathcal{L}^n = \int \phi^n(t)^* \, \mathcal{L} \, \phi^n(t) \, d\tau$$

where $\mathcal{L}$ is the physical quantity of interest, $\phi^n(t)$ is the wave function of the nth system and $dt \equiv d\vec{r}_1 d\vec{r}_2 \ldots d\vec{r}_N$. The ensemble average of is shown to be

$$\begin{aligned} \langle \mathcal{L} \rangle &= \frac{1}{N} \sum_n \mathcal{L}^n \\ &= \sum_{k'k} \rho_{k'k} \mathcal{L}_{kk'} = Tr \, \rho \mathcal{L} \end{aligned} \tag{A-3}$$

where

$$\mathcal{L}_{kk'} = \int \phi_k^* \mathcal{L} \phi_{k'} \, d\tau$$

and $$\rho_{kk'} \equiv \frac{1}{N} \sum_{n} C_k^{n*}(t)\, C_{k'}^{n}(t)$$

which defines the density matrix. One can immediately notice that, for the above treatment, we used the Schrödinger picture by assigning an explicit time dependence to the wave function.

However, for our present purpose, we may want to describe the evolution of an observerable in time from an initial state. To do this we will use the Heisenberg picture. Since the two pictures are eventually the same, we can use the results in equation (3) but the expression of the density matrix will have a different form.

The density operator expressing the initial state of the ensemble is given by

$$\rho = \sum_{i=1}^{N} P_i \, |\chi_i\rangle\langle\chi_i| \qquad \text{(A-4)}$$

where P_i is the probability that the system will be found in the state of $|\chi_i\rangle$ and the $|\alpha_i\rangle$'s are the basis vectors. The time evolution of $\mathcal{L}(t)$ is written as

$$\mathcal{L}(t) = e^{iHt/\hbar}\, \mathcal{L}(0)\, e^{-iHt/\hbar}$$

where H is the Hamiltonian of the system. Then

$$\begin{aligned} \langle \mathcal{L}(t) \rangle &= Tr\, \rho \mathcal{L}(t) \\ &= Tr \left(\sum_{i=1}^{N} P_i |\chi_i\rangle\langle\chi_i| \mathcal{L}(t) \right) \qquad \text{(A-5)} \\ &= \sum_{i=1}^{N} P_i \langle\chi_i| e^{iHt/\hbar}\, \mathcal{L}(0)\, e^{-iHt/\hbar} |\chi_i\rangle \end{aligned}$$

b. The Depolarization of Muon Spins

A muon implanted in a solid interacts with a large number of localized magnetic dipoles. The interaction between the muon and a localized dipole with its magnetic moment $\gamma_I \hbar \vec{I}$,

$$H_{\mu I} = \frac{\gamma_\mu \gamma_I \hbar^2}{r^3} \left(\vec{S}_\mu \cdot \vec{I} - \frac{3 (\vec{S}_\mu \cdot \vec{r})(\vec{I} \cdot \vec{r})}{r^2} \right)$$

can be rewritten, in a polar coordinate,[45] as

$$H_{\mu I} = \frac{\hbar^2 \gamma_\mu \gamma_I}{r^3} (A + B + C + D + E + F)$$

where

$$A = I_z S_{\mu z} (1 - 3\cos^2\theta)$$

with θ the angle between the radius vector r and the Z-axis. All other terms except A have operators which alter the spin state of the system and will be excluded. Then the Hamiltonian representing the interaction between a muon and the N localized dipoles will be

$$\mathcal{H}_D = \sum_{j=1}^{N} \alpha_j S_\mu^z I_j^z \qquad \text{(A-6)}$$

where

$$\alpha_j = \frac{\hbar^2}{r_j^3} \gamma_N \gamma_I (1 - 3\cos^2\theta_j) \qquad \text{(A-7)}$$

Following the general treatment given in part a, the density operator representing the initial spin ensemble can be written as

$$\rho = \sum_n C_n |n\rangle\langle n|$$

where

$$|n\rangle = |\psi_\mu^i\rangle |m_1\rangle |m_2\rangle \cdots\cdots |m_N\rangle$$

which span a $2(2I+1)^N$ dimensional space,

$$|\psi_\mu^{1,2}\rangle = \frac{1}{\sqrt{2}} \left(|+\rangle_\mu \pm |-\rangle_\mu \right)$$

and $|m_i\rangle$ describes the spin state of the ith localized moment. Then the ensemble average of the x-component of a muon spin will be

$$\begin{aligned} \langle \sigma_\mu^x(t) \rangle &= Tr\,(\rho \sigma_\mu^x(t)) \\ &= \sum_n C_n \langle n | e^{iH_D t/\hbar} \sigma_\mu^x e^{-iH_D t/\hbar} | n \rangle \end{aligned} \tag{A-8}$$

Since we have only one initial muon spin state, say $|\psi_\mu^1\rangle$, C_n must be $(2I+1)^{-N}$. Due to the motion of the muon, θ_j in equation (A-7) changes in time and subsequently equation (A-8) becomes

$$\langle \sigma_\mu^x(t) \rangle = \frac{1}{(2I+1)^N} \sum_n \langle n | e^{\frac{i}{\hbar}\int_0^t dt' \mathcal{H}_D(t')} \sigma_\mu^x \; e^{-\frac{i}{\hbar}\int_0^t dt' \mathcal{H}_D(t')} | n \rangle \tag{A-9}$$

The Hamiltonian $\mathcal{H}_D$ is now a stochastic function of time.

To evaluate the diagonal matrix elements in equation (A-9), we write the exponential term as

$$e^{-\frac{i}{\hbar}\int_0^t dt' \mathcal{H}_D(t')} = e^{-i\sum_{j=1}^N a_j(t) S_\mu^z I_j^z}$$

In the adiabatic approximation, $a_j(t)$ can be shown to be

$$\begin{aligned} [a_j(t)]^2 &= \gamma_\mu^2 \gamma_x^2 \hbar^2 \int_0^t \int_0^t \langle \alpha_j(t') \alpha_j(t'') \rangle \, dt' \, dt'' \\ &= 2\gamma_\mu^2 \gamma_x^2 \hbar^2 \int_0^t (t-\tau) \langle \alpha_j(\tau) \alpha_j(0) \rangle \, d\tau \\ &= 2\gamma_\mu^2 \gamma_x^2 \hbar^2 \int_0^t (t-\tau) \, g(\tau) \, d\tau \end{aligned}$$

where $\tau = t' - t''$ and $g(\tau) = \langle \alpha_j(\tau)\alpha_j(0)\rangle_t$ is the correlation function.

Here we assumed that

$$\langle \alpha_j(t')\alpha_j(t'')\rangle_t = \langle \alpha_j(t'-t'')\alpha_j(0)\rangle_t$$

Then

$$\sum_n \langle n | e^{i\sum_j a_j(t) S_\mu^z I_j^z} \sigma_\mu^x e^{-i\sum_\ell a_\ell(t) S_\mu^z I_\ell^z} | n\rangle$$

$$= \sum_n \frac{1}{2}\left(e^{i\sum_{j=1}^N a_j(t) m_j} + e^{-i\sum_{\ell=1}^N a_\ell(t) m_\ell}\right) \qquad \text{(A-10)}$$

$$= \sum_m \cos\left(\sum_{j=1}^N a_j(t) m_j\right)$$

To simplify the above expression, let's consider the following:

$$\sum_n \sin\left(\sum_{j=1}^N a_j(t) m_j\right)$$

$$= \sum_{m_1}\sum_{m_2}\cdots\sum_{m_N} \sin\left(\sum_{j=1}^N a_j(t) m_j\right), \quad m_j = -I, \cdots 0, \cdots I$$

$$\equiv 0$$

So, equation (A-10) can be rewritten as

$$\sum_n \cos\left(\sum_{j=1}^N a_j(t) m_j\right) + i\sum_n \sin\left(\sum_{\ell=1}^N a_\ell(t) m_\ell\right)$$

$$= \sum_n e^{i\sum_{j=1}^N a_j(t) m_j}$$

$$= \left(e^{-iIa_1(t)} + e^{-i(I-1)a_1(t)} + \cdots e^{+iIa_1(t)}\right)\left(e^{-iIa_2(t)} + \cdots\right)(\quad)\cdots$$

$$= \prod_{j=1}^N \sum_{m_j=-I}^{I} \cos a_j(t) m_j$$

Using the trigonometric relation

$$\frac{1}{2} + \sum_{\ell=1}^M \cos \ell x = \frac{\sin\left[(2M+1)\frac{1}{2}x\right]}{2\sin\frac{1}{2}x},$$

We get the final result for an ensemble of muons

$$P(t) = P(0) \prod_{j=1}^{N} \frac{\sin[(2I+1)\frac{1}{2}a_j(t)]}{(2I+1)\sin\frac{1}{2}a_j(t)} \tag{A-11}$$

Applications of the above result to some special cases were discussed by Seeger[59] and we will follow his treatment. The expansion of the sine terms in equation (A-11), valid for small t, gives

$$P(t)/P(0) = 1 - \frac{1}{6}I(I+1)\sum_{j=1}^{N}[a_j(t)]^2 \simeq e^{-\frac{1}{6}I(I+1)\sum_{j=1}^{N}[a_j(t)]^2} \tag{A-12}$$

(1) If the muons are immobile:

The α_j's are time independent. Then $g_j(t') = g_j(0) = \alpha_j^2$ and

$$[a_j(t)]^2 = \gamma_\mu^2\gamma_I^2\hbar^2 g_j t^2 \tag{A-13}$$

Therefore, from (A-13)

$$P(t) \simeq P(0)\, e^{-\frac{1}{6\hbar^2}I(I+1)(\sum_{j=1}^{N}\alpha_j^2)t^2}$$

and the relaxation is certainly Gaussian as in equation (A-2).

(2) If $\sum_{j=1}^{N} g_j(t) = e^{-t/\tau_c}\sum_{j=1}^{N}[b_j(0)]^2$, then

$$\sum_{j=1}^{N}[a_j(t)]^2 = \gamma_\mu^2\gamma_I^2\hbar^2 2\int_0^t (t-t')\, e^{-t'/\tau_c}\Big[\sum_{j=1}^{N} b_j(0)\Big]^2 dt'$$

$$= \gamma_\mu^2\gamma_I^2\hbar^2 2\tau_c^2\left[e^{-t/\tau_c} + t/\tau_c - 1\right]\sum_{j=1}^{N}[b_j(0)]^2$$

$$= 2\sigma^2\tau_c^2\left[e^{-t/\tau_c} + t/\tau_c - 1\right]$$

where τ_c is the correlation time of the muon and

$$\sigma^2 = \gamma_\mu^2 \gamma_I^2 \hbar^2 \sum_{j=1}^{N} [b_j(0)]^2 \quad .$$

As τ_c decreases, i.e., the diffusional motion of the muon becomes faster,

$$[e^{-t/\tau_c} + t/\tau_c - 1] \longrightarrow t/\tau_c \quad .$$

Therefore,

$$P(t) = P(0) e^{-2\sigma^2 \tau_c t}$$

which has the same form as equation (A-1), i.e., exponential.

As mentioned before, we used the adiabatic approximation throughout this treatment. By using this we assumed the slow motion of muons in the sense that the muon jump frequency is less than the precessional frequency of the localized dipoles. In a non-magnetic substance these localized dipoles are the dipole moments of nuclei and in a ferromagnetic substance these are the magnetic moments of ions. The condition for the adiabatic approximation is satisfied for muons in most materials except cobalt (see reference 59).

APPENDIX B

The Depolarization of Muon Spin in an Fe Single Crystal

The purpose of this appendix is to provide the underlying physical meaning of the fitting equation mainly used in this work. For this, we will derive the mathematical expression of $\langle \sigma_n(t)\, \sigma_n(0) \rangle$ in the case of Fe where $\sigma_n(t)$ is the component of the muon spin vector along its initial direction.

First, consider a single domain making an angle θ with $\hat{n}$ which is the unit vector in the direction of the initial muon spin, as shown in Figure 56. Then

$$\vec{\sigma} = \sigma_{\parallel} \hat{b} + \vec{\sigma}_{\perp} ,$$

$$\sigma_{\parallel} = \vec{\sigma} \cdot \vec{B}/B = \vec{\sigma} \cdot \hat{b}$$

and

$$d\vec{\sigma}/dt = \vec{\omega}_0 \times \vec{\sigma} + \text{relaxation}$$

where ω_0 is the precessional frequency of the muon.

The Bloch equations for the component of muon spin parallel to the local field $\vec{B}$ can be written as

$$d\sigma_{\parallel}/dt = d(\hat{b} \cdot \vec{\sigma})/dt = - \hat{b} \cdot \vec{\sigma}/T_1 \qquad \text{(B-1)}$$

and for the component perpendicular to $\vec{B}$,

$$d\vec{\sigma}_{\perp}/dt = \vec{\omega}_0 \times \vec{\sigma}_{\perp} - \vec{\sigma}_{\perp}/T_2 \qquad \text{(B-2)}$$

To solve these equations, we need to decompose the muon spin vector into the three orthogonal unit vectors shown in Figure 56. For this, we write

$$\vec{\sigma} = \vec{\sigma} \cdot (\hat{b}\hat{b} + \hat{n}_1\hat{n}_1 + \hat{n}_2\hat{n}_2)$$

where

$$\hat{n}_1 \equiv \frac{\hat{n} \times \hat{b}}{|\hat{n} \times \hat{b}|} \quad , \quad \hat{n}_2 \equiv \hat{b} \times \hat{n}_1 \; .$$

Then

$$(\vec{\omega}_o \times \vec{\sigma}) \cdot \hat{n}_1 = \omega_o (\hat{b} \times \hat{n}_2) \cdot \hat{n}_1 \, \sigma_{n_2}$$

$$= - \omega_o \sigma_{n_2} \; .$$

Similarly,

$$(\vec{\omega}_o \times \vec{\sigma}) \cdot \hat{n}_2 = \omega_o \sigma_{n_1} \; .$$

From these, we get three equations to solve. They are:

$$\frac{d\sigma_b}{dt} = - \sigma_b / T_1 \tag{B-3}$$

for the longitudinal component and

$$\frac{d\sigma_{n_1}}{dt} = - \omega_o \sigma_{n_2} - \frac{\sigma_{n_1}}{T_2} \tag{B-4}$$

$$\frac{d\sigma_{n_2}}{dt} = \omega_o \sigma_{n_1} - \frac{\sigma_{n_2}}{T_2} \tag{B-5}$$

From the last two equations, we get

$$\sigma_{n_1}(t) = e^{-t/T_2} [\sigma_{n_1} \cos \omega_o t - \sigma_{n_2} \sin \omega_o t] \tag{B-6}$$

$$\sigma_{n_2}(t) = e^{-t/T_2} [\sigma_{n_1} \sin \omega_o t + \sigma_{n_2} \cos \omega_o t]$$

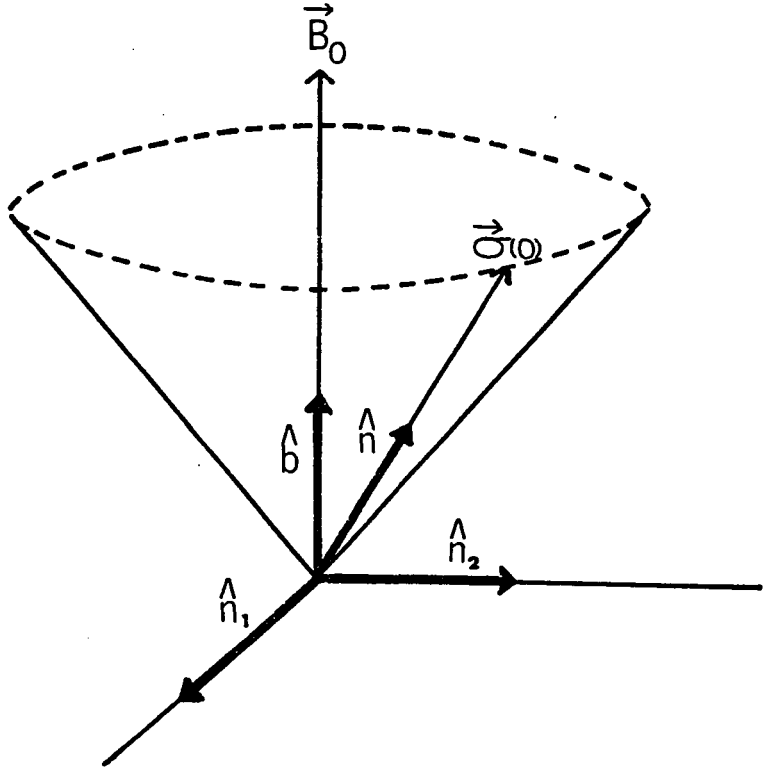

Fig. 56. Precession of the muon spin with an arbitrary initial angle with respect to the domain magnetization direction.

Now, we need to express $\sigma_n(t)$ in terms of $\sigma_{n_1}(t)$, $\sigma_{n_2}(t)$ and $\sigma_b(t)$. Since

$$\vec{\sigma}\cdot\hat{n} = \vec{\sigma}\cdot(\hat{b}\hat{b} + \hat{n}_1\hat{n}_1 + \hat{n}_2\hat{n}_2)\cdot\hat{n}$$

$$= \sigma_{n_2}(\hat{n}_2\cdot\hat{n}) + \sigma_b(\hat{b}\cdot\hat{n})$$

$$= \sigma_{n_2}\sin\theta + \sigma_b\cos\theta \ ,$$

$$\sigma_n(t) = e^{-t/\tau_1}\sigma_b(0)\cos\theta + e^{-t/\tau_2}\sin\theta\left[\sigma_{n_1}(0)\sin\omega_0 t + \sigma_{n_2}(0)\cos\omega_0 t\right] .$$

Thus

$$\sigma_n(t)\,\sigma_n(0) = \sigma_b^2(0)\,e^{-t/\tau_2}\cos^2\theta + e^{-t/\tau_2}\sin\theta\cos\theta\left[\sigma_{n_1}(0)\sigma_b(0)\sin\omega_0 t\right.$$

$$\left. + \sigma_{n_2}(0)\sigma_b(0)\cos\omega_0 t\right] + \sigma_{n_2}(0)\,\sigma_b(0)\,e^{-t/\tau_2}\cos\theta\sin\theta$$

$$+ e^{-t/\tau_2}\sin^2\theta\left[\sigma_{n_1}(0)\sigma_{n_2}(0)\sin\omega_0 t + \sigma_{n_2}(0)\sigma_b(0)\cos\omega_0 t\right] .$$

Then, by the facts that

$$\langle\sigma_b(0)\,\sigma_b(0)\rangle = 1 \ ,$$

$$\langle\sigma_{n_2}(0)\,\sigma_{n_1}(0)\rangle = \langle\sigma_{n_1}(0)\,\sigma_{n_2}(0)\rangle = 1 \qquad \text{, and otherwise zero,}$$

we get

$$\langle\sigma_n(t)\,\sigma_n(0)\rangle = \left\{e^{-t/\tau_1}\cos^2\theta + e^{-t/\tau_2}\sin^2\theta\cos\omega_0 t\right\} \qquad \text{(B-7)}$$

In Fe there are six possible directions of B because the magnetic domains are along $\pm\,\mathcal{Z}_i$ with i = 1, 2, 3. Since the expression of $\langle\sigma_n(t)\ \sigma_n(0)\rangle$ is independent of the signs of θ and ω_0, we need to consider only three domains along $\mathcal{Z}_i$ with i = 1, 2, 3. Now, define f_i as the fractional volume of domains along $\pm\,\mathcal{Z}_i$. Then the $\langle\sigma_n(t)\,\sigma_n(0)\rangle$ averaged with these weighting factors must be

$$\langle \sigma_n(t)\,\sigma_n(0)\rangle = e^{-t/T_1}\sum_i f_i \cos^2\theta_i + e^{-t/T_2}\cos\omega_0 t \sum_i f_i \sin^2\theta_i$$

We will consider two special cases

(1) If the f_i's are all the same:

$$\langle \sigma_n(t)\,\sigma_n(0)\rangle = \frac{1}{3}e^{-t/T_1} + \frac{2}{3}e^{-t/T_2}\cos\omega_0 t \qquad \text{(B-8)}$$

(2) If $f_x = f_y \neq f_z$ and $\theta_z = \pi/2$:

$$\langle \sigma_n(t)\,\sigma_n(0)\rangle = f_x e^{-t/T_1} + (f_x + f_z)\,e^{-t/T_2}\cos\omega_0 t \qquad \text{(B-9)}$$

The condition for case (1) is in fact for an ideal Fe single crystal sample, but we can assume that it is satisfied in an unmagnetized and unstrained Fe single crystal. The conditions for case (2) are satisfied if the uniaxial stress is applied along the z-axis and the direction of the incoming muon beam lies on the x-y plane. With these the fitting function should be

$$N_{F,B}(t) = N_{0F,B}\,e^{-t/\tau_\mu}\left\{1 \pm P\left[F_L e^{-t/T_1} + F_T e^{-t/T_2}\cos(\omega_\mu t + \phi)\right]\right\} + BKG_{F,B} \qquad \text{(B-10)}$$

if we neglect the differences in frequencies in different domains when the sample is strained.

APPENDIX C

The Calculation of the Dipolar Fields in Ferromagnetic Crystals

The dipolar field acting on a muon in a ferromagnetic crystal can be divided into two parts. The first part, which is contributed by the contact interaction between the muon and the conduction electron of the host ion, is the hyperfine field B_{hf}. The second part has the contribution from the localized dipole moments carried by the host ions at the lattice sites of the crystal.

As discussed in Jackson[60] (Chapter 5), the volume integral of a magnetic field produced by a localized current distribution can be shown to be

$$\int_{r<R} \vec{B}\, d\vec{r} = \frac{8\pi}{3}\vec{m} \qquad (C\text{-}1)$$

if the total magnetic moment is inside the sphere of radius R, and

$$\int_{r<R} \vec{B}\, d\vec{r} = \frac{4\pi R^3}{3}\vec{B}(0) \qquad (C\text{-}2)$$

if all the current distribution is external to the sphere. $\vec{B}(0)$ is the field at the center of the sphere. In the region where the wave functions of the muon and the conduction electron overlap, as a result of the interaction, the muon feels a type of field as of equation (C-1). We will discuss B_{hf} and the field due to the localized moments in the following sections.

a. The Muon Hyperfine Field

The total magnetic Hamiltonian of a system consisting of a crystal and a muon can be written as

$$\mathcal{H} = \mathcal{H}_{\mu e} + \mathcal{H}_{\mu N} + \mathcal{Z}_{\mu} + \mathcal{Z}_{e} + \mathcal{Z}_{N}$$

where $H_{\mu e}$ and $H_{\mu N}$ are the interactions of the muon with electrons and nucleus, and Z_{μ}, Z_{e} and Z_{N} are the Zeeman interaction terms of the muon, electrons and nucleus. The Zeeman terms are of the form

$$\mathcal{Z} = -g\mu_B \vec{S} \cdot \vec{H}_{ext}$$

and need no further explanation. Since the magnetic moment of an electron is about 2,000 times larger than that of a nucleus, we neglect the term $H_{\mu N}$ in the case of ferromagnetic material. The general form of $H_{\mu e}$ can be obtained as follows.

From the Pauli approximation we can write the Hamiltonian of an electron as

$$\mathcal{H} = \frac{1}{2m}\left(\vec{p} + \frac{e}{c}\vec{A}\right)^2 + 2\mu_B \vec{S}_e \cdot (\nabla \times \vec{A}) \qquad (C\text{-}3)$$

$$= \frac{p^2}{2m} + \mathcal{H}_1 + \frac{e^2}{2mc^2}\vec{A}^2$$

where

$$\mathcal{H}_1 = \mathcal{H}_{\mu e} = \frac{e}{2mc}(\vec{p}\cdot\vec{A} + \vec{A}\cdot\vec{p}) + 2\mu_B \vec{S}\cdot(\nabla\times\vec{A}) \qquad (C\text{-}4)$$

and A is the vector potential at the electron due to the magnetic moment of the muon. Here, we will consider only the spin dependent term in equation (C-4). We can rewrite this term as follows.

$$
\begin{aligned}
\mathcal{H}^{s}_{\mu e} &= 2\mu_B \vec{S}_e \cdot (\nabla \times \vec{A}) \\
&= 2\mu_B \vec{S}_e \cdot [\nabla \times (\nabla \times \vec{\mu}_\mu / r)] \\
&= 2\mu_B [(\vec{S}_e \cdot \nabla)(\vec{\mu}_\mu \cdot \nabla) - (\vec{S}_e \cdot \vec{\mu}_\mu)\nabla^2] \frac{1}{r} \\
&= 2\mu_B [(\vec{S}_e \cdot \nabla)(\vec{\mu}_\mu \cdot \nabla) - \tfrac{1}{3}(\vec{S}_e \cdot \vec{\mu}_\mu)\nabla^2] \frac{1}{r} - \frac{4}{3}\mu_B (\vec{S}_e \cdot \vec{\mu}_\mu)\nabla^2 \frac{1}{r}
\end{aligned}
\tag{C-5}
$$

where $\vec{r} = \vec{r}_e - \vec{r}_\mu$.

Since

$$
(\vec{S}_e \cdot \nabla)(\vec{\mu}_\mu \cdot \nabla)\frac{1}{r} = -\frac{\vec{S}_e \cdot \vec{\mu}_\mu}{r^3} + 3\frac{(\vec{\mu}_\mu \cdot \vec{r})(\vec{S}_e \cdot \vec{r})}{r^5}
$$

and

$$
\nabla^2\left(\frac{1}{r}\right) = -4\pi\delta(r) ,
$$

equation (C-5) becomes

$$
\mathcal{H}^{s}_{\mu e} = 2\mu_B \hbar \gamma_\mu \left[\frac{(\vec{S}_\mu \cdot \vec{r})(\vec{S}_e \cdot \vec{r})}{r^5} - \frac{\vec{S}_\mu \cdot \vec{S}_e}{r^3}\right] \tag{C-6}
$$

for $r \neq 0$, and it corresponds to the classical dipole interaction. For the limit of $r \to 0$, we consider the matrix elements of the term with the first square bracket of equation (C-5).

$$
\begin{aligned}
&[(\vec{S}_{e_i} \cdot \nabla_i)(\vec{\mu}_{\mu_j} \nabla_j) - \tfrac{1}{3}\delta_{ij} S_{e_i} \mu_{\mu_j} \nabla^2] \frac{1}{r} \\
&= \frac{S_{e_i} \mu_{\mu_j}}{r^3}\left[\frac{3(x_{e_i} - x_{\mu_i})(x_{e_j} - x_{\mu_j}) - \delta_{ij} r^2}{r^2}\right]
\end{aligned}
\tag{C-7}
$$

The term inside the bracket of equation (C-7) is exactly the spherical harmonic $Y_{\ell,m}$ with $\ell = 2$.

The solution of the Schrödinger equation can be constructed as $\psi(r,\theta,\phi) = \frac{U(r)}{r} Y_{\ell,m}(\theta,\phi)$. If the interaction is Coulombic, the radial wave function U(r) must behave as $r^{\ell+1}$ near the origin.[61] The contribution of the first part of equation (C-5) to $\langle \psi_e | \mathcal{H}^{s}_{\mu e} | \psi_e \rangle$ can be written as:

$$\int_0^{r_0} u^*(r)\, u(r) \left[\int Y^*_{\ell' m'}\, Y_{\ell m}\, Y_{\ell'' m''}\, d\Omega \right] dr .$$

The angular integral in the above expression is non-zero only if the conditions

$$|\ell' - \ell''| \leq \ell \leq \ell' + \ell''$$

and

$$m + m'' = m'$$

are satisfied.[62] Since

$$\ell + \ell' + \ell'' = \ell + 2\ell' - (\ell' - \ell'') > 0,$$

the whole integral, with the non-zero angular integral,

$$\int_0^{r_0} r^{\ell + \ell' + \ell''}\, dr$$

becomes zero, as r_0 approaches zero.

Therefore, the interaction between the muon and an electron can be written as

$$\langle \psi_e | \mathcal{H}^s_{\mu e} | \psi_e \rangle = \frac{16}{3} \pi \mu_B \gamma_\mu \vec{S}_\mu \cdot \vec{S}_e \qquad \text{(C-8)}$$

in the region where their wave functions overlap. The interaction in equation (C-9) is the well known Fermi contact interaction. This can also be expressed as

$$\langle \psi_e | \mathcal{H}^s_{\mu e} | \psi_e \rangle = \frac{8\pi}{3} g_\mu \mu_B^\mu g_e \mu_B^e |\psi(0)|^2 \vec{S}_\mu \cdot \vec{S}_e \qquad \text{(C-9)}$$

where $|\psi(0)|^2$ is the density of the conduction electrons at the muon site. As a result, we can say that the contact field

$$\vec{B}_{hf}(\vec{R}_\mu) = \frac{8\pi}{3} \vec{M}(\vec{R}_\mu)$$

acts on the muon where $\vec{M}(\vec{R}_\mu)$ is the local magnetization of the conduction electron at the muon site.

b. The Contribution from the Dipoles inside the Lorentz Cavity

The dipolar field at the muon contributed by the localized moments of the ions in the host crystal is

$$\vec{B}_d(\vec{R}_\mu) = \sum_m \frac{3(\vec{r}_m \cdot \vec{\mu}_{ion})\vec{r}_m - r_m^2 \vec{\mu}_{ion}}{r_m^5} \qquad \text{(C-10)}$$

where $\vec{r}_m = \vec{r} - \vec{R}_\mu$ and the subscript ℓ runs over all the lattice sites in the crystal. The expression in equation (C-10) can be simplified by using the dipolar tensor notation:

$$\vec{B}_d(\vec{R}_\mu) = \sum_m \overleftrightarrow{D}(\vec{r}_m) \cdot \vec{\mu}_{ion} \qquad \text{(C-11)}$$

where

$$D_{ij}(\vec{r}_m) = \frac{3x_{m_i}x_{m_j} - \delta_{ij} r_m^2}{r_m^5} \qquad \text{(C-12)}$$

As discussed in Chapter I, the sum in equation (C-10) can be divided into three parts: the summation over the lattice points inside the Lorentz sphere, the contributions from the magnetic charges on the Lorentz sphere and on the sample surface. The third contribution, which arises from the demagnetizing field for a saturated specimen, depends on the geometry of the sample and will be treated separately. Since the second contribution, $B_L = \frac{4\pi}{3} M_S$, is independent of the radius of the Lorentz sphere, so is the summation within the Lorentz sphere. For this

reason the calculation of the first contribution must be performed until the summation up to the $(n + 1)^{th}$ nearest neighbor atom shell becomes the same as that up to the n^{th} shell. However, due to its slow convergence, the direct lattice summation of equation (C-10) is not appropriate.

The method developed by Ewald to calculate the total electrostatic potential in an ionic crystal has been extended by Meier et al.[63] for the magnetic dipolar field calculation. The derivation of the result obtained by Meier et al. is outlined below.

First, we rewrite equation (C-12) as

$$\mathcal{D}_{ij}(\vec{\Lambda}_m) = (\nabla_i \nabla_j - \tfrac{1}{3}\delta_{ij}\nabla^2)\frac{1}{|\vec{\Lambda}_m|} \tag{C-13}$$

and using

$$\frac{1}{|\vec{\Lambda}|} = \frac{2}{\sqrt{\pi}}\int_0^\infty dh\, e^{-|\vec{\Lambda}|^2 h^2} ,$$

we get

$$\mathcal{D}_{ij}(\vec{\Lambda}_m) = (\nabla_i \nabla_j - \tfrac{1}{3}\delta_{ij}\nabla^2)\frac{2}{\sqrt{\pi}}\left[\int_0^{G} dh\, e^{-|\vec{\Lambda}_m|^2 h^2} + \int_{G}^{\infty} dh\, e^{-|\vec{\Lambda}_m|^2 h^2}\right] . \tag{C-14}$$

The second integral in equation (C-14) can be shown to be

$$\frac{2}{\sqrt{\pi}}\int_{G}^{\infty} e^{-|\vec{\Lambda}_m|^2 h^2} dh = \frac{2}{\Lambda_m\sqrt{\pi}}\int_{G\Lambda_m}^{\infty} e^{-h^2} dh \equiv \frac{1}{\Lambda_m}\,\mathrm{erfc}(G\Lambda_m) \tag{C-15}$$

where erfc is the complementary error function. The derivative of erfc with respect to x_i is

$$\frac{\partial}{\partial x_i}\,\mathrm{erfc}(G\Lambda) = -\frac{2}{\sqrt{\pi}}\, e^{-G^2\Lambda^2}\,\frac{x_i}{\Lambda} .$$

With this we obtain

$$\nabla_i \nabla_j\left[\frac{1}{\Lambda}\,\mathrm{erfc}(G\Lambda)\right] = \nabla_i \nabla_j\left(\frac{1}{\Lambda}\right)\left\{\mathrm{erfc}(G\Lambda) + \frac{1}{\sqrt{\pi}}\left[2G\Lambda + \frac{4}{3}G^3\Lambda^3\right] e^{-G^2\Lambda^2}\right\} \tag{C-16}$$

if $i \neq j$, and

$$\nabla_i \nabla_j \left[\frac{1}{r} \operatorname{erfc}(\alpha r)\right] = \nabla_i \nabla_j \left(\frac{1}{r}\right) \operatorname{erfc}(\alpha r) + \frac{1}{\sqrt{\pi}} \left[\frac{6 x_i^2 \alpha}{r^4} + \frac{4 x_i^2 \alpha^3}{r^2} - \frac{2\alpha}{r^2}\right] e^{-\alpha^2 r^2}$$

which gives

$$\nabla^2 \left[\frac{1}{r} \operatorname{erfc}(\alpha r)\right] = \frac{4}{\sqrt{\pi}} \alpha^3 e^{-\alpha^2 r^2}.$$

From the above two equations, we get

$$(\nabla_i \nabla_j - \tfrac{1}{3} \nabla^2) \left[\frac{1}{r} \operatorname{erfc}(\alpha r)\right] = \nabla_i \nabla_j \left(\frac{1}{r}\right) \left[\operatorname{erfc}(\alpha r) + \frac{1}{\sqrt{\pi}} (2\alpha r + \tfrac{4}{3} \alpha^3 r^3) e^{-\alpha^2 r^2}\right] \qquad \text{(C-17)}$$

Combining equations (C-16) and (C-17),

$$\begin{aligned} E_{ij}^{dir}(\vec{R}_\mu) &= \sum_m (\nabla_i \nabla_j - \tfrac{1}{3} \delta_{ij} \nabla^2) \frac{2}{\sqrt{\pi}} \int_\alpha^\infty dh\, e^{-|\vec{r}_m|^2 h^2} \\ &= \sum_m D_{ij}(\vec{r}_m) \left[\operatorname{erfc}(\alpha r_m) + \frac{1}{\sqrt{\pi}} (2\alpha r_m + \tfrac{4}{3} \alpha^3 r_m^3) e^{-\alpha^2 r_m^2}\right] \end{aligned} \qquad \text{(C-18)}$$

Next, we consider the first part of equation (C-14). For this, it is convenient to change the order of the calculation, i.e., rather than calculate this term for single $\vec{r}_m$, we will calculate the summation over $\vec{r}_m$

$$\sum_m (\nabla_i \nabla_j - \tfrac{1}{3} \delta_{ij} \nabla^2) \frac{2}{\sqrt{\pi}} \int_0^\alpha dh\, e^{-|\vec{r}_m - \vec{R}_\mu|^2 h^2}.$$

Any function $F(\vec{r},h)$ which is periodic in $\vec{r}$ can be expanded in a Fourier series:

$$F(\vec{r}, h) = \sum_{\vec{g}} F_{\vec{g}}\, e^{i \vec{g} \cdot \vec{r}}$$

where the F_g coefficients can be obtained as

$$F_{\vec{g}} = \frac{1}{V} \int F(\vec{r}, h)\, e^{-i \vec{g} \cdot \vec{r}}\, d\vec{r}$$

and $\vec{g}$ is the reciprocal lattice vector. Then, in the same way, we write

$$\sum_{\ell} e^{-|\vec{n}_\ell - \vec{n}|^2 h^2} = \sum_{\vec{g}} F_{\vec{g}}\, e^{i\vec{g}\cdot\vec{n}}$$

and

$$F_{\vec{g}} = \frac{1}{V}\int \sum_{\ell} e^{-|\vec{n}_\ell - \vec{n}|^2 h^2}\, e^{-i\vec{g}\cdot(\vec{n}-\vec{n}_\ell)}\, d\vec{n}$$

$$= \frac{N}{V} e^{-g^2/4h^2} \frac{\pi^{3/2}}{h^3}$$

where N is the total number of lattice points in the crystal. Then we can write

$$\sum_{\ell} e^{-|\vec{n}_\ell - \vec{n}|^2 h^2} = \frac{N\pi^{3/2}}{V h^3} \sum_{\vec{g}} e^{-g^2/4h^2}\, e^{i\vec{g}\cdot\vec{n}}$$

Hence

$$\sum_{m} (\nabla_i \nabla_j - \tfrac{1}{3}\delta_{ij}\nabla^2) \frac{2}{\sqrt{\pi}} \int_0^G dh\, e^{-|\vec{n}_m - \vec{R}_\mu|^2 h^2}$$

$$= \frac{2\pi N}{V} (\nabla_i \nabla_j - \tfrac{1}{3}\delta_{ij}\nabla^2) \sum_{\vec{g}} e^{i\vec{g}\cdot\vec{R}_\mu} \int_0^G dh\, e^{-g^2/4h^2} \frac{1}{h^3}$$

Finally, we get

$$E_{ij}^{nec}(\vec{R}_\mu) = -\frac{4\pi N}{V} \sum_{\vec{g}\neq 0} (g_i g_j - \tfrac{1}{3}\delta_{ij} g^2)/g^2\, e^{i\vec{g}\cdot\vec{R}_\mu}\, e^{-g^2/4G^2} \qquad \text{(C-19)}$$

By appropriate choice of the parameter G, the rapid convergence of the summation in equations (C-18) and (C-19) can be achieved and the computing time to calculate

$$B_{d,i}(\vec{R}_\mu) = E_{ij}(\vec{R}_\mu)\, \mu_{i,m,j}$$

where

$$E_{ij}(\vec{R}_\mu) = E_{ij}^{dir}(\vec{R}_\mu) + E_{ij}^{nec}(\vec{R}_\mu)$$

can be significantly reduced. Equations (C-18) and (C-19) can be used to calculate $\vec{B}_d(\vec{R}_\mu)$ in a strained sample but the strain must be uniform throughout the crystal. Also, it must be noted that the above equations are applicable only for the case of a point-like muon. Corrections for a non-point-like muon and the effect of the local lattice distortion will be discussed in the following sections.

c. The Correction for a Non-Point-like Muon

For a muon which has a non-delta function-like wave function $\psi(\vec{r})$, we have to average the dipolar field by weighting with $\psi(\vec{n})$ everywhere in the sample. Taking $\vec{r}$ as a radius vector from an interstitial site, $\vec{r}_m - \vec{r}$ takes the place of $\vec{r}_m$ in equation (C-13). Then the averaged dipolar field due to a particular atomic dipole can be written as

$$\begin{aligned} \langle B_{d,i}(\vec{R}_\mu)\rangle_\psi &= \int d\vec{n}\, |\psi(\vec{n})|^2 B_{d,i}(\vec{n}_m - \vec{n}) \\ &= (\nabla_i \nabla_j - \tfrac{1}{3}\delta_{ij}\nabla^2) \int d\vec{n}\, |\psi(\vec{n})|^2 \mu_j / |\vec{n}_m - \vec{n}| \end{aligned} \qquad \text{(C-20)}$$

where the differential operators act only on r_m. If we assume that the extension of the muon wave function is strictly limited to the interstitial region, i.e., $|\psi(\vec{n})|^2 = 0$ for $|\vec{n}| > |\vec{n}_m|$,

$$\frac{1}{|\vec{n}_m - \vec{n}|} = \sum_{l=0}^{\infty} (2l+1) P_l(\cos\theta) \frac{n^l}{n_m^{l+1}}$$

Inserting the above expression into equation (C-20), for a spherically symmetric wave function $\psi(r)$,

$$\langle B_{d,i}(\vec{R}_\mu)\rangle_\psi = B_{d,i}(\vec{R}_\mu)$$

which is the result for a point-like muon.

However, the tetragonal symmetry of the interstitial sites of BCC lattices suggests that the muon wave function will not be spherically symmetric, rather, it should be of the form, for its probability density,

$$|\psi(\vec{r})|^2 = \frac{1}{\alpha^2\beta\pi^{3/2}} e^{-\frac{x^2+y^2}{\alpha^2}} e^{-\frac{z^2}{\beta^2}} \qquad \text{(C-21)}$$

for the octa- or tetrahedral site with the tetragonal axis parallel to the z-axis.

To calculate the integral in equation (C-20), we take G = 0 which means that

$$E_{ij}(\vec{R}_\mu) = E_{ij}^{dip}(\vec{R}_\mu) + E_{ij}^{nec}(\vec{R}_\mu) = E_{ij}^{nec}(\vec{R}_\mu)$$

only. Then the integral we need to perform is

$$\langle E_{ij}(\vec{R}_\mu)\rangle_\psi = \frac{4\pi N}{\alpha^2\beta V\pi^{3/2}} \sum_{\vec{g}} \frac{1}{g^2}(g_i g_j - \tfrac{1}{3}\delta_{ij}g^2) \int e^{-i\vec{g}\cdot(\vec{r}+\vec{R}_\mu)} e^{-\frac{x^2+y^2}{\alpha^2}} e^{-\frac{z^2}{\beta^2}} d\vec{r}$$

Performing the integral, we obtain

$$\langle E_{ij}(\vec{R}_\mu)\rangle_\psi = -\frac{4\pi N}{V} \sum_{\vec{g}} (g_i g_j - \tfrac{1}{3}\delta_{ij}g^2)/g^2 \; e^{-(g_x^2+g_y^2)\alpha^2/4} e^{-g_z^2\beta^2/4} \cos(\vec{g}\cdot\vec{R}_\mu) \qquad \text{(C-22)}$$

The exponential terms in equation (C-22) help the summation converge. However, if one uses very small values of α and β, the convergence will be slow. In actual calculations, the summation was performed within the 120th nearest shell centered at the origin of the reciprocal lattice space. The results showed that for the values below $\alpha = \beta = 0.05$ the

range of the summation we chose was not enough because of a slow convergence. For the values larger than 0.05 but smaller than 0.1, the exact point-like muon results were obtained.

d. The Correction for the Local Lattice Distortion around the Muon

To calculate the effects of the local lattice distortion on the dipolar field we need a totally different approach. This is because in this case we cannot define the reciprocal lattice space and also we want an expression of $B_d(\vec{R}_\mu)$ which is an explicit function of the vector $\vec{r}_m$.

The expression

$$\frac{1}{|\vec{\Lambda}_m - \vec{n}|} = \frac{2}{\sqrt{\pi}} \int_0^\infty dh\, e^{-|\vec{\Lambda}_m - \vec{n}|^2 h^2}$$

substituted into equation (C-13) gives

$$D_{ij}(\vec{\Lambda}_m) = \frac{2}{\sqrt{\pi}} \int d\vec{n} \left(\nabla_i \nabla_j - \frac{1}{3}\delta_{ij}\nabla^2\right)\left[\int_0^\infty dh\, e^{-h^2|\vec{\Lambda}_m - \vec{n}|^2}\right] |\psi(\vec{n})|^2$$

$$= \frac{2}{\alpha^2\beta\pi^{3/2}} \int_0^\infty dh \left(\nabla_i \nabla_j - \frac{1}{3}\delta_{ij}\nabla^2\right) \int e^{-|\vec{\Lambda}_m - \vec{n}|^2 h^2} e^{-\frac{x^2+y^2}{\alpha^2}} e^{-\frac{z^2}{\beta^2}} d\vec{n}$$

The integration over $\vec{r}$ can readily be performed to give the result

$$\frac{\pi^{3/2}}{Ah^2\sqrt{B}h} e^{-h^2\left(1-\frac{1}{A}\right)\left(\Lambda_{m_x}^2 + \Lambda_{m_y}^2\right)} e^{-h^2\left(1-\frac{1}{B}\right)\Lambda_{m_z}^2}$$

where $A = 1 + \frac{1}{\alpha^2 h^2}$, $B = 1 + \frac{1}{\beta^2 h^2}$. If we take i = j = 3,

$$\langle D_{33}\rangle = -\frac{8}{3\sqrt{\pi}} \int_0^\infty \frac{dh\, h^2}{(1+\alpha^2h^2)\sqrt{1+\beta^2h^2}} \left\{\left[\left(1 - \frac{2h^2\Lambda_{m_z}^2}{1+\beta^2h^2}\right)\Big/ 1+\beta^2h^2\right] - \left[\left(1 - \frac{h^2(\Lambda_{m_x}^2+\Lambda_{m_y}^2)}{1+\alpha^2h^2}\right)\Big/ 1+\alpha^2h^2\right]\right\} \quad \text{(C-23)}$$

$$\times\, e^{-h^2(\Lambda_{m_x}^2 + \Lambda_{m_y}^2)/1+\alpha^2h^2}\, e^{-h^2\Lambda_{m_x}^2/1+\beta^2h^2}$$

for the sites with their tetragonal axis parallel to $\vec{M}_s = M_s\hat{Z}$ and

$$\langle D_{33} \rangle = -\frac{4}{3\sqrt{\pi}} \int_0^\infty \frac{dh\, h^2}{(1+\alpha^2 h^2)\sqrt{1+\beta^2 h^2}} \left\{ \left[\left(1 + 2h^2 \frac{(\Lambda_{m_x}^2 - 2\Lambda_{m_z}^2)}{1+\alpha^2 h^2} \right) / 1+\alpha^2 h^2 \right] \right.$$

$$\left. - \left[\left(1 - \frac{2h^2 \Lambda_{m_y}^2}{1+\beta^2 h^2} \right) / 1+\beta^2 h^2 \right] \right\} e^{-h^2(\Lambda_{m_x}^2 + \Lambda_{m_z}^2)/1+\alpha^2 h^2} \; e^{-h^2 \Lambda_{m_z}^2 / 1+\beta^2 h^2} \qquad \text{(C-24)}$$

for the sites with their tetragonal axis perpendicular to $\vec{M}_S$. Since the above two equations are very complicated functions of h, the integrals were performed numerically. The results showed that the upper limit of $h_{max} = 15$ is more than enough. The calculation was performed for each individual ion around the muon site.

To calculate the dipolar field at the muon in a crystal with the local distortion we assumed that this distortion was substantial only up to the second nearest ions around the muon. First, we calculated $B_d(\vec{R}_\mu)$ for an undistorted crystal by equation (C-22). Then the contribution from the undisplaced ions within the second nearest shell was replaced by that from the displaced ones.

APPENDIX D

The Demagnetizing Field in a Thin Slab Sample

In this appendix we will discuss a computational method for a somewhat oversimplified problem. To calculate the demagnetizing field we assume that the atomic moments are arranged as in Figure 57(a) when saturated by an external field. Figure 57(b) shows the actual situation for a slab sample which we will not discuss.

As shown in Figure 57(c), we calculate the field at P produced by a rectangular sheet of uniform pole density, with sides a and b. The field at P due to the elementary pole $\sigma\, dxdy$ at (x,y) is $\sigma\, dxdy/r^2$ along r. With $y = s\tan\theta$, then $dH_r = \sigma\, dxd\theta\ /S$ and the component along s is $dH_S = \sigma\, dx\cos\theta\ d\theta\ /S$. Integrating with respect to θ gives the field due to the strip $\sigma b dx/qs$ with a component parallel to OX as

$$dH_x = \sigma b z\, dx/s^2 q\ .$$

Integrating with respect to x from c to (c + a) gives, for the whole sheet

$$H_x = -\sigma \ln \left\{ \frac{[(c+a)^2 + z^2]^{1/2}}{[(c+a)^2 + z^2 + b^2]^{1/2} + b} \cdot \frac{(c^2 + z^2 + b^2)^{1/2} + b}{(c^2 + z^2)^{1/2}} \right\} \qquad \text{(D-1)}$$

the negative sign indicating that the field is antiparallel to the positive OX direction for positive charges. The resolved field along OZ due to the strip is

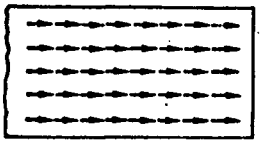

(a)

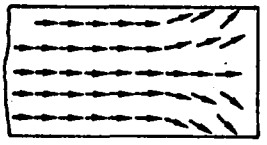

(b)

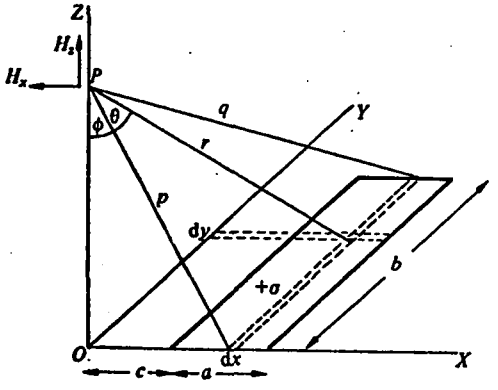

(c)

Fig. 57. Alignment of magnetic moments (a) with an infinite anisotropy energy, and (b) with a finite anisotropy energy. The demagnetization field is calculated, as in (c), assuming the situation of (a).

$$\frac{\sigma b z\, dx}{s^2 g} = \frac{\sigma b z\, dx}{(x^2+z^2)(x^2+z^2+b^2)^{1/2}}$$

Substituting $x = z \tan\phi$ and integrating with respect to gives

$$H_z = \sigma \sin^{-1}\left\{\frac{(c+a)b}{[(c+a)^2+z^2]^{1/2}(b^2+z^2)^{1/2}}\right\} - \sigma \sin^{-1}\left\{\frac{bc}{[(c^2+z^2)(b^2+z^2)]^{1/2}}\right\} \qquad \text{(D-2)}$$

the limits of ϕ being $\sin^{-1}\left\{\frac{c}{[(z^2+c^2)]^{1/2}}\right\}$ and $\sin^{-1}\left\{\frac{(c+a)}{[z^2+(c+a)^2]^{1/2}}\right\}$. The first term is always larger and when σ is positive the direction is parallel to positive OZ.

To inspect the inhomogeneity in B_μ, we will calculate only H_z in equation (D-2) for the Fe ⟨100⟩ crystal. The sample dimension is 1 x 4.6 x 46 mm^3. As shown in Figure 58, calculations were performed along the five lines parallel to the z-axis in the rectangle ABCD. The results are shown in Figure 59 with the rectangle at the surface of the sample. Among the five curves drawn in the figure, the topmost one corresponds to the line segment $\overline{CD}$ in Figure 59. The results show that B_{dem} almost depends on Z only. Figure 60 shows the results of the same calculations with the rectangle at the center of the sample. This indicates that the y dependence is also negligible.

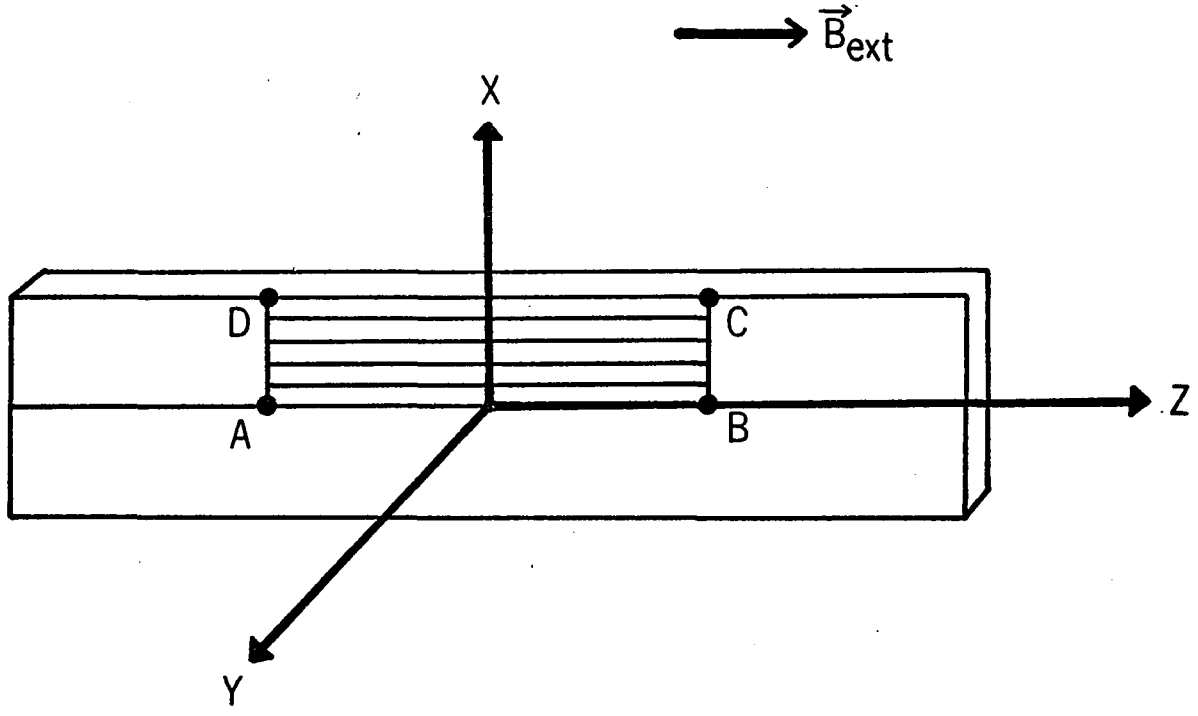

Fig. 58. The demagnetization field is calculated along six lines including line segments DC and AB.

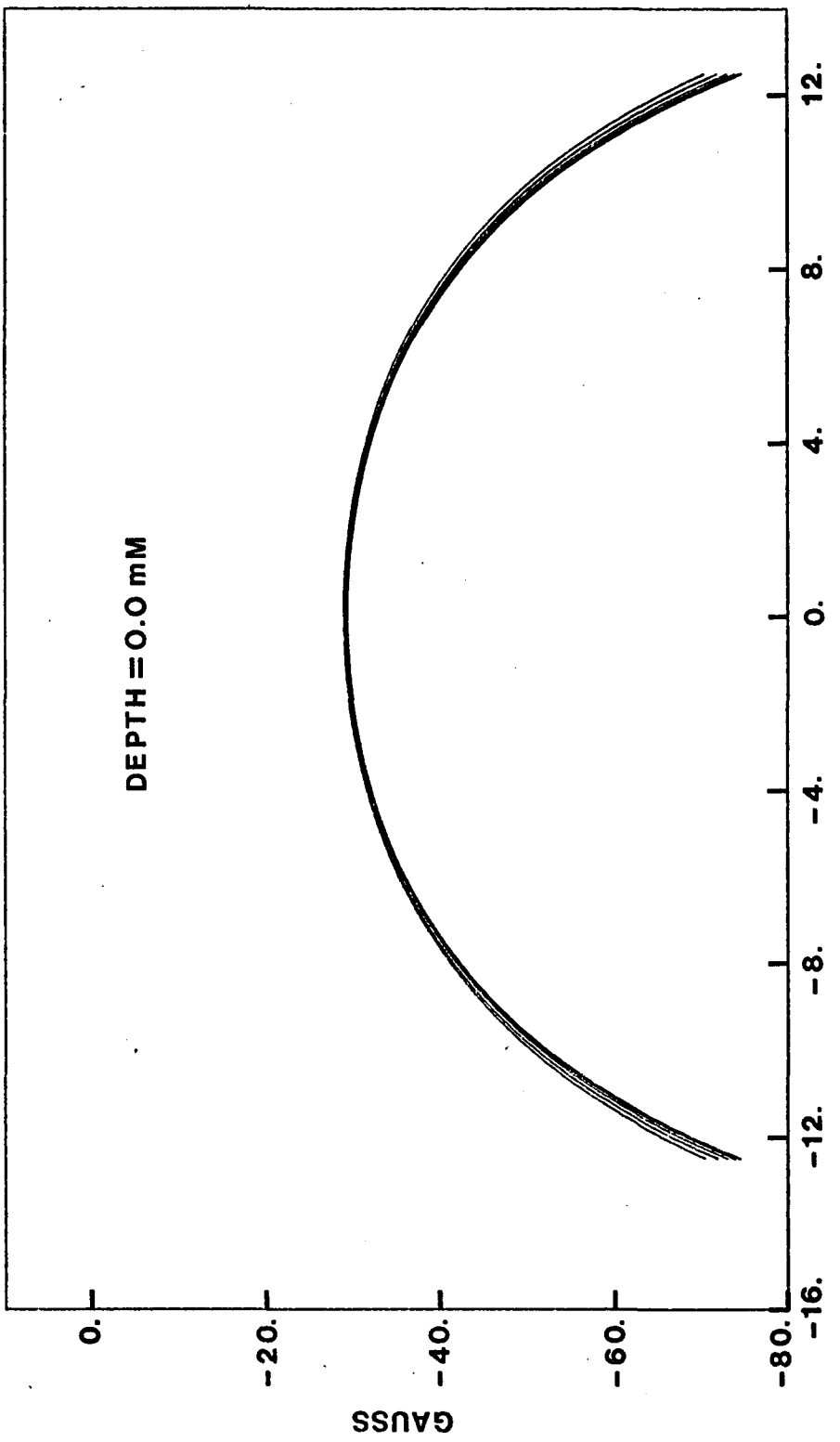

Fig. 59. Demagnetization field calculated along six lines on the surface of a sample. The topmost curve represents fields along the center line.

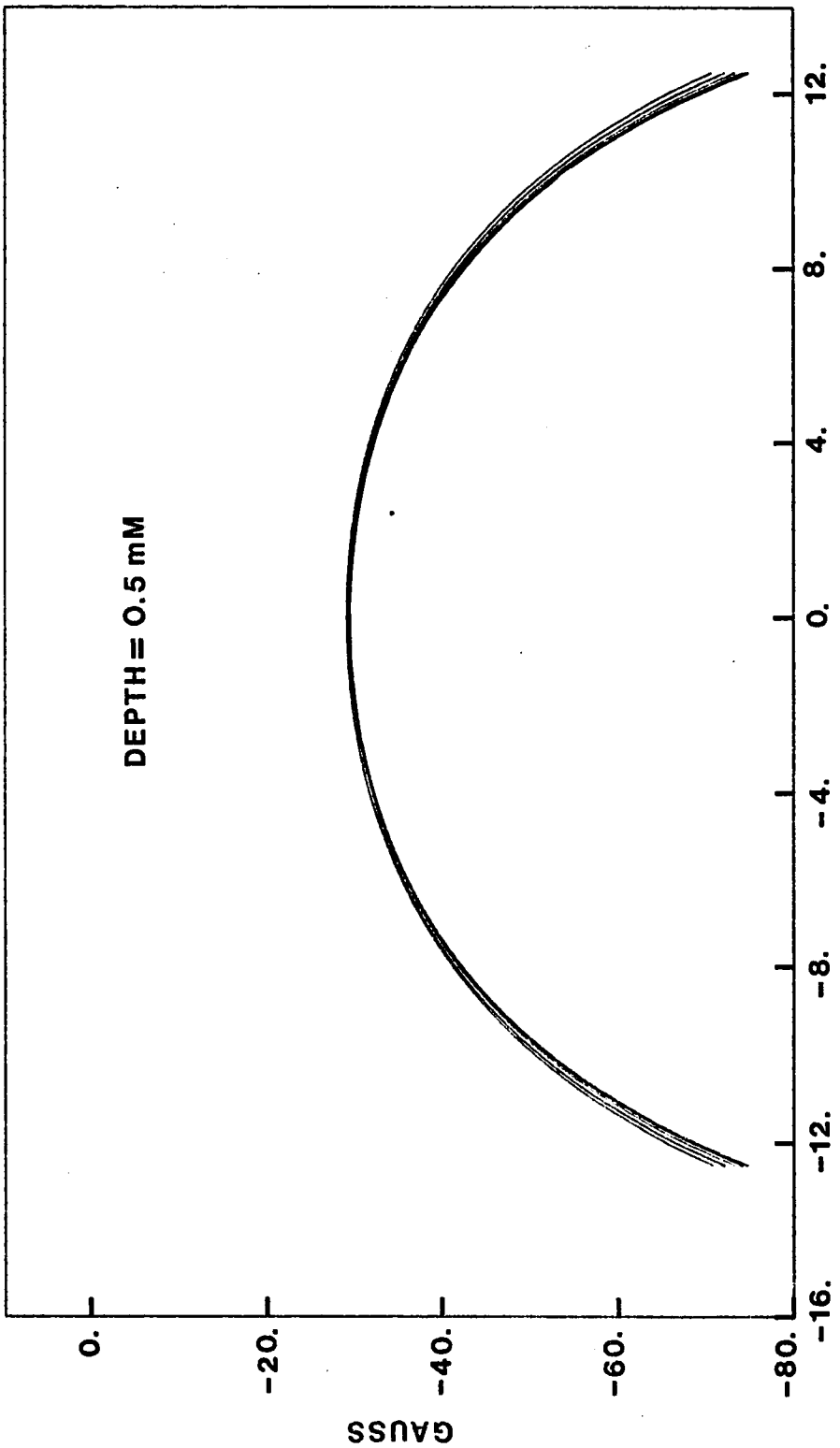

Fig. 60. Demagnetization fields calculated on the center plane of a slab sample.

REFERENCES

1. R. I. Grynszpan, N. Nishida, K. Nagamine, R. S. Hayano, T. Yamazaki, J. H. Brewer and D. G. Fleming, Solid State Comm. 29, 143 (1979).
2. A. S. Arrott, B. Heinrich, C. E. Stronach and W. F. Lankford, Journal of Applied Physics 53, 1985 (1982).
3. A. H. Cottrell, Dislocation and Plastic Flow in Crystals (Oxford, New York, 1952).
4. T. Butz, J. Chappert, J. F. Dufresne, O. Hartman, E. Karlsson, B. Lindgren, L. O. Norlin, P. Pondini, and A. Yaouanc, Phys. Lett. 75A, 321 (1980).
5. G. Källén, Elementary Particle Physics (Addison-Wesley, New York 1964).
6. A. Schenck, Nuclear and Particle Physics at Intermediate Energies, edited by J. Warren (Plenum, New York, 1976).
7. J. H. Brewer, K. M. Crowe, F. N. Gygax, and A. Schenck, Muon Physics, Vol. 3: Chemistry and Solids, edited by W. Hughes and C. S. Wu (Academic, New York, 1975).
8. G. W. Ford and C. J. Mullin, Phys. Rev. 108, 477 (1957).
9. G. Wentzel, Phys. Rev. 75, 1810 (1949).
10. H. A. Mook, Phys. Rev. 148, 495 (1966).
11. K. G. Petzinger and R. Munjal, Phys. Rev. B 15, 1560 (1977).
12. P. Jena, K. S. Singwi, and R. M. Nieminen, Phys. Rev. B 17, 301 (1978).
13. C. G. Shull and H. A. Mook, Phys. Rev. Lett. 16, 184 (1966).

14. J. Kanamori, H. K. Yoshida, and K. Terakura, Hyperfine Interac. 8, 573 (1981).

15. J. Keller and B. D. Patterson, Hyperfine Interact. 6, 73 (1979).

16. H. Katayama, K. Terakura, and J. Kanamori, Solid State Comm. 29, 431 (1979).

17. O. Jepsen, R. M. Nieminen, and J. Madsen, Solid State Comm. 34, 575 (1980).

18. S. Estreicher, A. B. Denison and P. F. Meier, Hyperfine Interact. 8, 601 (1981).

19. P. F. Meier and S. Estreicher, Phys. Rev. B 25, 297 (1982).

20. A. Seeger, Phys. Lett. A 58, 137 (1976).

21. N. Nishida, R. S. Hayano, K. Nagamine, T. Yamazaki, J. H. Brewer, D. M. Garner, D. G. Fleming, T. Takeuchi and Y. Ishikawa, Solid State Comm. 22, 235 (1977).

22. E. Yagi, H. Bossy, K. P. Döring, M. Gladisch, D. Herlach, H. Matsui, H. Orth, G. zu Putlitz, A. Seeger, and J. Vetter, Hyperfine Interact. 8, 553 (1981).

23. D. M. Garner, Ph.D. Thesis, University of British Columbia, (1979), unpublished.

24. E. Holzschuh, Ph.D. Thesis, University of Zürich, (1982), unpublished.

25. P. R. Bevington, Data Reduction and Error Analysis for the Physical Sciences, (McGraw-Hill, New York, 1969).

26. C. Kittel, Introduction to Solid State Physics, 4th Ed., (John Wiley and Sons, New York, 1971).

27. D. H. Martin, Magnetism in Solids, (MIT Press, Cambridge, 1964).

28. S. Chikazumi, Physics of Magnetism (John Wiley and Sons, New York, 1964).

29. J. M. Ziman, Principles of the Theory of Solids (Cambridge University Press, New York, 1963).

30. A. H. Morrish, The Physical Principles of Magnetism (John Wiley and Sons, New York, 1965).

31. S. V. Vonsovskii, Magnetism Vol. II (John Wiley and Sons, New York, 1974).

32. W. A. Harrison, Solid State Theory (McGraw-Hill, New York, 1970).

33. B. D. Culity, Introduction to Magnetic Materials (Addison-Wesley, Menlo Park, 1972).

34. C. Kittel, Rev. Mod. Phys. 21, 541 (1949).

35. A. E. H. Love, A Treatise on the Mathematical Theory of Elasticity (Cambridge University Press, New York, 1944).

36. D. J. Craik, Structure and Properties of Magnetic Materials (Pion Limited, London, 1971).

37. R. M. Bozorth, Ferromagnetism (Van Nostrand, New York, 1951).

38. A. S. Nowick and B. S. Berry, Anelastic Relaxation in Crystalline Solids (Academic Press, New York, 1972).

39. H. Kanzaki, J. Phys. Chem. Solids 2, 24 (1957).

40. A. Kelly and G. W. Groves, Crystallography and Crystal Defects (Addison-Wesley, Menlo Park, 1970).

41. M. Tinkham, Group Theory and Quantum Mechanics (McGraw-Hill, New York, 1964).

42. M. Eisenstadt, Introduction to Mechanical Properties of Materials (Macmillan Company, New York, 1971).

43. W. T. Read, Jr., Dislocations in Crystals (McGraw-Hill, New York, 1953).

44. B. Edmonson, Proc. Roy. Soc. A 264, 176 (1961).

45. C. P. Slichter, Principles of Magnetic Resonance, 2nd Ed. (Springer-Verlag, New York, 1980).

46. J. A. Osborn, Phys. Rev. 67, 351 (1945).

47. H. Träuble, The Influence of Crystal Defects on Magnetization Processes in Ferromagnetic Single Crystals: Magnetism and Metallurgy Vol. II, edited by A. E. Berkowitz and E. Kneller (Academic Press, New York, 1969).

48. The results are presented in the article: W. J. Carr, Jr., in Ferromagnetism, edited by J. P. J. Wijn (Springer-Verlag, New York, 1966).

49. The results are presented in Reference 31.

50. D. Bloch and R. Pauthenet, J. Appl. Phys. 36, 1229 (1965).

51. K. Gschneider, Jr., Solid State Phys. 16, 275 (1964).

52. E. I. Kondorskii and V. L. Sedov, Soviet Physics JETP 11, 561 (1960).

53. E. I. Kondorskii, Soviet Physics JETP 10, 1284 (1960).

54. C. G. Shull, in Magnetic and Inelastic Scattering of Neutrons by Metals, Eds. T. J. Rowland and P. A. Beck (Gordon and Breach, New York, 1967).

55. H. Sugimoto and Y. Fukai, Phys. Rev. B 22, 670 (1980).

56. R. A. Johnson, G. J. Dienes, and A. C. Damask, Acta Metall. 12, 1215 (1964).

57. C. E. Stronach, W. J. Kossler, J. Lindemuth, K. G. Petzinger, A. T. Fiory, R. P. Minnich, W. F. Lankford, J. J. Singh and K. G. Lynn, Phys. Rev. B 20, 2315 (1979).

58. G. De Vries, D. W. Van Geest, R. Gersdorf and G. W. Rathenau, Physica 25, 1131 (1959).

59. A. Seeger, Positive Muons as Light Isotopes of Hydrogen, in Hydrogen in Metals I, Eds. G. Alefeld and J. Völkl (Springer-Verlag, New York, 1978).

60. J. D. Jackson, Classical Electrodynamics, 2nd Ed. (John Wiley and Sons, New York, 1975).

61. E. Merzbacher, Quantum Mechanics, 2nd Ed. (John Wiley and Sons, New York, 1970).

62. G. Arfken, Mathematical Methods for Physicists, 2nd Ed. (Academic Press, New York, 1970).

63. P. F. Meier, W. Kündig, B. D. Patterson and K. Rüegg, Hyperfine Interact. 5, 311 (1978).